Innovative approaches for

Improvement of incision wound care in patients post implantation of cardiac electronic devices

and

Modeling breast cancer cell invasion of lymph node ex vivo

A Dissertation presented to

the graduate faculty of the School of Engineering and Applied Science

University of Virginia

in partial fulfillment of the

requirements for the degree of

Doctor of Philosophy

by

Katsiarina Morgaenko

June 2024

APPROVAL SHEET

This Dissertation

is submitted in partial fulfillment of the requirements for the degree of

Doctor of Philosophy

Author: Katsiarina Morgaenko

Advisor: Rebecca Pompano, PhD

Committee Member: Sepideh Dolatshahi, PhD

Committee Member: Shayn Peirce-Cottler, PhD

Committee Member: Melanie Rutkowski, PhD

Committee Member: Jennifer Munson, PhD

Committee Member: Natasha Sheybani, PhD

Accepted for the School of Engineering and Applied Science:

Jennifer L. West, School of Engineering and Applied Science

June 2024

Dedication

To my beloved parents,

In loving memory of my late father, whose guidance continues to shape my journey, and to my mother, whose support paved the path for my accomplishments. Your love, encouragement, and sacrifices have been the foundation of my success, and I am forever grateful for every moment you've invested in my dreams. This work stands as a tribute to your boundless love and enduring legacy.

With heartfelt gratitude,

Katerina

Acknowledgments

This dissertation would not have been achievable without the contributions and support of many incredible individuals, only a few of whom I can acknowledge here.

First, I want to express my most sincere appreciation to my PhD advisor, Dr. Rebecca Pompano. Throughout this journey, you always made time for our long meetings, always approached every challenge with optimism, and always found kind words of advice and support. From the initial stages of this project to the final draft, you have provided me with the freedom to explore my ideas while offering the critical insights necessary to refine them. Under your guidance, I have become a better writer, presenter, thinker, collaborator, mentor, and overall, a much better researcher than I ever thought I could be. Thank you for shaping my scientific character.

I extend my gratitude to the PhD committee members, Dr. Shayn Peirce-Cottler, Dr. Sepideh Dolatshahi, Dr. Melanie Rutkowski, Dr. Jennifer Munson, and Dr. Natasha Sheybani. It has been an honor to complete the work of this dissertation under your guidance. Your expert advice and constructive critiques have been crucial in shaping the direction and quality of my research. The time and effort you invested in reviewing my work and providing detailed suggestions have been deeply appreciated.

I am profoundly grateful to Dr. Zygmunt Derewenda for establishing the visiting research traineeship program at UVA, which provided me with an invaluable opportunity to further my academic journey. I extend my heartfelt appreciation to my advisor, Dr. Nishaki Mehta, who welcomed me as an international visiting scholar to her lab and supported me in my pursuit of a PhD career.

I would like to thank all the past and present members of the Pompano Lab for the collaborative environment we have cultivated together. I wish to extend my heartfelt thanks to Tochi Ozulumba, Alex Ball, and Parris Anbaei. Whether it was troubleshooting experimental challenges, discussing research ideas, or simply providing words of encouragement, your support has made a significant difference. Thank you for not only being exceptional colleagues but also dear friends. The countless hours spent together in the lab, the shared triumphs and setbacks (with minigolf being, for my part, the major one), and the many memorable moments have created a bond that I will cherish always. I would also like to thank Morgan McKnight, the undergraduate student I had the honor to work with during my research. It has been a pleasure working with you, and I look forward to seeing all that you will accomplish in your academic and professional journey.

I would like to express my deepest gratitude to my family for their unwavering support and for always nourishing my curiosity. To my late grandad, Alexander, who has been a role model and motivated me to choose a scientific career, thank you for your guidance and inspiration. To my mother, Elena, and my late father, Andrei, I am forever grateful for the sacrifices you made to allow me to study abroad and pursue my dreams. Your love and dedication have been the foundation of my achievements. To my younger sister, Liza, thank you for taking on my responsibilities and helping care for our family in my absence. Your support has been invaluable and has allowed me to focus on my studies.

I would like to express my deepest gratitude to my husband, Bojan, who has been the most patient, kind, understanding, and supportive partner throughout this journey. Your support has provided me with the strength and motivation to persevere through the challenges and celebrate the achievements.

List of Figures

List of Tables

Preface

This thesis is divided into two parts, representing the two laboratories where the research was conducted.

The first part of this thesis, covered in **Chapters 1-4,** describes research in the field of cardiovascular medicine performed under the supervision of Dr. Nishaki Mehta, a cardiac electrophysiologist and an assistant professor of biomedical engineering at the University of Virginia School of Medicine from 2017 to 2020. This research focused on **dermatologic evaluation and novel hematoma prevention strategies for improved outcomes in patients post- cardiac implantable electronic device (CIED) surgery.**

Infections following CIED implantation pose significant mortality risks. Additionally, the cosmetic appearance of post-CIED implantation scars critically impacts patients' quality of life. Despite these issues, systematic dermatologic evaluation of surgical wounds post-CIED implantation and strategies for hematoma prevention have not been well-established. In **Chapter 2** we characterized baseline wound scar features using quantifiable surgical tools and scar scales. In **Chapter 3** we evaluated a novel mechanical compression device designed for hematoma prevention and improved cosmetic outcomes in post-CIED patients.

The second part of this thesis, covered in **Chapters 5-8**, details research in the field of cancer immunology conducted under the supervision of Dr. Rebecca Pompano, an Assistant Professor in the Departments of Chemistry and Biomedical Engineering at the University of Virginia. This research focused on **developing a novel model of breast cancer invasion in tumor-draining lymph nodes (TDLNs).** TDLNs are common sites of metastatic invasion in breast cancer, often preceding spread to distant organs and serving as key indicators of clinical disease

progression. However, the mechanisms of cancer cell invasion into LNs are not well understood. Existing in vivo models struggle to isolate the specific impacts of the TDLN milieu on cancer cell invasion due to the co-evolving relationship between TDLNs and the upstream tumor. To address these limitations, in **Chapter 6** we used live LN tissue slices with intact chemotactic function to model cancer cell spread ex vivo within a controlled microenvironment. In **Chapter 7** we characterized physical and biochemical aspects of TDLN remodeling in early and advanced stages of breast cancer disease.

Table of Contents

1 Introduction to patient outcomes and wound care post implantation of cardiovascular implantable electronic devices

1.1. Impacts of CIED surgery on patient outcomes

Cardiovascular implantable electronic devices (CIEDs), including pacemakers and implantable cardioverter-defibrillators, are life-enhancing technologies essential for monitoring and maintaining heart rhythm in patients with heart disorders.[1] Annually, up to 1.4 million CIEDs are implanted globally.[2] A conventional CIED is usually implanted in a subcutaneous pocket in the chest, with leads extending from the device through the veins to the heart (Figure 1.1). CIED surgery is an invasive procedure that inherently involves risks, such as complications in wound healing and infections.[3]

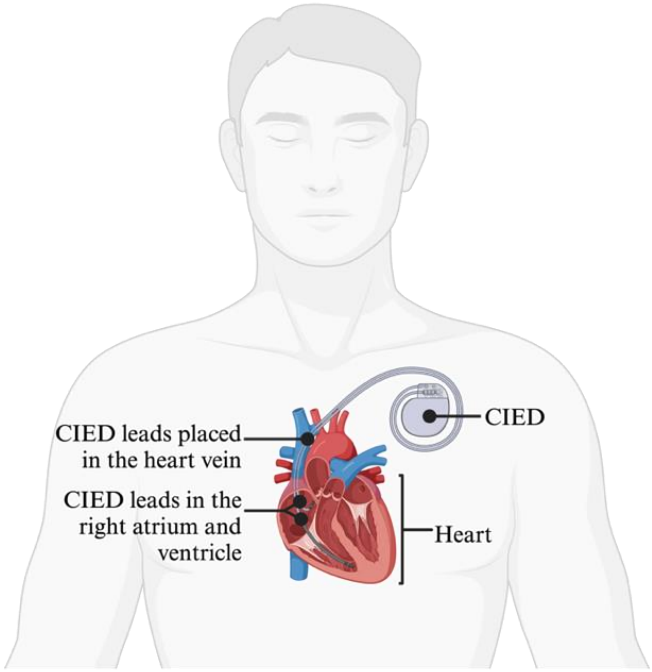

Figure 1.1: Placement of CIED device. CIED device is impanated into the subcutaneous chest pocket, with leads positioned in the heart's veins, reaching the right atrium and ventricle. Created with BioRender.

The occurrence of a hematoma post device implantation is linked to a risk of device infection that is up to 21 times higher, making it one of the most serious complications of CIED surgery.[4–6] While the mortality rate directly related to CIED implantation is low, the risk of mortality due to infections and severe bleeding remains a major concern.[7,8] Additionally, an infection of the post-CIED implantation wound can result in extended hospital stays, necessitate systemic antibiotics and surgical removal of the device, significantly increasing healthcare expenses.[9,10]

Furthermore, the physical impacts of CIED surgery extend beyond the immediate postoperative period, significantly affecting patients' long-term well-being. One common concern is the cosmetic appearance of scars, which plays a crucial role in patient perception, potentially leading to decreased self-esteem and psychological distress.[11] Additionally, physical complications such as chronic pain or sensitivity around the scar tissue can restrict mobility and daily activities, further diminishing the overall quality of life.[12]

1.2. Importance of improving post CIED implantation wound care

Postoperative care for CIED implantation focuses on minimizing complications and promoting optimal wound healing. Standard care strategies to reduce postoperative hematoma include monitoring the surgical site for signs of infection, ensuring proper sterility, and dressing of the wound, including application of pressure dressing, sandbags or ice packs.[13] Despite these measures, significant risks remain if post-surgical bleeding or hematoma is overlooked. Currently applied compression dressings can inadvertently conceal early signs of hematoma, leading to delayed diagnosis and an increased risk of infection.[14]

Given the broad spectrum of potential complications and their impacts on patient outcomes, improving post-CIED surgery wound care is paramount. Enhanced wound care protocols can

reduce the incidence of complications, shorten hospital stay, and improve overall patient outcomes. Innovations in characterization of the wound scarring and advancements in dressing materials that allow for better monitoring and breathability, could prevent occurrence of hematoma, and further diminish infection-associated complication.

1.3. Concluding remarks

In conclusion, the impact of CIED surgery on patient outcomes is profound, encompassing both immediate postoperative risks and long-term physical and psychological effects. Addressing these challenges through improved wound care protocols is essential for enhancing patient outcomes and reducing healthcare costs.

Currently, there are no standardized tools to evaluate wounds after CIED implantation in the acute postoperative phase. In **Chapter 2**, we aimed to establish a baseline for dermatologic evaluation of post-CIED wounds using quantifiable surgical tools and scar scales. Next, in **Chapter 3** we developed an innovative compressive device to prevent hematoma formation in post-CIED patients. We evaluated the effectiveness of this novel compression device improving cosmetic outcomes following CIED implantation. **Chapter 4** provides a summary of the innovation and its impact, discussion about the limitations of the study, and potential directions for further research and development.

1.4. References

(1) Kotalczyk, A.; Kalarus, Z.; Wright, D. J.; Boriani, G.; Lip, G. Y. H. Cardiac Electronic Devices: Future Directions and Challenges. *Med. Devices Evid. Res.* **2020**, *Volume 13*, 325–338. https://doi.org/10.2147/MDER.S245625.

(2) Mkoko, P.; Mdakane, N. X.; Govender, G.; Scherman, J.; Chin, A. Experience of Cardiac Implantable Electronic Device Lead Removal from a South African Tertiary Referral Centre. *Cardiovasc. J. Afr.* **2021**, *32* (4), 21–25. https://doi.org/10.5830/CVJA-2021-010.

(3) Gandhi, T.; Crawford, T.; Riddell, J. Cardiovascular Implantable Electronic Device Associated Infections. *Infect. Dis. Clin. North Am.* **2012**, *26* (1), 57–76. https://doi.org/10.1016/j.idc.2011.09.001.

(4) Greenspon, A. J.; Patel, J. D.; Lau, E.; Ochoa, J. A.; Frisch, D. R.; Ho, R. T.; Pavri, B. B.; Kurtz, S. M. 16-Year Trends in the Infection Burden for Pacemakers and Implantable Cardioverter-Defibrillators in the United States 1993 to 2008. *J. Am. Coll. Cardiol.* **2011**, *58* (10), 1001–1006. https://doi.org/10.1016/j.jacc.2011.04.033.

(5) Tarakji, K. G.; Ellis, C. R.; Defaye, P.; Kennergren, C. Cardiac Implantable Electronic Device Infection in Patients at Risk. *Arrhythmia Electrophysiol. Rev.* **2016**, *5* (1), 65–71. https://doi.org/10.15420/aer.2015.27.2.

(6) Song, J.; Tark, A.; Larson, E. L. The Relationship between Pocket Hematoma and Risk of Wound Infection among Patients with a Cardiovascular Implantable Electronic Device: An Integrative Review. *Heart Lung J. Crit. Care* **2020**, *49* (1), 92–98. https://doi.org/10.1016/j.hrtlng.2019.09.009.

(7) Kewcharoen, J.; Kanitsoraphan, C.; Thangjui, S.; Leesutipornchai, T.; Saowapa, S.; Pokawattana, A.; Navaravong, L. Postimplantation Pocket Hematoma Increases Risk of Cardiac Implantable Electronic Device Infection: A Meta-analysis. *J. Arrhythmia* **2021**, *37* (3), 635–644. https://doi.org/10.1002/joa3.12516.

(8) Vasilev, S. Strategies for Prevention of Surgical Site Infection in Patients With CIED Implantation: A Literature Review. *Cureus* **2021**. https://doi.org/10.7759/cureus.13021.

(9) Sohail, M. R. Mortality and Cost Associated With Cardiovascular Implantable Electronic Device Infections. *Arch. Intern. Med.* **2011**, *171* (20), 1821. https://doi.org/10.1001/archinternmed.2011.441.

(10) Costabella, F.; Patel, K. B.; Adepoju, A. V.; Singh, P.; Attia Hussein Mahmoud, H.; Zafar, A.; Patel, T.; Watekar, N. A.; Mallesh, N.; Fawad, M.; Sathyarajan, D. T.; Abbas, K. Healthcare Cost and Outcomes Associated With Surgical Site Infection and Patient Outcomes in Low- and Middle-Income Countries. *Cureus* **2023**. https://doi.org/10.7759/cureus.42493.

(11) Garg, S. P.; Weissman, J. P.; Reddy, N. K.; Varghese, J.; Ellis, M. F.; Kim, J. Y. S.; Galiano, R. D. Patient-Reported Outcomes of Scar Impact: Comparing of Abdominoplasty, Breast Surgery, and Facial Surgery Patients. *Plast. Reconstr. Surg. - Glob. Open* **2022**, *10* (10), e4574. https://doi.org/10.1097/GOX.0000000000004574.

(12) Abd-Elsayed, A.; Pope, J.; Mundey, D. A.; Slavin, K. V.; Falowski, S.; Chitneni, A.; Popielarski, S. R.; John, J.; Grodofsky, S.; Vanetesse, T.; Fishman, M. A.; Kim, P. Diagnosis, Treatment, and Management of Painful Scar: A Narrative Review. *J. Pain Res.* **2022**, *Volume 15*, 925–937. https://doi.org/10.2147/JPR.S355096.

(13) Mehta, N. K.; Doerr, K.; Skipper, A.; Rojas-Pena, E.; Dixon, S.; Haines, D. E. Current Strategies to Minimize Postoperative Hematoma Formation in Patients Undergoing Cardiac Implantable Electronic Device Implantation: A Review. *Heart Rhythm* **2021**, *18* (4), 641–650. https://doi.org/10.1016/j.hrthm.2020.11.017.

(14) Blomstrom-Lundqvist, C.; Ostrowska, B. Prevention of Cardiac Implantable Electronic Device Infections: Guidelines and Conventional Prophylaxis. *EP Eur.* **2021**, *23* (Supplement_4), iv11–iv19. https://doi.org/10.1093/europace/euab071.

2 Baseline incision characteristics and early scar maturation indices following cardiac device implantation.

Portions of this chapter were adapted from the following:

Mehta, N.K., Morgaenko, K., Haines, D., Rojas-Pena, E., Heard, B., Malhotra, R., Darby, A., Mangrum, J.M., Mason, P., Campbell, C. and Bilchick, K., 2021. Baseline incision characteristics and early scar maturation indices following cardiac device implantation. *Journal of arrhythmia*, *37*(2), pp.400-406.

2.1 Introduction

Despite the known risks of hematomas and psychological concerns, there is currently no standardized process for assessing scars that form after CIED implantation, apart from manual palpation and visual inspection.

Visual scar assessment is typically performed using subjective scales, such as the Manchester Scar Scale (MSS), which evaluates clinical characteristics of the scar tissue, including color, contour, texture, and more; or patient-reported outcome measures such as the Patient and Observer Scar Assessment Scale (POSAS), that describe patients' assessment of the scar, encompassing visual, tactile, and sensory characteristics of the tissue.[1,2] The methodologies available for scar assessment are observer-dependent and often fail to accurately measure the subjective physical qualities of the scar tissue. New strategies are needed for a comprehensive scar

evaluation method that integrates both objective and subjective characteristics, addressing cosmetic features as well as the functional properties of the tissue.

Of the various scar assessment tools available, the durometer is a well-validated instrument.[3] The durometer measures tissue pliability by applying a vertically directed indentation load to the scar.[4] Initially developed for use in scleroderma, it has also been utilized in assessing burn scar induration.[5]

This study aims to document and evaluate the early stages of scar maturation during surgical wound healing following CIED implantation, using both objective and subjective scale assessments. To our knowledge, a systematic objective assessment of wound healing post-CIED implantation has not been previously reported.

2.2 Methods

This study was part of a prospective observational study, approved by the Institutional Review Board (IRB) for Health Sciences Research (HSR) at the University of Virginia (UVA). IRB-HRS/UVA trial number: 20809. Written informed consent was obtained from all patients.

2.2.1 Patient selection

Patients undergoing CIED procedures at UVA were screened for inclusion. Exclusion criteria included pediatric patients (under 18 years of age), pregnant patients, patients undergoing lead extraction, and implantable loop recorder implants. After the appropriate screening, informed consent was obtained. Device implantation and closure were performed based on physician's discretion.

2.2.2 Implant site assessment

Prior to the surgical procedure, the Model 1600 Type OO Dial durometer (Rex Gauge) was used to measure skin pliability at three sites in the quadrant of the planned implantation and contralateral nonsurgical site. The durometer was positioned perpendicularly on the site of interest, and the measurement, based on the indentation of the mechanical pin, was recorded in standard shore durometer units. On the day after procedure, durometer measurements were taken at the implant site and at the contralateral site. Management of the implant site was left to the discretion of the implanting physician. Routine two-week shoulder restriction was advised. At the two-week post procedure, durometer measurements were repeated, surgical site was assessed MSS and patient survey component of POSAS. Clinical follow-up information was collected from chart review of medical records.

2.2.3 Data analysis

Three durometer readings of each site obtained were averaged for each clinical assessment. An experienced plastic surgeon subsequently evaluated the surgical site to complete MSS and POSAS two-weeks after the procedure. These data were compared to those of 40 healthy volunteers, who served as controls. Control patients had durometer measurements obtained over left and right prepectoral regions with similar assessment as patients. Durometer readings obtained from healthy volunteers and patients were described as mean ± SD. Baseline durometer readings from healthy volunteers and CIED patients were compared using an unpaired two-tailed t test. Post procedure and two-week post procedure durometer readings were compared to contralateral readings for their respective time point using a paired two-tailed t test. In the patient population, one-way ANOVA

was used to assess change in durometer readout over study duration. SAS software was used for performing statistical analysis (Version 9.4 SAS Institute Inc.).

2.3 Results

2.3.1 Skin pliability in patients before the surgery were similar to control population

52 patients undergoing initial CIED placement were enrolled and successfully completed the study. The average age of patient group was 67 ± 14 years, with 14 (26.9%) female and 38 (73.1%) male participants. A control group of forty healthy volunteers with no known cardiac history was also included. The average age of the control group was 21.9 ± 6.77 years, with 16 (40%) female and 24 (60%) male participants. Although the cohort of healthy volunteers were younger, the durometer readings were comparable to patient baseline readings. Preoperative readings in patients at both surgical and contralateral sites were 5.4 ± 2.6 and 5.6 ± 3.1, respectively. As shown in Figure 2.1, these were comparable to readings in healthy controls (5.6 ± 0.6 and 5.6 ± 0.5, P = NS). These baseline values were similar to those in the study evaluating anterior chest wall skin thickness in no scar regions of patients with keloid scars prior to surgical excision and radiation therapy (5.5 ± 1.6).[6]

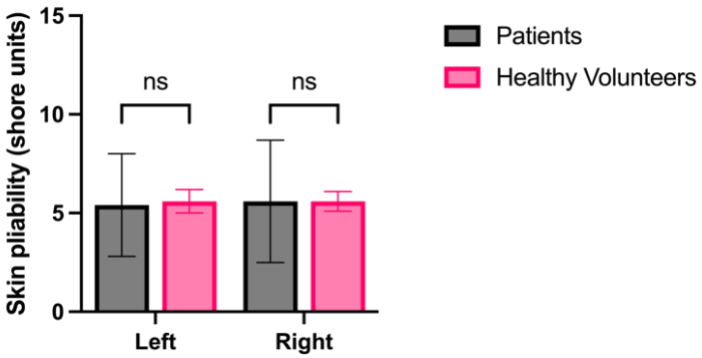

Figure 2.1: Baseline skin pliability measurements. Skin pliability was measured using a durometer, displayed in shore units. No significant difference in skin pliability observed between the left and right sites in healthy volunteers and patients before the procedure. (all $P > .05$).

2.3.2 Increased skin pliability observed one-day post-procedure sustained at two-weeks post-surgery

Skin pliability increased from pre-procedure to post-procedure at both sites. At the surgical site, the mean durometer reading one day post-procedure was 7.5 ± 4, significantly higher than the preoperative mean of 5.4 ± 2.6 ($P = 0.0031$). Similarly, the contralateral site showed a higher postoperative day reading of 7.3 ± 3.2 compared to the preoperative measurement of 5.6 ± 3.1 ($P = 0.0004$). These findings are consistent with prior studies that have shown increased durometer readings for subacute to chronic wounds. [7] While the skin pliability readings at both the surgical and nonsurgical sites were similar during the preoperative and immediate postoperative assessments, the readings at the two-week post-procedure were significantly higher on the surgical side compared to the nonsurgical side ($P < 0.001$) (Figure 2.2).

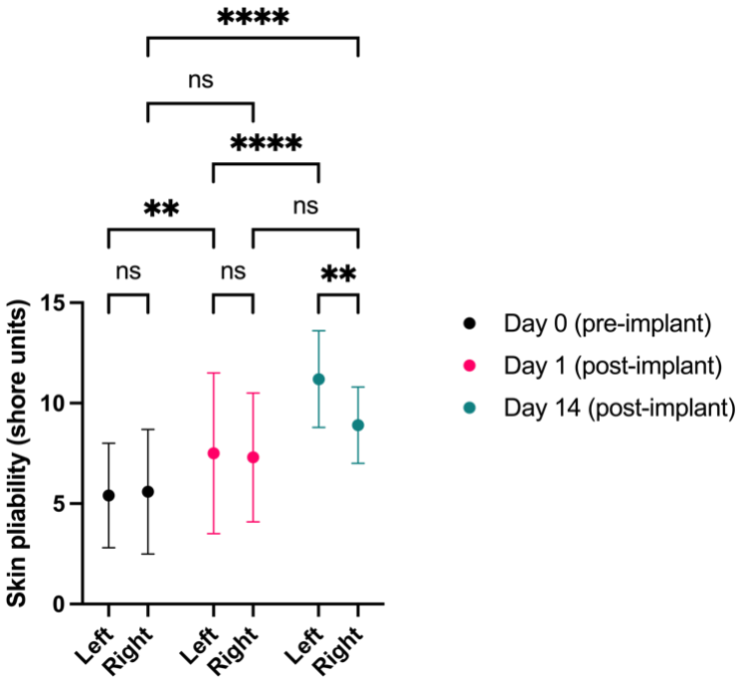

Figure 2.2: Skin pliability changes during early scar maturation post CIED surgery. Skin pliability was higher at both surgical and contralateral sites at Day 1 after surgery in comparison to Day 0. At Day 14 post implantation, skin pliability at surgical site was significantly higher than at Day 1.

2.3.3 Two-Week scar evaluation results using POSAS and MSS

At the two-week follow-up, patient evaluations using the POSAS often described the scar as thin, painless, and hypopigmented with moderate stiffness. In contrast, clinical evaluations performed by a plastic surgeon using the MSS typically reported the scar as palpable and matte, with some distortion and a slight color mismatch. The results suggest that there is a difference in the perception of scar quality between patients and clinical evaluations performed by a plastic surgeon. This discrepancy between patient-reported and clinician-observed scar assessments aligns with findings from previous studies.[8] The mean total scores for POSAS and MSS were 20 ± 8.5 and 9.2 ± 2.5, respectively, indicating a generally higher score (worse scar quality) from the

patient-reported POSAS compared to the clinical MSS evaluation. Importantly, there was no correlation found between the scores and factors such as gender, antiplatelet or anticoagulation regimen, hematoma occurrence, or type of device closure used.

2.4 Discussion

In conclusion, this study emphasizes the importance of developing standardized, integrated assessment protocols that combine clinical assessment, patient-reported evaluation and objective measurements to provide a comprehensive evaluation of scar quality and wound healing post-CIED implantation.

The study highlights a discrepancy between patient-reported and clinician-observed evaluations of scar quality when using subjective scales for scar evaluation. Furthermore, the study confirms the utility of the durometer as an objective tool for measuring skin pliability, which showed significant changes in skin pliability from pre-procedure to post-procedure, and sustained increases at two weeks post-surgery.

Together, these results underscore the need for a comprehensive scar evaluation method that integrates both objective measurements and subjective assessments to address the cosmetic and functional properties of scar tissue effectively.

2.5 Conclusions and future work

This study established baseline objective and scale-based wound assessments for patients undergoing CIED implantation. The findings demonstrated that skin pliability increased significantly from pre-procedure to one day post-procedure at both the surgical and contralateral

sites and remained elevated at the surgical site two weeks post-surgery. These results underscore the importance of early and systematic evaluation of wound healing and scar maturation in patients with CIED implants. Furthermore, the observed increases in durometer readings post-procedure highlight potential mechanisms, including hydration and fluid administration during surgery, which merit further investigation. Consequently, these baseline values may be instrumental in optimizing wound healing in this population. Moreover, early detection of elevated durometer values, which may indicate wound complications, could enable the prompt identification of abnormal wound healing, pocket hematomas, or infections.

Increasing the sample size and including a more diverse population could further enhance the value of the study. Additionally, validation across multiple institutions would add scientific rigor to our initial findings.

2.6 References

(1) Park, J. W.; Koh, Y. G.; Shin, S. H.; Choi, Y.-J.; Kim, W.-S.; Yoo, H. H.; Lee, J. O.; Jang, Y. N.; Kim, J.; Li, K.; Kim, B. J.; Yoo, K. H. Review of Scar Assessment Scales. *Med. Lasers* **2022**, *11* (1), 1–7. https://doi.org/10.25289/ML.2022.11.1.1.

(2) Carrière, M. E.; Mokkink, L. B.; Tyack, Z.; Westerman, M. J.; Pijpe, A.; Pleat, J.; Van De Kar, A. L.; Brown, J.; De Vet, H. C. W.; Van Zuijlen, P. P. M. Development of the Patient Scale of the Patient and Observer Scar Assessment Scale (POSAS) 3.0: A Qualitative Study. *Qual. Life Res.* **2023**, *32* (2), 583–592. https://doi.org/10.1007/s11136-022-03244-6.

(3) Fearmonti, R.; Bond, J.; Erdmann, D.; Levinson, H. A Review of Scar Scales and Scar Measuring Devices. *Eplasty* **2010**, *10*, e43.

(4) Pittar, N.; Winter, T.; Falland-Cheung, L.; Tong, D.; Waddell, J. N. Scalp Simulation – A Novel Approach to Site-Specific Biomechanical Modeling of the Skin. *J. Mech. Behav. Biomed. Mater.* **2018**, *77*, 308–313. https://doi.org/10.1016/j.jmbbm.2017.09.024.

(5) Falanga, V.; Bucalo, B. Use of a Durometer to Assess Skin Hardness. *J. Am. Acad. Dermatol.* **1993**, *29* (1), 47–51. https://doi.org/10.1016/0190-9622(93)70150-R.

(6) Akita, S.; Akino, K.; Yakabe, A.; Imaizumi, T.; Tanaka, K.; Anraku, K.; Yano, H.; Hirano, A. Combined Surgical Excision and Radiation Therapy for Keloid Treatment. *J. Craniofac. Surg.* **2007**, *18* (5), 1164–1169. https://doi.org/10.1097/scs.0b013e3180de62a1.

(7) Van Der Wal, M.; Bloemen, M.; Verhaegen, P.; Tuinebreijer, W.; De Vet, H.; Van Zuijlen, P.; Middelkoop, E. Objective Color Measurements: Clinimetric Performance of Three Devices on Normal Skin and Scar Tissue. *J. Burn Care Res.* **2013**, *34* (3), e187–e194. https://doi.org/10.1097/BCR.0b013e318264bf7d.

(8) Choo, A. M. H.; Ong, Y. S.; Issa, F. Scar Assessment Tools: How Do They Compare? *Front. Surg.* **2021**, *8*, 643098. https://doi.org/10.3389/fsurg.2021.643098.

3 Evaluation of a novel mechanical compression device for improvement of wound cosmesis after CIED implantation.

Portions of this chapter were adapted from the following:

Rojas, E., Morgaenko, K., Brown, L., Kim, S., Mazimba, S., Malhotra, R., Darby, A., Monfredi, O., Mason, P., Mangrum, J.M. and Haines, D.E., 2022. Evaluation of a novel mechanical compression device for hematoma prevention and wound cosmesis after CIED implantation. Pacing and Clinical Electrophysiology, 45(4), pp.491-498.

3.1 Introduction

Up to 35% of patients undergoing CIED procedures are prescribed antiplatelet and/or anticoagulant therapies, which significantly increase the risk of hematoma formation.[1] Hematoma development is associated with a heightened risk of device infection, one of the most serious CIED complications.

The application of pressure to the postoperative wound aims to prevent hematoma formation by optimizing the wound healing process. This is achieved by enhancing local blood flow and increasing the production of granulation tissue.[3,4] Previous guidelines for post-CIED surgery wound care have outlined efforts to prevent hematoma formation, such as cauterizing bleeding sites, irrigating the pocket, and using pressure dressings after skin closure.[5,6] For general wounds, the applied pressure typically ranges from 50 mmHg to 125 mmHg.[7,8] However, the pressure exerted by conventional dressings has not been quantitatively assessed, and an optimal pressure for post-CIED surgery has not yet been established.

This study aimed to evaluate the effectiveness of a novel compression device, designed to deliver consistent pressure to the surgical site, in comparison to conventional strategies for patients undergoing cardiac device implantation.

3.2 Methods

An open, prospective, randomized, single-center clinical trial was conducted on patients who underwent cardiac device implantation at the University of Virginia (UVA) Medical Center between January 2020 and May 2020. IRB-HRS/UVA trial number: 21759. This study received approval from the University of Virginia Institutional Review Board, and written informed consent was obtained from all participants.

3.2.1 Study design and participants

Patients at UVA Medical Center scheduled for de novo implantation of a CIED, or generator replacement were invited to participate in the study and screened for eligibility. Exclusion criteria included pediatric patients (under 18 years of age), recent sternotomy and chest, shoulder or abdominal surgery precluding the placement of a novel compression device. After the appropriate screening, written informed consent was obtained from 112 patients. Device implantation and closure were performed based on physician's discretion.

After the initial assessment for enrollment, 112 patients were randomized using the UVA Online Collaborative Research Environment tool. Of these, 56 patients were allocated to the treatment group and received a novel compression device applied to the surgical site post-procedure, while the remaining 56 patients were assigned to the control group and received a standard care bandage. In the treatment group, four patients had their procedures canceled, delayed, or postponed, and one patient chose to withdraw from the study. Consequently, 51 patients

in the treatment group were included in the final analysis. In the control group, two patients had their procedures postponed, resulting in a total of 54 patients in the control group included in the final analysis.

3.2.2 Application of postoperative dressings and pressure regimens in study groups

Patients assigned to the treatment group had a novel compression device applied on top of the medical bandage Primapore (Smith+ Nephew, Memphis, Tennessee) or Aquacel (ConvaTec, Bridgewater, NJ) over the surgical site for a minimum of two hours. Patients randomized to the control group received the standard of care at the physician's discretion, which included either (i) a medical bandage Primapore (Smith+ Nephew, Memphis, Tennessee) or Aquacel (ConvaTec, Bridgewater, NJ) over the surgical site; or (ii) a conventional pressure dressing (a stack of gauze with tape for compression) on top of the medical bandage.

3.2.3 Design and application of the novel compression device

Novel compression device (Patent# 17/108541 Pressure Apparatus to Reduce Swelling After Medical Device) is a modular biocompatible, transparent, lightweight, and durable pneumatic compression device that was designed to deliver sufficient pressure consistently over a 2−4 hours application period and accommodate varying upper body anatomy. Device compression system is a modular assembly consisting of (i) Pneumatic compression system (transparent air inflation mechanism with inflatable bulb (Dyad Medical Sourcing, LLC, Bannockburn, IL) with air release valve, custom made for this trial using medical grade thermoplastic polyurethane (shore 90A material), (ii) Fixation mechanism (skin safe adhesive pads Stetrix (Tissue Management Solutions Bartlett, TN) with light weighted fabric slings which connect the compression system to

the pads, (iii) Pressure monitoring mechanism (pressure gauge with read-out scale, Varodem (The Compression Company Horn, Netherlands). The compression system enables application of pressure up to 160 mmHg, additionally allowing complete surgical site inspection owing to transparent material. The pressure valve apparatus can be easily detached from the air inflation module after complete inflation and sealing the pressure valve.

The novel compression device (Patent #17/108541, Pressure Apparatus to Reduce Swelling After Medical Device) is a modular, biocompatible, transparent, lightweight, and durable pneumatic compression device. It is designed to consistently deliver sufficient pressure over a 2–4-hour application period and accommodate varying upper body anatomies. The device's compression system consists of three modular components: (i). Pneumatic Compression System: This includes a transparent air inflation mechanism with an inflatable bulb (Dyad Medical Sourcing, LLC, Bannockburn, IL) and an air release valve custom-made for this trial using medical-grade thermoplastic polyurethane (shore 90A material) (Figure 3.1). The compression system can apply pressure up to 160 mmHg and allows complete inspection of the surgical site due to its transparent material. The pressure valve apparatus can be easily detached from the air inflation module after complete inflation, sealing the pressure valve. (ii) Fixation Mechanism: Skin-safe adhesive pads (Stetrix, Tissue Management Solutions, Bartlett, TN) and lightweight fabric slings connect the compression system to the pads, ensuring secure attachment. (iii) Pressure Monitoring Mechanism: A pressure gauge with a read-out scale (Varodem, The Compression Company, Horn, Netherlands) allows for accurate pressure monitoring.

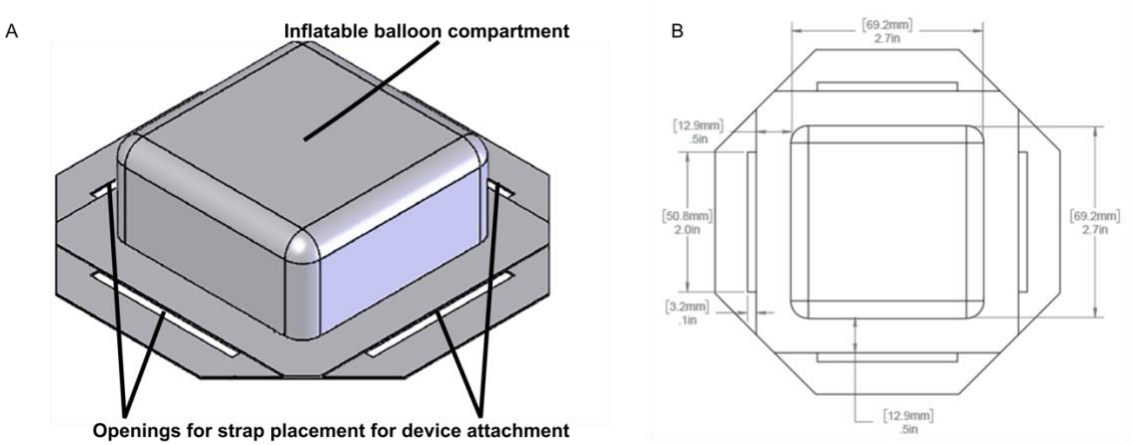

Figure 3.1: Design of the Novel Compression Device. (A) A bottom-up view of the device model. The balloon compartment is positioned over the surgical wound to enable pressure application. Openings for strap placement allow for adjustments to accommodate individual patient anatomy. (B) Dimensions of the device.

A trained operator applied and removed the novel compression device. The pressure exerted on the surgical site was calibrated to 40 mmHg. Pressure readings were taken every 30 minutes using a sub-bandage pressure measuring sensor (Kikuhime, MediTrade, Soro, Denmark). The pressure transducer was calibrated before each measurement.

3.2.4 Implant site assessment

Before the procedure, trained study investigators used a Model 1600 Type OO Dial durometer (Rex Gauge, IL) to measure skin pliability at the surgical site (S) and the contralateral site (CL) at four time points: 1) pre-procedure (baseline), 2) within 24 hours post-procedure, 3) at the 2-week follow-up, and 4) at the 3-month follow-up visit. Three readings were taken from each quadrant of interest, and the average value was used for analysis.

After the removal of the novel compression device, patients completed a postoperative survey that assessed various aspects of their experience with the device.

At the 2-week and 3-month follow-up periods, wound healing was assessed using the Manchester Scar Scale (MSS) and the Patient and Observer Assessment Scale (POSAS). The physician component of these assessments was evaluated by a blinded plastic surgeon.

3.2.5 Endpoints of interest

The primary endpoint was the incidence of postoperative pocket hematoma in patients using the hematoma prevention device compared to the control group. Secondary endpoints included skim pliability readings, POSAS and MSS scores, rates of CIED revision, and CIED infection rates. The analysis of surgical site hematoma was conducted according to the Bleeding Academic Research Consortium classification.[2]

3.2.6 Data analysis

Quantitative data were expressed as the mean ± standard deviation and median ± percentiles. Based on the distribution of the data points, comparisons between groups were performed using an unpaired Student's *t*-test or U-Mann Whitney test. Comparisons of means from the same individual were performed using a paired Student's *t*-test. Categorical data were compared by Chi-Square test. One-way ANOVA was used to assess changes in durometer readings over time in both groups. *P* values of less than 0.05 were deemed to be significant. Data were analyzed according to the intention-to-treat model. SAS software was used for performing statistical analysis (Version 9.4, SAS Institute Inc.).

3.3 Results

3.3.1 Novel compression device delivers consistent pressure over a 4-hour application period

First, we assessed the pressure exerted by both the conventional pressure dressing and the novel compression device on healthy volunteers. The mean pressure applied by the conventional pressure dressing was 4.91 mmHg, with approximately a 10% reduction in pressure every 30 minutes. In contrast, the novel compression device, set to an initial pressure of 40.00 mmHg, consistently maintained a pressure exhibiting only a 2.5% reduction every 30 minutes. Therefore, while the conventional pressure dressing failed to deliver substantial and sustained pressure, the novel compression device effectively provided consistent pressure over the application period (Figure 3.2).

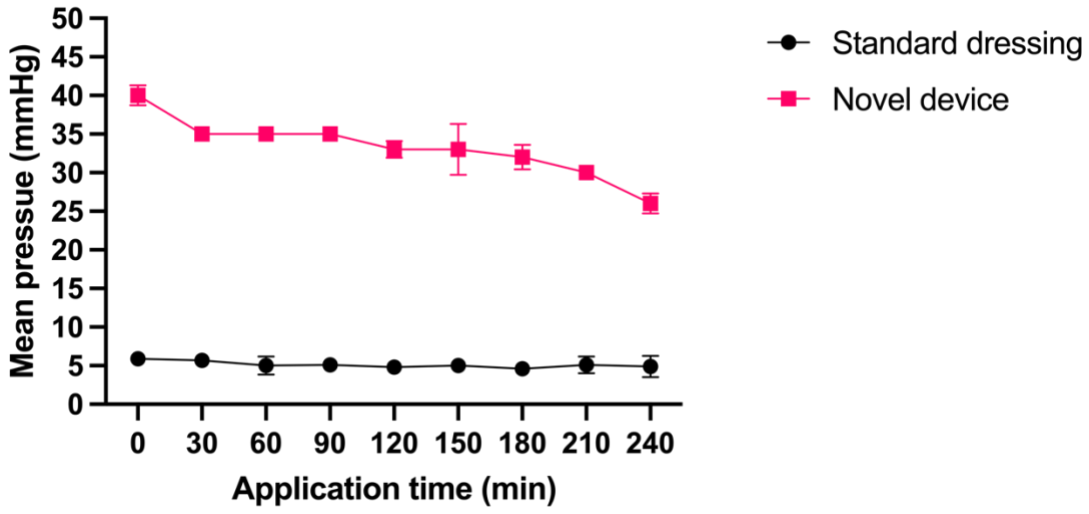

Figure 3.2: Comparison of pressure applied by conventional dressing and novel device. *M*ean pressure delivered to the chest by the conventional dressing and a novel compression device over four hours of application.

These results showed that the conventional pressure dressing applied a pressure within a range from 3 to 7 mmHg. Given that the venous pressure exceeds 20 mmHg and the mean arterial pressure is at least 60 mmHg, the pressure delivered by conventional dressings is insufficient to counteract venous or arterial pressure effectively.

3.3.2 Clinical evaluation of the novel compression device

Having confirmed the consistency of pressure application by the novel compression device in healthy volunteers, we proceeded to evaluate its performance in a clinical setting. The average pressure delivered by the device to the post-surgical wound was 34.68 mmHg. Patients in the treatment group were surveyed to assess their tolerability and overall experience with the device, yielding a mean score of 7.6 ± 2.8. Reports of pain, pressure, and discomfort were minimal, and no major adverse events were associated with the use of the novel compression device (Table 3.1). Furthermore, there were no instances of patients needing to remove the device due to intolerance.

Surveyed questions	**Mean ± SD**
Pressure	2.16 ± 3.2
Pain	1.65 +/− 2.9
Itching	0.29 ± 0.8
Soreness	1.43 ± 2.8
Decreased mobility	0.83 ± 2.2
Discomfort	1.62 ± 2.7
Device removal	3.08 ± 3.3
Overall experience (0 to 10 being 10 the best possible experience)	7.6 ± 2.8

Table 3.1: Patients response to novel compression device. The table presents the mean and standard deviation of patients' responses to surveyed questions. Experience rated on a scale from 0 to 10 (with 10 being the best possible experience).

Throughout the study, there were 11 hematoma occurrences at the surgical site post-CIED implantation, with eight in the control group and three in the treatment group (14.8% vs. 5.9%, p = 0.27) (Table 3.2).

	Control group: Conventional dressing, n = 54	**Treatment group: Novel compression device, n = 51**	**p-value**
Hematoma	14.8% (*n* = 8)	5.9% (*n* = 3)	0.20 (Fisher's)
Antiplatelet	63.0%	43.1%	0.04*
Anticoagulation	42.6%	58.8%	0.09
Immunosuppression	3.7%	5.9%	0.11

Table 3.2: Comparison of outcomes between treatment and control groups. * Indicates statistically significant difference.

Although the hematoma occurrence rate was lower in the treatment group, this difference was not statistically significant. Due to the overall low incidence of hematomas in this study, we believe that further research involving larger patient populations is needed to more accurately determine the clinical effectiveness of the novel compression device.

3.3.3 Comparison of pre- and post-procedural skin pliability measurements in treatment group and control cohorts

Pre-procedural skin pliability measurements at both the surgical and contralateral sites were similar between the treatment and control groups (4.2 ± 2.2 vs. 4.8 ± 2.7 and 4.6 ± 2.1 vs. 5.3 ± 2.7, respectively; p = NS). However, post-procedural measurements at the surgical site were

significantly higher in the control group compared to the treatment group (7.50 ± 3.45 vs. 5.37 ± 2.78; $p < 0.01$) (Figure 3.3).

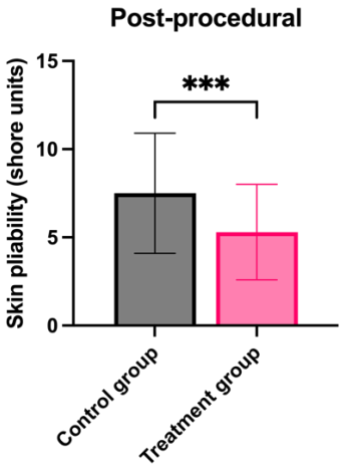

Figure 3.3: Post-procedural measurements of skin pliability. Post-procedural measurements at the surgical site showed significantly higher values in the control group compared to the treatment group.

This result indicates that the novel compression device provided adequate compression and dispersion of surgical swelling, potentially reducing skin tension and promoting better scar healing.

3.3.4 Treatment group reported improvement of the surgical site cosmetic appearance

Significantly lower MSS scores were observed in the treatment group at the two-week follow-up ($p = 0.03$), indicating a better cosmetic appearance and improved wound healing compared to the control group. Meanwhile, POSAS scores, which reflect patient-reported outcomes, were comparable between both groups at both the two-week and three-month follow-ups. Together these results indicate that despite the clinical improvements observed with the MSS

in the treatment group, patients' subjective assessments of their scars were similar across both groups over time (Figure 3.4).

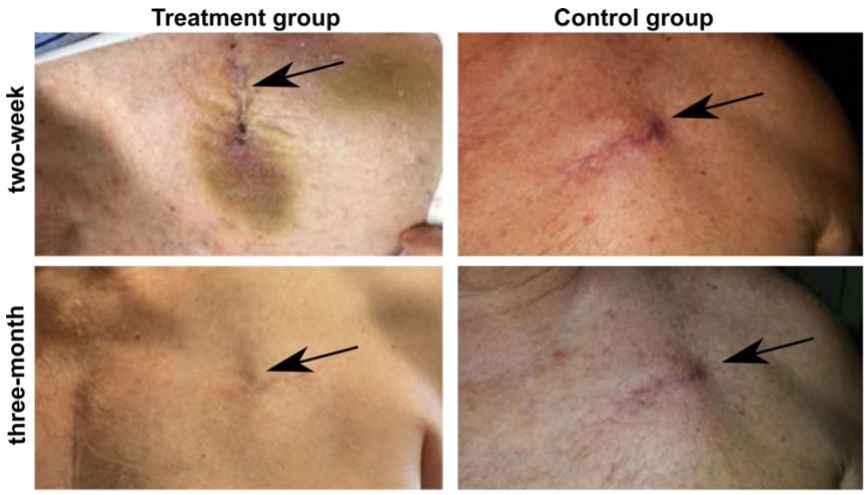

Figure 3.4: Representative images of post-CIED incision. The appearance of post-CIED surgery scars in the treatment group and control group after two weeks and three months post-surgery.

3.4 Discussion

In this study we designed the novel compression device to address the limitations of existing mechanical compression devices, which obstruct visual access to the site and lack the ability to deliver consistent pressure and/or adjust pressure levels. Additionally, most alternative solutions for mechanical compression are site-specific. The modular assembly of the novel compression device allows for universal site application. Furthermore, to our knowledge, there is currently no mechanical compression device for CIEDs that can dynamically adjust pressure.

In this randomized clinical trial, we evaluated the performance and clinical effectiveness of a novel compression device designed for postoperative wound care in patients undergoing CIED implantation. The novel compression device delivered consistent pressure over a 4-hour

application period, maintaining a mean pressure of 33.68 mmHg. This consistency was significantly better than that of conventional pressure dressings, which failed to maintain adequate pressure. In a clinical setting, the device maintained an average pressure of 34.68 mmHg on the post-surgical wound. The treatment group exhibited a lower, although not statistically significant, incidence of hematomas compared to the control group (5.9% vs. 14.8%). Patient surveys indicated good tolerability and a positive overall experience with the device, with minimal reports of pain or discomfort and no major adverse events.

Additionally, we demonstrated that durometer can be used to reliably measure skin pliability in patients post-CIED surgery. We found that four-hour application of the novel compression device resulted into the lower skin pliability, indicating that applied compression lead to reduced swelling. This suggests that the novel device may contribute to improved scar healing by reducing skin tension.

Overall, the results of this study demonstrate the potential of the novel compression device to enhance postoperative wound care by providing consistent pressure and improving cosmetic outcomes.

3.5 Conclusions and future work

The results of this study demonstrate the potential of the novel compression device to enhance postoperative wound care by providing consistent pressure and improving cosmetic outcomes. However, due to the small sample size and single-center design, further research is necessary to validate these findings and establish the device's clinical effectiveness on a larger scale. Future studies should also focus on long-term outcomes, including the incidence of device infections and the durability of cosmetic improvements. Furthermore, additional research is needed to determine the optimal pressure settings for different age populations among CIED patients.

3.6 References

(1) Cabell, C. H.; Heidenreich, P. A.; Chu, V. H.; Moore, C. M.; Stryjewski, M. E.; Corey, G. R.; Fowler, V. G. Increasing Rates of Cardiac Device Infections among Medicare Beneficiaries: 1990–1999. *Am. Heart J.* **2004**, *147* (4), 582–586. https://doi.org/10.1016/j.ahj.2003.06.005.

(2) Mehran, R.; Rao, S. V.; Bhatt, D. L.; Gibson, C. M.; Caixeta, A.; Eikelboom, J.; Kaul, S.; Wiviott, S. D.; Menon, V.; Nikolsky, E.; Serebruany, V.; Valgimigli, M.; Vranckx, P.; Taggart, D.; Sabik, J. F.; Cutlip, D. E.; Krucoff, M. W.; Ohman, E. M.; Steg, P. G.; White, H. Standardized Bleeding Definitions for Cardiovascular Clinical Trials: A Consensus Report From the Bleeding Academic Research Consortium. *Circulation* **2011**, *123* (23), 2736–2747. https://doi.org/10.1161/CIRCULATIONAHA.110.009449.

(3) Xia, C.-Y.; Yu, A.-X.; Qi, B.; Zhou, M.; Li, Z.-H.; Wang, W.-Y. Analysis of Blood Flow and Local Expression of Angiogenesis-Associated Growth Factors in Infected Wounds Treated with Negative Pressure Wound Therapy. *Mol. Med. Rep.* **2014**, *9* (5), 1749–1754. https://doi.org/10.3892/mmr.2014.1997.

(4) Banwell, P. E.; Téot, L. Topical Negative Pressure (TNP): The Evolution of a Novel Wound Therapy. *J. Wound Care* **2003**, *12* (1), 22–28. https://doi.org/10.12968/jowc.2003.12.1.26451.

(5) Baddour, L. M.; Epstein, A. E.; Erickson, C. C.; Knight, B. P.; Levison, M. E.; Lockhart, P. B.; Masoudi, F. A.; Okum, E. J.; Wilson, W. R.; Beerman, L. B.; Bolger, A. F.; Estes, N. A. M.; Gewitz, M.; Newburger, J. W.; Schron, E. B.; Taubert, K. A.; Council on

Cardiovascular Surgery and Anesthesia; Council on Cardiovascular Nursing; Council on Clinical Cardiology; the Interdisciplinary Council on Quality of Care and Outcomes Research. Update on Cardiovascular Implantable Electronic Device Infections and Their Management: A Scientific Statement From the American Heart Association. *Circulation* **2010**, *121* (3), 458–477. https://doi.org/10.1161/CIRCULATIONAHA.109.192665.

(6) Baddour, L. M.; Esquer Garrigos, Z.; Rizwan Sohail, M.; Havers-Borgersen, E.; Krahn, A. D.; Chu, V. H.; Radke, C. S.; Avari-Silva, J.; El-Chami, M. F.; Miro, J. M.; DeSimone, D. C.; on behalf of the American Heart Association Council on Lifelong Congenital Heart Disease and Heart Health in the Young (Young Hearts); and Council on Clinical Cardiology. Update on Cardiovascular Implantable Electronic Device Infections and Their Prevention, Diagnosis, and Management: A Scientific Statement From the American Heart Association. *Circulation* **2024**, *149* (2). https://doi.org/10.1161/CIR.0000000000001187.

(7) Vikatmaa, P.; Juutilainen, V.; Kuukasjärvi, P.; Malmivaara, A. Negative Pressure Wound Therapy: A Systematic Review on Effectiveness and Safety. *Eur. J. Vasc. Endovasc. Surg.* **2008**, *36* (4), 438–448. https://doi.org/10.1016/j.ejvs.2008.06.010.

(8) Ubbink, D. T.; Westerbos, S. J.; Nelson, E. A.; Vermeulen, H. Authors' Reply: A Systematic Review of Topical Negative Pressure Therapy for Acute and Chronic Wounds (*Br J Surg* 2008; 95: 685–692). *Br. J. Surg.* **2008**, *95* (9), 1186–1186. https://doi.org/10.1002/bjs.6363.

4 Conclusions and future directions

In summary, this study highlights the necessity for development of comprehensive scar evaluation methods that integrate both objective and subjective characteristics. Given the current lack of standardized processes for assessing scars post-CIED implantation, future work should focus on the development and validation of integrated assessment protocols that combine clinical evaluations, patient-reported outcomes, and objective measurements like durometer readings. This will provide a comprehensive framework for systemic assessing scar quality and wound healing post-CIED implantation and capture the subjective experiences of patients, addressing both cosmetic concerns and functional properties of the scar tissue.

Furthermore, in this work we demonstrated the potential of a novel compression device to enhance postoperative wound care by providing consistent pressure, reducing skin tension, and improving cosmetic outcomes. In contrast to existing compression dressing techniques, this novel device enables visual access to the surgical site and offers a dynamic pressure adjustment. Future studies are needed to identify the optimal pressure levels for preventing hematoma formation and promoting effective wound healing specifically for post-CIED surgery. Research should include a range of pressures to find the most effective level that balances efficacy and patient comfort.

Future research into the development of smart compression devices that can dynamically adjust pressure based on real-time feedback from the wound site could offer significant advancements. These devices could provide personalized wound care tailored to individual patient needs and responses.

5 Introduction to the role of tumor-draining lymph nodes in breast cancer

5.1 Breast cancer represents a global health concern

Breast cancer is the most frequently diagnosed cancer in women globally, and its incidence has been increasing steadily over recent decades.[1] In 2022, approximately 2.3 million women worldwide were diagnosed with breast cancer, resulting in 665,684 deaths (Figure 5.1A).[2] Projections suggest a significant increase in cases by 2040, with new diagnoses expected to surge by over 40% to about 3 million annually (Figure 5.1B). Similarly, deaths related to breast cancer are anticipated to grow by more than 50%, from 666,000 in 2022 to 1 million by 2040 (Figure 5.1C).[1]

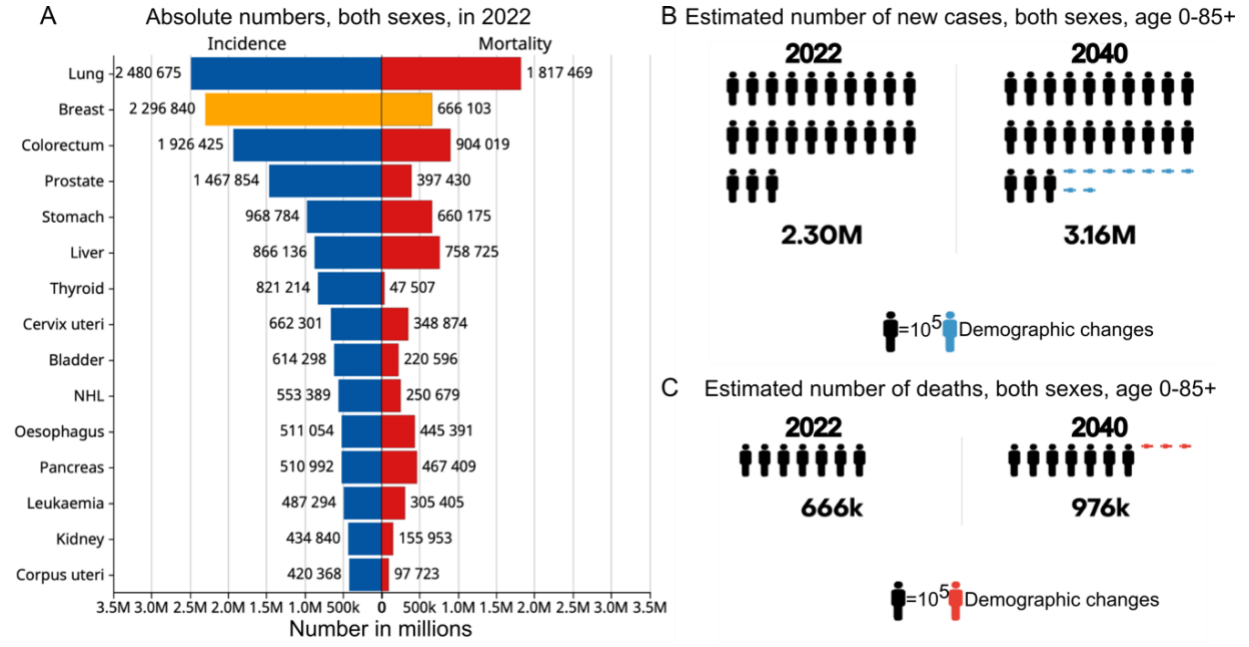

Figure 5.1: Breast cancer incidence and mortality from 2022 to 2040. (A) Estimated numbers of new cancer cases (incidence) and deaths (mortality) in 2022. (B) Estimated numbers of new breast cancer cases in 2022 and 2040. (C) Estimated numbers of breast cancer related deaths in 2022 and 2040. Source: GLOBOCAN 2022.

5.2 The role of lymphatic system in metastatic spread of breast cancer

The majority of breast cancer mortalities are caused by metastasis — the spread of tumor cells leading to secondary malignant growths in anatomically distant organs.[3] The rate of metastasis has been increasing, with 20–30% of breast cancer patients developing metastatic disease after the initial diagnosis and treatment of their primary tumor.[4] While surgical resection and adjuvant therapies can effectively treat primary tumors, metastatic disease remains largely incurable due to its systemic spread and accounts for 90% of all cancer-related deaths.[5] In breast cancer, metastatic disease remains the underlying cause of mortality, and occurs predominantly via vascular invasion in lymphatics,[6] with an 8-fold higher invasion than in blood vessels.[3] The lymphatic system, a vital component of the circulatory system, plays an essential role in maintaining tissue-fluid balance and supporting immune functions.[7] Under normal physiological conditions, the lymphatic system is essential for transport of lymph — a fluid mixture of extracellular fluids, proteins, soluble antigen and immune cells — to draining lymph nodes (LNs) for immune surveillance. Once surveilled, efferent lymphatic vessels carry filtered lymph to other LNs or back into the venous system.[8] Tumor cells can exploit the lymphatic system as a conduit to spread and colonize draining LNs, and/or as a gateway for dissemination to distant organs (Figure 5.2).[9,10]

The sentinel lymph node (SLN), a first tumor-draining lymph node (TDLN) located downstream from the primary cancer site, is the first organ tumor cells encounter passing through the lymphatic vessels and potential niche for initial metastatic seeding.[11] Biopsy of the SLNs a standard practice for many solid tumors, with the identification of tumor cells in the SLNs serving

as a critical predictor of cancer outcomes.[12] It plays a key role in determining disease staging and guiding therapeutic strategies.[13,14] At diagnosis 27% of breast cancer patients have detectable TDLN metastasis,[4] and the presence of TDLN metastasis is linked to poorer survival outcomes compared to patients without nodal involvement.[15]

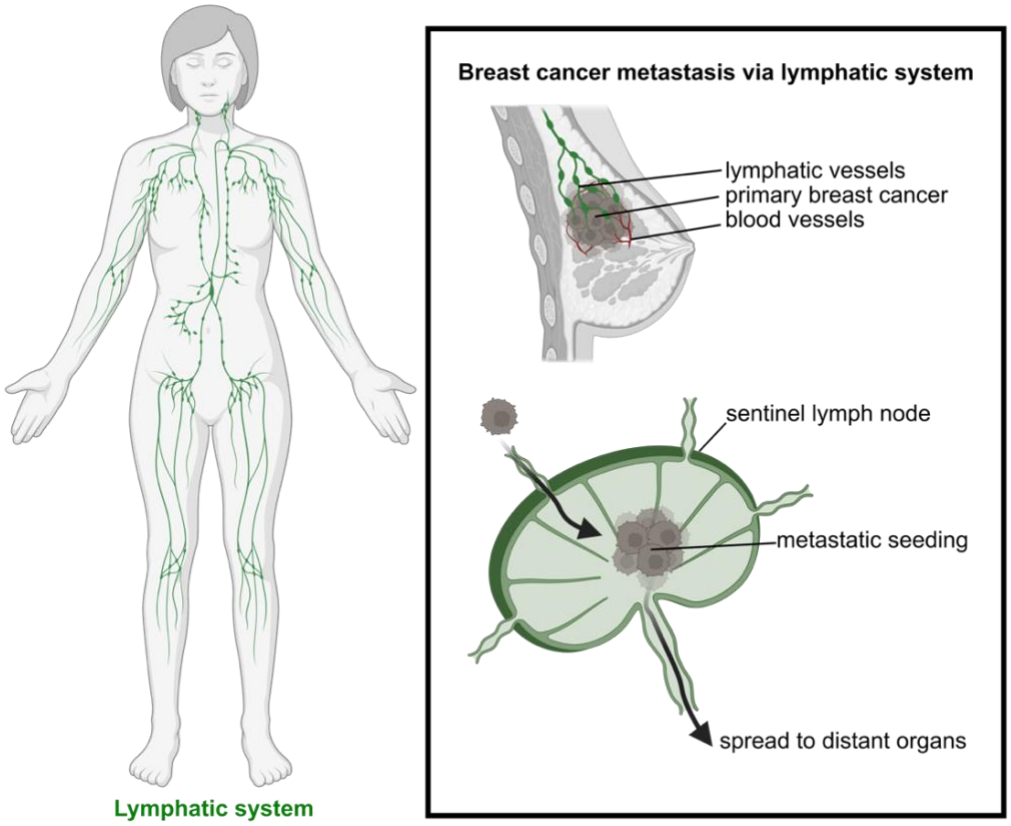

Figure 5.2: Metastatic progression of primary breast cancer through the lymphatic system. Metastatic cells that exit primary tumor use lymphatic vessels to gain access to the SLN, enabling spread to distant organs. Created with BioRender.

While the colonization of distant organs is not solely dependent on initial TDLN infiltration, invasion of the TDLN is believed to facilitate metastatic progression by inducing immune tolerance and creating a conducive environment in distant organs that favors metastatic colonization.[16]

5.3 The TDLNs are crucial for generating anti-tumor immunity

LN are secondary lymphoid organs that act as hubs for the immune system, coordinating lymphocytes to mount adaptive immune responses. During the early stages of primary tumor development, tumor-associated (neo)antigens are presented in TDLN, initiating the priming of T cells.[17] Over the last decade, it has become evident that TDLN are dynamic structures that, in response to the upstream tumors, may create microenvironments that both promote metastasis and impede immune surveillance,[18–20] or control elimination of cancer at the early stages of tumor development.[21–23]

Recent studies highlight the critical role of TDLNs in supporting the survival and antigenic priming of CD8+ T cells, as well as initiating systemic anti-tumor T cell responses, which can enhance the effectiveness of immune checkpoint blockade (ICB) immunotherapy such as atezolizumab, a monoclonal antibody against programmed cell death ligand 1 (PDL1).[24–27] An increasing number of studies are investigating the potential of therapeutic strategies that involve the localized administration of immune-modulating agents to the TDLNs.[28–31]

5.4 Stromal cells optimize structure of LNs for immunosurveillance and generation of effective immune responses

Soluble antigens and proteins are carried by the lymph to the afferent lymphatic vessels of LN. The subcapsular sinus (SCS), lined by a layer of endothelial cells, sorts incoming particulate by size. Large material is sampled by SCS macrophages, while small particulate (< 70kDa) enters the conduit system for surveillance by resident dendritic cells. It percolates through a network of

conduits formed by stromal cells subsets — follicular dendritic cells (FDCs) in the B cell zone (cortex) and fibroblast reticular cells (FRCs) in the T cell zone (paracortical area), before moving into the medullary sinus and exiting the LN through efferent lymphatic vessels.[32,33] The interconnected network of conduits functions as a molecular sieve, setting up a size exclusion for incoming lymph, which permits only small molecules and particles such as antigens and inflammatory mediators to pass through.[34] Additionally, the compartmentalization structured by FDCs and FRCs facilitate interactions between T and B cells and their antigen-presenting cells (APCs), promoting clonal expansion.[35]

Blood-circulating lymphocytes enter the LN through high endothelial venules (HEVs), a specialized blood endothelial cells (BECs) producing molecules that help facilitate cell entry. Following entry through HEVs blood-circulating lymphocytes appear in the paracortical areas and following the gradients of different chemoattractant molecules home to their respective areas. Upon activation, T cells will migrate out of the LN through the medullary sinuses and subsequently exit via the efferent lymphatic vessels.[36] The efferent lymphatic vessel ultimately drains into the thoracic duct, enabling lymphocytes to enter the bloodstream and circulate through peripheral lymphoid organs (Figure 5.3).

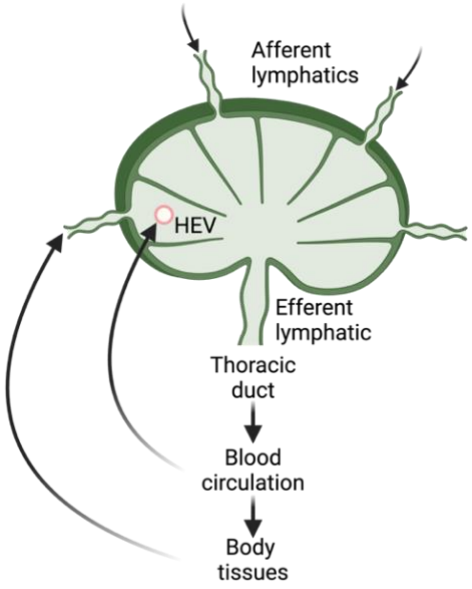

Figure 5.3: Lymphocyte circulation path. Afferent lymphatic vessels transport lymphatic material to the LN. Efferent lymphatic vessels drain into the thoracic duct, allowing lymphocytes to re-enter the bloodstream and circulate through the peripheral organs. Created with BioRender.

Thus, LNs are complex structures featuring distinct compartments with unique microanatomical characteristics, including lymphatic sinuses, T-cell zones, and B-cell zones. The organization of LNs is supported by resident stromal populations, which fulfill two key roles:

(i) Structural — they provide a functional scaffold.

(ii) Immune regulatory — they deliver critical guidance cues and survival signals for leukocyte interactions.

Together, these functions of stromal cell allow for positioning of lymphocytes into the specific zones, enabling efficient immune surveillance.[37,38]

5.5 Lymphocyte homing chemokines are widely implicated as mediators of lymphatic metastasis

Complex cellular organization of the LN is controlled by stromal cell subsets of LN which provide microanatomical structures and establish local gradients of chemokine cues. These lymphoid chemokines direct the homing of immune cells into distinct compartments within the LNs.[39] Chemokines are secreted proteins that act as chemoattractants to cells expressing cognate receptors, causing them to become polarized and crawl toward the source of the attractant. Chemokines are classified into two related yet structurally distinct groups: CC chemokines, characterized by two adjacent cysteine residues near the amino terminus, and CXC chemokines, where these cysteine residues are separated by a single amino acid.[40] Each group targets a different set of G-protein-coupled receptors.[41]

There is strong evidence supporting the role of chemokines in facilitating tumor cell migration from the site of the tumor into the lymphatics and TDLNs. Tumor cells can exploit chemokine-directed signaling to aid in their metastatic spread, often utilizing homing mechanisms designed for leukocytes (Table 5.1). In previous work on melanoma metastasis, Shields et al. has shown that CCL21 chemokine secreted by lymphatic endothelial cells (LEC), stimulates chemotactic migration in metastasizing cells.[42] In in vivo model of melanoma metastasis in TDLN, it was established that tumor cell expression of CCR7 cognate chemokine receptor lead to significant increase of TDLN invasion.[43] Furthermore, clinical research reported a positive correlation between the expression of CCR7 in tumors and an increased risk of LN metastasis in breast cancer.[44] Moreover, in patients with pancreatic ductal adenocarcinoma, tumors lacking CCR7 receptor expression exhibit diminished metastatic dissemination.[45] CCL1 chemokine secreted by the LECs of LN was shown to promote active migration of melanoma cells allowing

tumor cells to enter TDLN and establish metastatic seeding within the SCS later spreading into the deeper parenchyma.[46] Müller et al. demonstrated the role of signaling though CXCL12/CXCR4 chemokine axis in determining the metastatic site of breast tumor cells and showed that antibody blockade of CXCR4 receptor effectively hindered breast cancer metastasis to the lungs or LNs in mice.[47] Moreover, in breast cancer patients, tumors with high expression levels of the cognate chemokine receptor CXCR4 are associated with extensive lymphatic spread, showing a significant correlation with the degree of LN metastasis.[48–51] Additionally, the CXCL13/CXCR5 signaling axis has been reported as a regulator of epithelial-to-mesenchymal transition during LN metastasis in breast cancer.[52] Collectively, these studies suggest the involvement of chemokine signaling in navigating tumor invasion towards lymphatics and LNs.

Table 5.1: Role of chemokines regulating immune cell trafficking in the cancer lymphatic invasion and LN metastasis.

Chemokine ligand	CCL21, CCL19	CCL1	CXCL12	CXCL13
Chemokine receptor	CCR7	CCR8	CXCR4, CXCR7	CXCR5
Producing stromal cells	FRCs, HEVs, LECs	LECs	FRCs, FDCs, HEVs	FRCs, FDCs, HEVs
Anatomical location in LN	T cell zone, T : B cell border , T-cell zone-medulla border	SCS	T : B cell border, T-cell zone-medulla border, dark zone in germinal centers	T : B cell border, SCS, light zone in germinal centers
Function in homeostasis	Regulation of T and DC cell trafficking into LNs [57]	Recruitment of regulatory T cell [59]	Regulating B cell trafficking into LNs; [57] germinal center dark zone support [55]	Regulating B cell trafficking into LNs;[53,54] germinal center light zone support [55,56]
Function in LN metastasis	Mediates tumor cell migration toward lymphatic vessels [61]	Controls tumor cell entry to LN;[46] Immunosuppression of regulatory T cells [60]	Regulates tumor metastasis through establishment of premetastatic niche [58] 6/22/2024 8:17:00 PM6/22/2024 8:17:00 PM	regulates epithelial to mesenchymal transition of tumor cells during LN metastasis [51]

Despite growing evidence of the influence of LN produced chemokines on the metastatic potential of tumor cells, the spatiotemporal dynamics of tumor invasion after reaching the SCS remain poorly understood. It remains unclear which regions of the LN are preferentially invaded by cancer cells in the absence of lymphatic barriers, to what extent cancer cells invade chemokine-rich domains and whether blockade of chemokine signaling could be sufficient to modulate LN metastasis.

5.6 TDLNs undergo structural and functional remodeling in response to the upstream tumor

Structural changes of TDLN include lymphangiogenesis and dilation of the SCS prior metastatic seeding, [62,63] expansion and remodeling of HEVs,[64,65] and fibrosis of the FRC conduit network.[66] During acute inflammation, despite substantial remodeling of FRC network, conduits preserve their size exclusion properties and decrease tension to support LN enlargement and lymphocyte influx.[67] Conversely, FRC remodeling in TDLNs is characterized by widening of the conduits and a loss of size exclusion properties,[66] increase of extracellular matrix collagen and hyaluronic acid,[68] causing increased solid stress and impaired lymphocyte infiltration.[69] Additionally, FRC reprogramming to bile and fatty acid metabolism,[70] along with the production of fumarate, succinate, and 2-hydroxyglutarate oncometabolites, supports an immunosuppressive environment in the TDLN.[71]

Tumor-derived extracellular vesicles (tdEVs) drain to the TDLN and localize in the SCS, inducing remodeling of extracellular matrix and expression of adhesion molecules. This prepares a favorable environment for tumor cell seeding, as injected tumor cells invade at the sites of EVs accumulation.[72,73]

Cellular composition of TDLN also changes over the course of tumor development. T cells and myeloid cells such as macrophages, neutrophils, and antigen-presenting dendritic cells primed in the tumor accumulate selectively in the downstream TDLN, where their effects may be either activating or immunosuppressive.[74,75]

In conclusion, structural, molecular, and cellular changes occur within the TDLN prior to onset of metastasis, altering its biochemical environment and functionality. These changes may create conditions that favor metastasis and install mechanisms of immune suppression. Mapping the spread of tumor cells in the distinct regions of the LN (Figure 5.4) would enable identification of factors creating locally permissive microenvironments, and thus could reveal the fundamental mechanisms and potential therapies preventing metastatic invasion of LN.

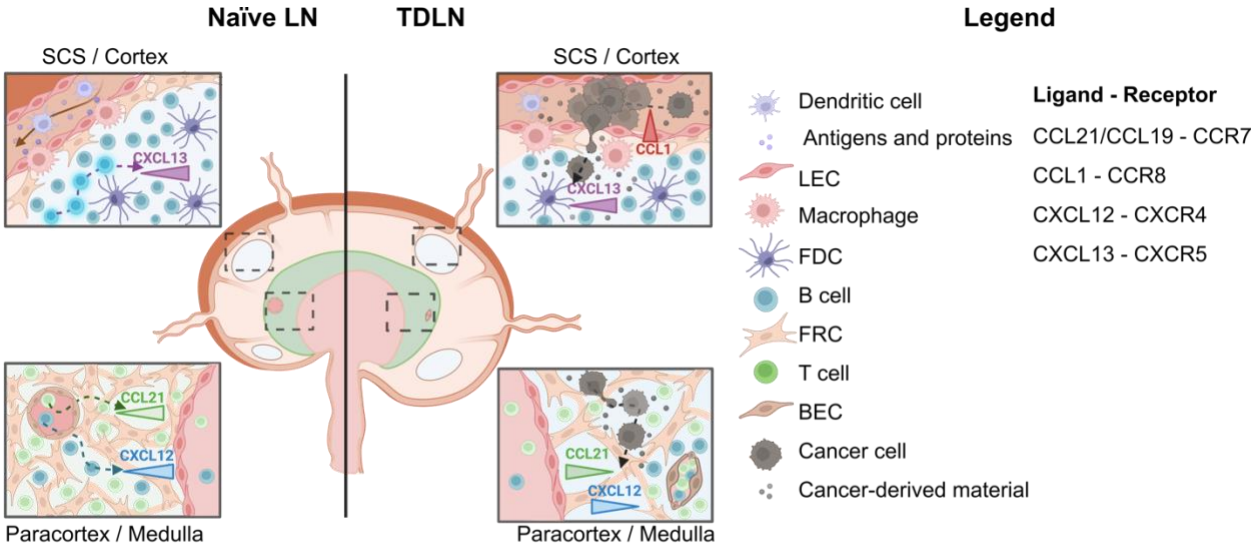

Figure 5.4: Chemokine signaling pathways designed for lymphocyte-homing to specific regions of LN implemented in migration of cancer cell. Illustration depicts the migration of immune cells to specific regions (subcapsular sinus, cortex, paracortex, medulla) of LNs in response to local chemokine gradients in the naive state. In tumor-draining lymph nodes (TDLNs), cancer cells can hijack these lymphocyte-homing signals to facilitate their invasion.

5.7 Existing models of LN metastasis are insufficient to measure factors controlling tumor cell invasion in TDLN

While it is established that invasion of the LN may promote metastatic advancement, the factors fostering a favorable milieu for tumor cell infiltration in the TDLN and the underlying mechanisms governing this process remain incompletely understood. Understanding tumor cell invasion in the TDLN involves recognizing it as a dynamic process of migration regulated by both biophysical and biochemical factors within the local microenvironment. Studying the capacity of tumor cells to invade distinct regions of the LN parenchyma is challenging using existing models, especially as a function of the state of the LN. While in vivo studies significantly improved our understanding of tumor cell metastasis in TDLN, assessing dynamic tumor cell invasion within specific LN regions is technically challenging and often requires the utilization of modern imaging techniques and/or reporter animal models.[76] Furthermore, the TDLN co-evolves with the tumor in vivo, making it difficult the parse the impacts of any changes to the cancer cells on egress from the primary tumor, entry into primary lymphatics, and invasion into the LN itself.

In contrast, in vitro 3D cell culture models of LN metastasis potentially enable precise control of the microenvironment while allowing time-course analysis. A variety of 3D culture systems have been developed to recapitulate features of LN architecture and signaling cues in the context of cancer. For example, Birmingham et al. engineered a LN sinus-on-a-chip platform mimicking microenvironment of the SCS to assess synergistically the influence of fluid flow profiles, adhesive ligand presentation, and presence of monocytic cells on cancer invasion of LNs.[77] Shim et al. demonstrated LN immunosuppression by tumor-secreted molecular factors in a microfluidic co-culture of live ex vivo LN tissues with tumor explants.[78] Tian et al. engineered

lymphoma organoid model enabling presentation of integrins specific for B and T cell lymphoma cells to demonstrate the effect of microenvironmental cues on proliferation, clustering, and drug resistance.[79] However, to date no model has captured the dynamic events of tumor cell spread in the organized LN, nor replicated the role of chemokine signaling in tumor cell invasion of the LN parenchyma.

Due to the limited capability of existing models to examine dynamic metastatic spread while controlling physical and biochemical factors, new models of tumor immunity are required to understanding the mechanisms underlying LN metastasis.

5.8 Concluding remarks

While it is well established that breast cancer often involves the lymphatic system and invades TDLN, the mechanisms underlying metastatic seeding in TDLNs remain unclear. There is strong evidence supporting the role of chemokines in facilitating cancer cell migration from the site of the tumor into the lymphatics and TDLNs, however the impact of local chemokine gradients on cancer cell survival and spread following their arrival in the SCS remains poorly understood. However, studying the capacity of cancer cells to invade distinct regions of the LN parenchyma presents a challenge due to limitations in existing models. Understanding cancer cell invasion in the TDLN involves recognizing it as an active migration process regulated by both biophysical and biochemical factors within of local microenvironment. Existing experimental models fail to simultaneously capture the sequential steps of LN metastasis and to identify the factors controlling tumor cell invasion in the complex tissue architecture. To address the limitations of existing models of LN metastasis, here we aimed to establish a new ex vivo model based on live ex vivo LN slices.

Chapter 6 will focus on the development of a novel ex vivo model of tumor cell seeding in spatially organized LN tissue with intact chemotactic function. As a demonstration, we employed this model to test the requirement for chemokine signaling in cancer invasion towards chemokine-rich domains of the naive LNs. Furthermore, we applied our novel system to model invasion into pre-metastatic TDLNs, to address an open question of whether pre-metastatic nodes were more permission or resistant to cancer cell invasion.

In **Chapter 7** we characterized the physical and biochemical remodeling of TDLN at advanced stages of the disease using in vivo model of BRPKp110 breast cancer.

Chapter 8 will discuss the impact of this research, the limitations of the novel model, and future research directions. Throughout this work, I developed and optimized several methodologies, which are comprehensively described in the **Contributed Protocols** section.

5.9 References

(1) Arnold, M.; Morgan, E.; Rumgay, H.; Mafra, A.; Singh, D.; Laversanne, M.; Vignat, J.; Gralow, J. R.; Cardoso, F.; Siesling, S.; Soerjomataram, I. Current and Future Burden of Breast Cancer: Global Statistics for 2020 and 2040. *The Breast* **2022**, *66*, 15–23. https://doi.org/10.1016/j.breast.2022.08.010.

(2) Bray, F.; Laversanne, M.; Sung, H.; Ferlay, J.; Siegel, R. L.; Soerjomataram, I.; Jemal, A. Global Cancer Statistics 2022: GLOBOCAN Estimates of Incidence and Mortality Worldwide for 36 Cancers in 185 Countries. *CA. Cancer J. Clin.* **2024**, caac.21834. https://doi.org/10.3322/caac.21834.

(3) Ran, S.; Volk, L.; Hall, K.; Flister, M. J. Lymphangiogenesis and Lymphatic Metastasis in Breast Cancer. *Pathophysiology* **2010**, *17* (4), 229–251. https://doi.org/10.1016/j.pathophys.2009.11.003.

(4) Steeg, P. S. Tumor Metastasis: Mechanistic Insights and Clinical Challenges. *Nat. Med.* **2006**, *12* (8), 895–904. https://doi.org/10.1038/nm1469.

(5) Valastyan, S.; Weinberg, R. A. Tumor Metastasis: Molecular Insights and Evolving Paradigms. *Cell* **2011**, *147* (2), 275–292. https://doi.org/10.1016/j.cell.2011.09.024.

(6) Mohammed, R. A. A.; Martin, S. G.; Gill, M. S.; Green, A. R.; Paish, E. C.; Ellis, I. O. Improved Methods of Detection of Lymphovascular Invasion Demonstrate That It Is the Predominant Method of Vascular Invasion in Breast Cancer and Has Important Clinical Consequences. *Am. J. Surg. Pathol.* **2007**, *31* (12), 1825–1833. https://doi.org/10.1097/PAS.0b013e31806841f6.

(7) Padera, T. P.; Meijer, E. F. J.; Munn, L. L. The Lymphatic System in Disease Processes and Cancer Progression. *Annu. Rev. Biomed. Eng.* **2016**, *18* (1), 125–158. https://doi.org/10.1146/annurev-bioeng-112315-031200.

(8) Liao, S.; Padera, T. P. Lymphatic Function and Immune Regulation in Health and Disease. *Lymphat. Res. Biol.* **2013**, *11* (3), 136–143. https://doi.org/10.1089/lrb.2013.0012.

(9) Brown, M.; Assen, F. P.; Leithner, A.; Abe, J.; Schachner, H.; Asfour, G.; Bago-Horvath, Z.; Stein, J. V.; Uhrin, P.; Sixt, M.; Kerjaschki, D. Lymph Node Blood Vessels Provide Exit Routes for Metastatic Tumor Cell Dissemination in Mice. *Science* **2018**, *359* (6382), 1408–1411. https://doi.org/10.1126/science.aal3662.

(10) Pereira, E. R.; Kedrin, D.; Seano, G.; Gautier, O.; Meijer, E. F. J.; Jones, D.; Chin, S.-M.; Kitahara, S.; Bouta, E. M.; Chang, J.; Beech, E.; Jeong, H.-S.; Carroll, M. C.; Taghian, A. G.;

Padera, T. P. Lymph Node Metastases Can Invade Local Blood Vessels, Exit the Node, and Colonize Distant Organs in Mice. *Science* **2018**, *359* (6382), 1403–1407. https://doi.org/10.1126/science.aal3622.

(11) du Bois, H.; Heim, T. A.; Lund, A. W. Tumor-Draining Lymph Nodes: At the Crossroads of Metastasis and Immunity. *Sci. Immunol.* **2021**, *6* (63), eabg3551. https://doi.org/10.1126/sciimmunol.abg3551.

(12) Morton, D. L.; Thompson, J. F.; Cochran, A. J.; Mozzillo, N.; Nieweg, O. E.; Roses, D. F.; Hoekstra, H. J.; Karakousis, C. P.; Puleo, C. A.; Coventry, B. J.; Kashani-Sabet, M.; Smithers, B. M.; Paul, E.; Kraybill, W. G.; McKinnon, J. G.; Wang, H.-J.; Elashoff, R.; Faries, M. B. Final Trial Report of Sentinel-Node Biopsy versus Nodal Observation in Melanoma. *N. Engl. J. Med.* **2014**, *370* (7), 599–609. https://doi.org/10.1056/NEJMoa1310460.

(13) Singletary, S. E.; Allred, C.; Ashley, P.; Bassett, L. W.; Berry, D.; Bland, K. I.; Borgen, P. I.; Clark, G.; Edge, S. B.; Hayes, D. F.; Hughes, L. L.; Hutter, R. V. P.; Morrow, M.; Page, D. L.; Recht, A.; Theriault, R. L.; Thor, A.; Weaver, D. L.; Wieand, H. S.; Greene, F. L. Revision of the American Joint Committee on Cancer Staging System for Breast Cancer. *J. Clin. Oncol.* **2002**, *20* (17), 3628–3636. https://doi.org/10.1200/JCO.2002.02.026.

(14) Woodward, W. A.; Strom, E. A.; Tucker, S. L.; McNeese, M. D.; Perkins, G. H.; Schechter, N. R.; Singletary, S. E.; Theriault, R. L.; Hortobagyi, G. N.; Hunt, K. K.; Buchholz, T. A. Changes in the 2003 American Joint Committee on Cancer Staging for Breast Cancer Dramatically Affect Stage-Specific Survival. *J. Clin. Oncol.* **2003**, *21* (17), 3244–3248. https://doi.org/10.1200/JCO.2003.03.052.

(15) Ji, H.; Hu, C.; Yang, X.; Liu, Y.; Ji, G.; Ge, S.; Wang, X.; Wang, M. Lymph Node Metastasis in Cancer Progression: Molecular Mechanisms, Clinical Significance and Therapeutic

Interventions. *Signal Transduct. Target. Ther.* **2023**, *8* (1), 367. https://doi.org/10.1038/s41392-023-01576-4.

(16) Reticker-Flynn, N. E.; Zhang, W.; Belk, J. A.; Basto, P. A.; Escalante, N. K.; Pilarowski, G. O. W.; Bejnood, A.; Martins, M. M.; Kenkel, J. A.; Linde, I. L.; Bagchi, S.; Yuan, R.; Chang, S.; Spitzer, M. H.; Carmi, Y.; Cheng, J.; Tolentino, L. L.; Choi, O.; Wu, N.; Kong, C. S.; Gentles, A. J.; Sunwoo, J. B.; Satpathy, A. T.; Plevritis, S. K.; Engleman, E. G. Lymph Node Colonization Induces Tumor-Immune Tolerance to Promote Distant Metastasis. *Cell* **2022**, *185* (11), 1924-1942.e23. https://doi.org/10.1016/j.cell.2022.04.019.

(17) Delclaux, I.; Ventre, K. S.; Jones, D.; Lund, A. W. The Tumor-Draining Lymph Node as a Reservoir for Systemic Immune Surveillance. *Trends Cancer* **2024**, *10* (1), 28–37. https://doi.org/10.1016/j.trecan.2023.09.006.

(18) Cochran, A. J.; Huang, R.-R.; Lee, J.; Itakura, E.; Leong, S. P. L.; Essner, R. Tumour–Induced Immune Modulation of Sentinel Lymph Nodes. *Nat. Rev. Immunol.* **2006**, *6* (9), 659–670. https://doi.org/10.1038/nri1919.

(19) Preynat-Seauve, O.; Contassot, E.; Schuler, P.; Piguet, V.; French, L. E.; Huard, B. Extralymphatic Tumors Prepare Draining Lymph Nodes to Invasion via a T-Cell Cross-Tolerance Process. *Cancer Res.* **2007**, *67* (10), 5009–5016. https://doi.org/10.1158/0008-5472.CAN-06-4494.

(20) Lee, E.; Pandey, N. B.; Popel, A. S. Pre-Treatment of Mice with Tumor-Conditioned Media Accelerates Metastasis to Lymph Nodes and Lungs: A New Spontaneous Breast Cancer Metastasis Model. *Clin. Exp. Metastasis* **2014**, *31* (1), 67–79. https://doi.org/10.1007/s10585-013-9610-9.

(21) Vinay, D. S.; Ryan, E. P.; Pawelec, G.; Talib, W. H.; Stagg, J.; Elkord, E.; Lichtor, T.; Decker, W. K.; Whelan, R. L.; Kumara, H. M. C. S.; Signori, E.; Honoki, K.; Georgakilas, A. G.; Amin, A.; Helferich, W. G.; Boosani, C. S.; Guha, G.; Ciriolo, M. R.; Chen, S.; Mohammed, S. I.; Azmi, A. S.; Keith, W. N.; Bilsland, A.; Bhakta, D.; Halicka, D.; Fujii, H.; Aquilano, K.; Ashraf, S. S.; Nowsheen, S.; Yang, X.; Choi, B. K.; Kwon, B. S. Immune Evasion in Cancer: Mechanistic Basis and Therapeutic Strategies. *Semin. Cancer Biol.* **2015**, *35*, S185–S198. https://doi.org/10.1016/j.semcancer.2015.03.004.

(22) Louie, D. A. P.; Oo, D.; Leung, G.; Lin, Y.; Stephens, M.; Alrashed, O.; Tso, M.; Liao, S. Tumor-Draining Lymph Node Reconstruction Promotes B Cell Activation During E0771 Mouse Breast Cancer Growth. *Front. Pharmacol.* **2022**, *13*, 825287. https://doi.org/10.3389/fphar.2022.825287.

(23) Mao, X.; Tang, X.; Pan, H.; Yu, M.; Ji, S.; Qiu, W.; Che, N.; Zhang, K.; Huang, Z.; Jiang, Y.; Wang, J.; Zhong, Z.; Wang, J.; Liu, M.; Chen, M.; Zhou, W.; Wang, S. B Cells and IL-21-Producing Follicular Helper T Cells Cooperate to Determine the Dynamic Alterations of Premetastatic Tumor Draining Lymph Nodes of Breast Cancer. *Research* **2024**, *7*, 0346. https://doi.org/10.34133/research.0346.

(24) Fransen, M. F.; Schoonderwoerd, M.; Knopf, P.; Camps, M. G. M.; Hawinkels, L. J. A. C.; Kneilling, M.; Van Hall, T.; Ossendorp, F. Tumor-Draining Lymph Nodes Are Pivotal in PD-1/PD-L1 Checkpoint Therapy. *JCI Insight* **2018**, *3* (23), e124507. https://doi.org/10.1172/jci.insight.124507.

(25) Dammeijer, F.; Van Gulijk, M.; Mulder, E. E.; Lukkes, M.; Klaase, L.; Van Den Bosch, T.; Van Nimwegen, M.; Lau, S. P.; Latupeirissa, K.; Schetters, S.; Van Kooyk, Y.; Boon, L.; Moyaart, A.; Mueller, Y. M.; Katsikis, P. D.; Eggermont, A. M.; Vroman, H.; Stadhouders,

R.; Hendriks, R. W.; Thüsen, J. V. D.; Grünhagen, D. J.; Verhoef, C.; Van Hall, T.; Aerts, J. G. The PD-1/PD-L1-Checkpoint Restrains T Cell Immunity in Tumor-Draining Lymph Nodes. *Cancer Cell* **2020**, *38* (5), 685-700.e8. https://doi.org/10.1016/j.ccell.2020.09.001.

(26) Connolly, K. A.; Kuchroo, M.; Venkat, A.; Khatun, A.; Wang, J.; William, I.; Hornick, N. I.; Fitzgerald, B. L.; Damo, M.; Kasmani, M. Y.; Cui, C.; Fagerberg, E.; Monroy, I.; Hutchins, A.; Cheung, J. F.; Foster, G. G.; Mariuzza, D. L.; Nader, M.; Zhao, H.; Cui, W.; Krishnaswamy, S.; Joshi, N. S. A Reservoir of Stem-like CD8 $^{+}$ T Cells in the Tumor-Draining Lymph Node Preserves the Ongoing Antitumor Immune Response. *Sci. Immunol.* **2021**, *6* (64), eabg7836. https://doi.org/10.1126/sciimmunol.abg7836.

(27) Iwai, T.; Sugimoto, M.; Patil, N. S.; Bower, D.; Suzuki, M.; Kato, C.; Yorozu, K.; Kurasawa, M.; Shames, D. S.; Kondoh, O. Both T Cell Priming in Lymph Node and CXCR3-Dependent Migration Are the Key Events for Predicting the Response of Atezolizumab. *Sci. Rep.* **2021**, *11* (1), 13912. https://doi.org/10.1038/s41598-021-93113-y.

(28) Molenkamp, B. G.; Sluijter, B. J. R.; Van Leeuwen, P. A. M.; Santegoets, S. J. A. M.; Meijer, S.; Wijnands, P. G. J. T. B.; Haanen, J. B. A. G.; Van Den Eertwegh, A. J. M.; Scheper, R. J.; De Gruijl, T. D. Local Administration of PF-3512676 CpG-B Instigates Tumor-Specific CD8+ T-Cell Reactivity in Melanoma Patients. *Clin. Cancer Res.* **2008**, *14* (14), 4532–4542. https://doi.org/10.1158/1078-0432.CCR-07-4711.

(29) Sluijter, B. J. R.; Van Den Hout, M. F. C. M.; Koster, B. D.; Van Leeuwen, P. A. M.; Schneiders, F. L.; Van De Ven, R.; Molenkamp, B. G.; Vosslamber, S.; Verweij, C. L.; Van Den Tol, M. P.; Van Den Eertwegh, A. J. M.; Scheper, R. J.; De Gruijl, T. D. Arming the Melanoma Sentinel Lymph Node through Local Administration of CpG-B and GM-CSF: Recruitment and Activation of BDCA3/CD141+ Dendritic Cells and Enhanced Cross-

Presentation. *Cancer Immunol. Res.* **2015**, *3* (5), 495–505. https://doi.org/10.1158/2326-6066.CIR-14-0165.

(30) O'Melia, M. J.; Manspeaker, M. P.; Thomas, S. N. Tumor-Draining Lymph Nodes Are Survival Niches That Support T Cell Priming against Lymphatic Transported Tumor Antigen and Effects of Immune Checkpoint Blockade in TNBC. *Cancer Immunol. Immunother.* **2021**, *70* (8), 2179–2195. https://doi.org/10.1007/s00262-020-02792-5.

(31) Li, M.; Zhang, Y.; Zhang, Q.; Li, J. Tumor Extracellular Matrix Modulating Strategies for Enhanced Antitumor Therapy of Nanomedicines. *Mater. Today Bio* **2022**, *16*, 100364. https://doi.org/10.1016/j.mtbio.2022.100364.

(32) Sixt, M.; Kanazawa, N.; Selg, M.; Samson, T.; Roos, G.; Reinhardt, D. P.; Pabst, R.; Lutz, M. B.; Sorokin, L. The Conduit System Transports Soluble Antigens from the Afferent Lymph to Resident Dendritic Cells in the T Cell Area of the Lymph Node. *Immunity* **2005**, *22* (1), 19–29. https://doi.org/10.1016/j.immuni.2004.11.013.

(33) Bajénoff, M.; Germain, R. N. B-Cell Follicle Development Remodels the Conduit System and Allows Soluble Antigen Delivery to Follicular Dendritic Cells. *Blood* **2009**, *114* (24), 4989–4997. https://doi.org/10.1182/blood-2009-06-229567.

(34) Katakai, T.; Hara, T.; Sugai, M.; Gonda, H.; Shimizu, A. Lymph Node Fibroblastic Reticular Cells Construct the Stromal Reticulum via Contact with Lymphocytes. *J. Exp. Med.* **2004**, *200* (6), 783–795. https://doi.org/10.1084/jem.20040254.

(35) Li, L.; Wu, J.; Abdi, R.; Jewell, C. M.; Bromberg, J. S. Lymph Node Fibroblastic Reticular Cells Steer Immune Responses. *Trends Immunol.* **2021**, *42* (8), 723–734. https://doi.org/10.1016/j.it.2021.06.006.

(36) Lukacs-Kornek, V.; Malhotra, D.; Fletcher, A. L.; Acton, S. E.; Elpek, K. G.; Tayalia, P.; Collier, A.; Turley, S. J. Regulated Release of Nitric Oxide by Nonhematopoietic Stroma Controls Expansion of the Activated T Cell Pool in Lymph Nodes. *Nat. Immunol.* **2011**, *12* (11), 1096–1104. https://doi.org/10.1038/ni.2112.

(37) Krishnamurty, A. T.; Turley, S. J. Lymph Node Stromal Cells: Cartographers of the Immune System. *Nat. Immunol.* **2020**, *21* (4), 369–380. https://doi.org/10.1038/s41590-020-0635-3.

(38) Link, A.; Vogt, T. K.; Favre, S.; Britschgi, M. R.; Acha-Orbea, H.; Hinz, B.; Cyster, J. G.; Luther, S. A. Fibroblastic Reticular Cells in Lymph Nodes Regulate the Homeostasis of Naive T Cells. *Nat. Immunol.* **2007**, *8* (11), 1255–1265. https://doi.org/10.1038/ni1513.

(39) Cinti, I.; Denton, A. E. Lymphoid Stromal Cells—More than Just a Highway to Humoral Immunity. *Oxf. Open Immunol.* **2021**, *2* (1), iqab011. https://doi.org/10.1093/oxfimm/iqab011.

(40) Miller, M.; Mayo, K. Chemokines from a Structural Perspective. *Int. J. Mol. Sci.* **2017**, *18* (10), 2088. https://doi.org/10.3390/ijms18102088.

(41) Kufareva, I.; Salanga, C. L.; Handel, T. M. Chemokine and Chemokine Receptor Structure and Interactions: Implications for Therapeutic Strategies. *Immunol. Cell Biol.* **2015**, *93* (4), 372–383. https://doi.org/10.1038/icb.2015.15.

(42) Shields, J. D.; Emmett, M. S.; Dunn, D. B. A.; Joory, K. D.; Sage, L. M.; Rigby, H.; Mortimer, P. S.; Orlando, A.; Levick, J. R.; Bates, D. O. Chemokine-Mediated Migration of Melanoma Cells towards Lymphatics – a Mechanism Contributing to Metastasis. *Oncogene* **2007**, *26* (21), 2997–3005. https://doi.org/10.1038/sj.onc.1210114.

(43) Wiley, H. E.; Gonzalez, E. B.; Maki, W.; Wu, M. -t.; Hwang, S. T. Expression of CC Chemokine Receptor-7 and Regional Lymph Node Metastasis of B16 Murine Melanoma.

JNCI J. Natl. Cancer Inst. **2001**, *93* (21), 1638–1643. https://doi.org/10.1093/jnci/93.21.1638.

(44) Li, X.; Sun, S.; Li, N.; Gao, J.; Yu, J.; Zhao, J.; Li, M.; Zhao, Z. High Expression of CCR7 Predicts Lymph Node Metastasis and Good Prognosis in Triple Negative Breast Cancer. *Cell. Physiol. Biochem.* **2017**, *43* (2), 531–539. https://doi.org/10.1159/000480526.

(45) Sperveslage, J.; Frank, S.; Heneweer, C.; Egberts, J.; Schniewind, B.; Buchholz, M.; Bergmann, F.; Giese, N.; Munding, J.; Hahn, S. A.; Kalthoff, H.; Klöppel, G.; Sipos, B. Lack of CCR7 Expression Is Rate Limiting for Lymphatic Spread of Pancreatic Ductal Adenocarcinoma. *Int. J. Cancer* **2012**, *131* (4). https://doi.org/10.1002/ijc.26502.

(46) Das, S.; Sarrou, E.; Podgrabinska, S.; Cassella, M.; Mungamuri, S. K.; Feirt, N.; Gordon, R.; Nagi, C. S.; Wang, Y.; Entenberg, D.; Condeelis, J.; Skobe, M. Tumor Cell Entry into the Lymph Node Is Controlled by CCL1 Chemokine Expressed by Lymph Node Lymphatic Sinuses. *J. Exp. Med.* **2013**, *210* (8), 1509–1528. https://doi.org/10.1084/jem.20111627.

(47) Müller, A.; Homey, B.; Soto, H.; Ge, N.; Catron, D.; Buchanan, M. E.; McClanahan, T.; Murphy, E.; Yuan, W.; Wagner, S. N.; Barrera, J. L.; Mohar, A.; Verástegui, E.; Zlotnik, A. Involvement of Chemokine Receptors in Breast Cancer Metastasis. *Nature* **2001**, *410* (6824), 50–56. https://doi.org/10.1038/35065016.

(48) Kato, M.; Kitayama, J.; Kazama, S.; Nagawa, H. Expression Pattern of CXC Chemokine Receptor-4 Is Correlated with Lymph Node Metastasis in Human Invasive Ductal Carcinoma. *Breast Cancer Res.* **2003**, *5* (5), R144. https://doi.org/10.1186/bcr627.

(49) Kang, H.; Watkins, G.; Parr, C.; Douglas-Jones, A.; Mansel, R. E.; Jiang, W. G. Stromal Cell Derived Factor-1: Its Influence on Invasiveness and Migration of Breast Cancer Cells in

Vitro, and Its Association with Prognosis and Survival in Human Breast Cancer. *Breast Cancer Res.* **2005**, *7* (4), R402. https://doi.org/10.1186/bcr1022.

(50) Hiller, D.; Chu, Q. D. CXCR4 and Axillary Lymph Nodes: Review of a Potential Biomarker for Breast Cancer Metastasis. *Int. J. Breast Cancer* **2011**, *2011*, 1–6. https://doi.org/10.4061/2011/420981.

(51) Sun, Y.; Mao, X.; Fan, C.; Liu, C.; Guo, A.; Guan, S.; Jin, Q.; Li, B.; Yao, F.; Jin, F. CXCL12-CXCR4 Axis Promotes the Natural Selection of Breast Cancer Cell Metastasis. *Tumor Biol.* **2014**, *35* (8), 7765–7773. https://doi.org/10.1007/s13277-014-1816-1.

(52) Biswas, S.; Sengupta, S.; Roy Chowdhury, S.; Jana, S.; Mandal, G.; Mandal, P. K.; Saha, N.; Malhotra, V.; Gupta, A.; Kuprash, D. V.; Bhattacharyya, A. CXCL13–CXCR5 Co-Expression Regulates Epithelial to Mesenchymal Transition of Breast Cancer Cells during Lymph Node Metastasis. *Breast Cancer Res. Treat.* **2014**, *143* (2), 265–276. https://doi.org/10.1007/s10549-013-2811-8.

(53) Ebisuno, Y.; Tanaka, T.; Kanemitsu, N.; Kanda, H.; Yamaguchi, K.; Kaisho, T.; Akira, S.; Miyasaka, M. Cutting Edge: The B Cell Chemokine CXC Chemokine Ligand 13/B Lymphocyte Chemoattractant Is Expressed in the High Endothelial Venules of Lymph Nodes and Peyer's Patches and Affects B Cell Trafficking Across High Endothelial Venules. *J. Immunol.* **2003**, *171* (4), 1642–1646. https://doi.org/10.4049/jimmunol.171.4.1642.

(54) Bowman, E. P.; Campbell, J. J.; Soler, D.; Dong, Z.; Manlongat, N.; Picarella, D.; Hardy, R. R.; Butcher, E. C. Developmental Switches in Chemokine Response Profiles during B Cell Differentiation and Maturation. *J. Exp. Med.* **2000**, *191* (8), 1303–1318. https://doi.org/10.1084/jem.191.8.1303.

(55) Pikor, N. B.; Mörbe, U.; Lütge, M.; Gil-Cruz, C.; Perez-Shibayama, C.; Novkovic, M.; Cheng, H.-W.; Nombela-Arrieta, C.; Nagasawa, T.; Linterman, M. A.; Onder, L.; Ludewig, B. Remodeling of Light and Dark Zone Follicular Dendritic Cells Governs Germinal Center Responses. *Nat. Immunol.* **2020**, *21* (6), 649–659. https://doi.org/10.1038/s41590-020-0672-y.

(56) Allen, C. D. C.; Ansel, K. M.; Low, C.; Lesley, R.; Tamamura, H.; Fujii, N.; Cyster, J. G. Germinal Center Dark and Light Zone Organization Is Mediated by CXCR4 and CXCR5. *Nat. Immunol.* **2004**, *5* (9), 943–952. https://doi.org/10.1038/ni1100.

(57) Luther, S. A.; Bidgol, A.; Hargreaves, D. C.; Schmidt, A.; Xu, Y.; Paniyadi, J.; Matloubian, M.; Cyster, J. G. Differing Activities of Homeostatic Chemokines CCL19, CCL21, and CXCL12 in Lymphocyte and Dendritic Cell Recruitment and Lymphoid Neogenesis. *J. Immunol.* **2002**, *169* (1), 424–433. https://doi.org/10.4049/jimmunol.169.1.424.

(58) Kim, M.; Koh, Y. J.; Kim, K. E.; Koh, B. I.; Nam, D.-H.; Alitalo, K.; Kim, I.; Koh, G. Y. CXCR4 Signaling Regulates Metastasis of Chemoresistant Melanoma Cells by a Lymphatic Metastatic Niche. *Cancer Res.* **2010**, *70* (24), 10411–10421. https://doi.org/10.1158/0008-5472.CAN-10-2591.

(59) Kuehnemuth, B.; Piseddu, I.; Wiedemann, G. M.; Lauseker, M.; Kuhn, C.; Hofmann, S.; Schmoeckel, E.; Endres, S.; Mayr, D.; Jeschke, U.; Anz, D. CCL1 Is a Major Regulatory T Cell Attracting Factor in Human Breast Cancer. *BMC Cancer* **2018**, *18* (1), 1278. https://doi.org/10.1186/s12885-018-5117-8.

(60) Hoelzinger, D. B.; Smith, S. E.; Mirza, N.; Dominguez, A. L.; Manrique, S. Z.; Lustgarten, J. Blockade of CCL1 Inhibits T Regulatory Cell Suppressive Function Enhancing Tumor

Immunity without Affecting T Effector Responses. *J. Immunol.* **2010**, *184* (12), 6833–6842. https://doi.org/10.4049/jimmunol.0904084.

(61) Issa, A.; Le, T. X.; Shoushtari, A. N.; Shields, J. D.; Swartz, M. A. Vascular Endothelial Growth Factor-C and C-C Chemokine Receptor 7 in Tumor Cell–Lymphatic Cross-Talk Promote Invasive Phenotype. *Cancer Res.* **2009**, *69* (1), 349–357. https://doi.org/10.1158/0008-5472.CAN-08-1875.

(62) Qian, C.-N.; Berghuis, B.; Tsarfaty, G.; Bruch, M.; Kort, E. J.; Ditlev, J.; Tsarfaty, I.; Hudson, E.; Jackson, D. G.; Petillo, D.; Chen, J.; Resau, J. H.; Teh, B. T. Preparing the "Soil": The Primary Tumor Induces Vasculature Reorganization in the Sentinel Lymph Node before the Arrival of Metastatic Cancer Cells. *Cancer Res.* **2006**, *66* (21), 10365–10376. https://doi.org/10.1158/0008-5472.CAN-06-2977.

(63) Harrell, M. I.; Iritani, B. M.; Ruddell, A. Tumor-Induced Sentinel Lymph Node Lymphangiogenesis and Increased Lymph Flow Precede Melanoma Metastasis. *Am. J. Pathol.* **2007**, *170* (2), 774–786. https://doi.org/10.2353/ajpath.2007.060761.

(64) Chung, M. K.; Do, I.-G.; Jung, E.; Son, Y.-I.; Jeong, H.-S.; Baek, C.-H. Lymphatic Vessels and High Endothelial Venules Are Increased in the Sentinel Lymph Nodes of Patients with Oral Squamous Cell Carcinoma Before the Arrival of Tumor Cells. *Ann. Surg. Oncol.* **2012**, *19* (5), 1595–1601. https://doi.org/10.1245/s10434-011-2154-9.

(65) Bekkhus, T.; Martikainen, T.; Olofsson, A.; Franzén Boger, M.; Vasiliu Bacovia, D.; Wärnberg, F.; Ulvmar, M. H. Remodeling of the Lymph Node High Endothelial Venules Reflects Tumor Invasiveness in Breast Cancer and Is Associated with Dysregulation of Perivascular Stromal Cells. *Cancers* **2021**, *13* (2), 211. https://doi.org/10.3390/cancers13020211.

(66) Riedel, A.; Shorthouse, D.; Haas, L.; Hall, B. A.; Shields, J. Tumor-Induced Stromal Reprogramming Drives Lymph Node Transformation. *Nat. Immunol.* **2016**, *17* (9), 1118–1127. https://doi.org/10.1038/ni.3492.

(67) Martinez, V. G.; Pankova, V.; Krasny, L.; Singh, T.; Makris, S.; White, I. J.; Benjamin, A. C.; Dertschnig, S.; Horsnell, H. L.; Kriston-Vizi, J.; Burden, J. J.; Huang, P. H.; Tape, C. J.; Acton, S. E. Fibroblastic Reticular Cells Control Conduit Matrix Deposition during Lymph Node Expansion. *Cell Rep.* **2019**, *29* (9), 2810-2822.e5. https://doi.org/10.1016/j.celrep.2019.10.103.

(68) Rohner, N. A.; McClain, J.; Tuell, S. L.; Warner, A.; Smith, B.; Yun, Y.; Mohan, A.; Sushnitha, M.; Thomas, S. N. Lymph Node Biophysical Remodeling Is Associated with Melanoma Lymphatic Drainage. *FASEB J. Off. Publ. Fed. Am. Soc. Exp. Biol.* **2015**, *29* (11), 4512–4522. https://doi.org/10.1096/fj.15-274761.

(69) Jones, D.; Wang, Z.; Chen, I. X.; Zhang, S.; Banerji, R.; Lei, P.-J.; Zhou, H.; Xiao, V.; Kwong, C.; Van Wijnbergen, J. W. M.; Pereira, E. R.; Vakoc, B. J.; Huang, P.; Nia, H. T.; Padera, T. P. Solid Stress Impairs Lymphocyte Infiltration into Lymph-Node Metastases. *Nat. Biomed. Eng.* **2021**, *5* (12), 1426–1436. https://doi.org/10.1038/s41551-021-00766-1.

(70) Fischer, K.; Hoffmann, P.; Voelkl, S.; Meidenbauer, N.; Ammer, J.; Edinger, M.; Gottfried, E.; Schwarz, S.; Rothe, G.; Hoves, S.; Renner, K.; Timischl, B.; Mackensen, A.; Kunz-Schughart, L.; Andreesen, R.; Krause, S. W.; Kreutz, M. Inhibitory Effect of Tumor Cell–Derived Lactic Acid on Human T Cells. *Blood* **2007**, *109* (9), 3812–3819. https://doi.org/10.1182/blood-2006-07-035972.

(71) Mullen, A. R.; DeBerardinis, R. J. Genetically-Defined Metabolic Reprogramming in Cancer. *Trends Endocrinol. Metab.* **2012**, *23* (11), 552–559. https://doi.org/10.1016/j.tem.2012.06.009.

(72) Hood, J. L.; San, R. S.; Wickline, S. A. Exosomes Released by Melanoma Cells Prepare Sentinel Lymph Nodes for Tumor Metastasis. *Cancer Res.* **2011**, *71* (11), 3792–3801. https://doi.org/10.1158/0008-5472.CAN-10-4455.

(73) Nogués, L.; Benito-Martin, A.; Hergueta-Redondo, M.; Peinado, H. The Influence of Tumour-Derived Extracellular Vesicles on Local and Distal Metastatic Dissemination. *Mol. Aspects Med.* **2018**, *60*, 15–26. https://doi.org/10.1016/j.mam.2017.11.012.

(74) Torcellan, T.; Hampton, H. R.; Bailey, J.; Tomura, M.; Brink, R.; Chtanova, T. In Vivo Photolabeling of Tumor-Infiltrating Cells Reveals Highly Regulated Egress of T-Cell Subsets from Tumors. *Proc. Natl. Acad. Sci. U. S. A.* **2017**, *114* (22), 5677–5682. https://doi.org/10.1073/pnas.1618446114.

(75) Salmon, H.; Idoyaga, J.; Rahman, A.; Leboeuf, M.; Remark, R.; Jordan, S.; Casanova-Acebes, M.; Khudoynazarova, M.; Agudo, J.; Tung, N.; Chakarov, S.; Rivera, C.; Hogstad, B.; Bosenberg, M.; Hashimoto, D.; Gnjatic, S.; Bhardwaj, N.; Palucka, A. K.; Brown, B. D.; Brody, J.; Ginhoux, F.; Merad, M. Expansion and Activation of CD103(+) Dendritic Cell Progenitors at the Tumor Site Enhances Tumor Responses to Therapeutic PD-L1 and BRAF Inhibition. *Immunity* **2016**, *44* (4), 924–938. https://doi.org/10.1016/j.immuni.2016.03.012.

(76) Greenlee, J. D.; King, M. R. Engineered Fluidic Systems to Understand Lymphatic Cancer Metastasis. *Biomicrofluidics* **2020**, *14* (1), 011502. https://doi.org/10.1063/1.5133970.

(77) Birmingham, K. G.; O'Melia, M. J.; Bordy, S.; Reyes Aguilar, D.; El-Reyas, B.; Lesinski, G.; Thomas, S. N. Lymph Node Subcapsular Sinus Microenvironment-On-A-Chip Modeling

Shear Flow Relevant to Lymphatic Metastasis and Immune Cell Homing. *iScience* **2020**, *23* (11), 101751. https://doi.org/10.1016/j.isci.2020.101751.

(78) Shim, S.; Belanger, M. C.; Harris, A. R.; Munson, J. M.; Pompano, R. R. Two-Way Communication between *Ex Vivo* Tissues on a Microfluidic Chip: Application to Tumor–Lymph Node Interaction. *Lab. Chip* **2019**, *19* (6), 1013–1026. https://doi.org/10.1039/C8LC00957K.

(79) Tian, Y. F.; Ahn, H.; Schneider, R. S.; Yang, S. N.; Roman-Gonzalez, L.; Melnick, A. M.; Cerchietti, L.; Singh, A. Integrin-Specific Hydrogels as Adaptable Tumor Organoids for Malignant B and T Cells. *Biomaterials* **2015**, *73*, 110–119. https://doi.org/10.1016/j.biomaterials.2015.09.007.

6 Ex vivo model of breast cancer cell invasion in live lymph node tissue

6.1 Introduction

Breast cancer is one of the most common primary cancers worldwide, annually diagnosed in > 270,000 patients.[1] In breast cancer, metastatic disease remains the underlying cause of mortality,[2] and it occurs preferentially through the lymphatics, with 8-fold higher invasion of lymphatics than blood vessels.[3] The sentinel lymph node (LN), located downstream from the primary cancer, is the first organ contacted by cancer cells passing through the lymphatic vessels and may provide a niche for metastatic seeding.[4] Indeed, 27% of breast cancer patients have detectable LN metastasis at diagnosis.[5] The presence of LN metastasis is linked to poorer survival outcomes compared to patients without nodal involvement,[6] potentially due to induction of immune tolerance[7] and/or subsequent dissemination to distant organs.[8–10] However, despite its potential importance to patient outcomes, the factors fostering a favorable milieu for cancer cell infiltration of the LN and the underlying mechanisms governing this process remain incompletely understood.

Cancer cells that reach the TDLN encounter a highly organized lymphoid structure in the midst of change. Designed for survey of immunological material carried LN is compartmentalized into four major anatomical regions: subcapsular sinus (SCS), cortex, the paracortex, and the medulla. Before metastatic seeding occurs, TDLNs undergo extensive structural and functional remodeling.[11] Structurally, lymphangiogenesis and enlargement of high endothelial venules,[12] dilation of the SCS,[13] and a relaxation of the underlying stromal network collectively affect size

exclusion[14] and fluid permissiveness[15] of lymphatic conduits. Furthermore, the secretion of chemokines in TDLNs dynamically changes in response to the upstream tumor.[11] However, little is known about how all of these changes cumulatively impact the receptivity of the TDLN to cancer cell invasion. Some evidence suggests that the tumor primes its TDLN to be more receptive to metastasis than non-draining LN,[16–18] while other evidence indicates that tumor-induced remodeling of TDLN facilitates immune priming and elimination of cancer at early stages.[19–21]

Locations of invasion and survival in the LN are likely influenced by local microenvironmental cues such as chemokines and cellular activity. Cancer cells often enter the TDLN through the SCS and then penetrate deeper into the cortex via the lymphatic barrier at the sinus floor.[13] There is strong evidence that chemokines facilitate cancer cell migration from the tumor site into the lymphatics and TDLN, with cancer cells often exploiting the same homing mechanisms used by leukocytes to reach specific regions of LN.[4] However, many questions remain, including which regions of the LN preferentially support invasion, to what extent cancer cells invade chemokine-rich domains and whether blockade of chemokine signaling could modulate LN metastasis, and even whether the pre-metastatic TDLN is primed to be more or less receptive to invasion.

Questions such as these are challenging to answer using existing models, especially when accounting for the dynamic state of the LN. Most studies are performed in vivo in animal models, and these systems significantly improved our understanding of cancer cell metastasis in TDLN. However, the TDLN co-evolves with the tumor in vivo, making it difficult to study how invasion behavior may depend on the state of the LN separately from how it depends on the tumor microenvironment. In vivo, it is hard to discern how drugs or gene modifications made to the cancer cells may separately impact egress from the primary tumor, entry into primary lymphatics,

and invasion into the LN itself. Furthermore, assessing the dynamics of cancer cell invasion within specific LN regions over time is technically challenging, due to the terminal nature of most imaging approaches, limited numbers of reporter animal models, and the complexity of advanced in vivo imaging.[22] For these reasons, a variety of 3D cell culture systems have been developed to recapitulate features of LN architecture and signaling cues in the context of cancer metastasis. These systems have mimicked the microenvironment or fluid dynamics of specific anatomical regions of TDLNs;[23] recreated molecular communication between immune and tumor compartments;[24] and allowed for the testing of the effects of microenvironmental cues and immunotherapies on tumor cell survival.[25–27] While these systems potentially enable precise control of the microenvironment and allow time-course analysis, to date no model has captured the dynamic events of cancer cell invasion and spread in the spatially organized LN, nor replicated the role of chemokine signaling in cancer cell invasion of the LN parenchyma.

More than three decades ago, Brodt pioneered the use of frozen murine LN sections and demonstrated a correlation between cancer cell attachment to the 2-dimensional LN sections in vitro and their potential for lymphatic metastasis in vivo.[28] Recent work has shown that live LN explants support 3D cell migration and spread through organized tissue and maintain chemotactic function.[29–31] However, although T cell motility is commonly studied in LN slices,[29,32] cancer cell invasion has not been tested.

Here we aimed to establish a new ex vivo model on LN metastasis based on live ex vivo LN slices (Figure 6.1). We tested the hypothesis that the chemotactic activity in live LN slices could could recruit cancer cells into the LN parenchyma, including predicting aspects of the dynamic distribution of tumor cells previously reported in vivo. We tested the extent to which invasion was chemotactic towards particular chemokines, and demonstrated how the model could

be used to test requirements for chemokine signaling in cancer invasion. Finally, we applied this system to model invasion into pre-metastatic TDLNs, to begin to address an open question of whether pre-metastatic nodes are more permissive or resistant to invasion.

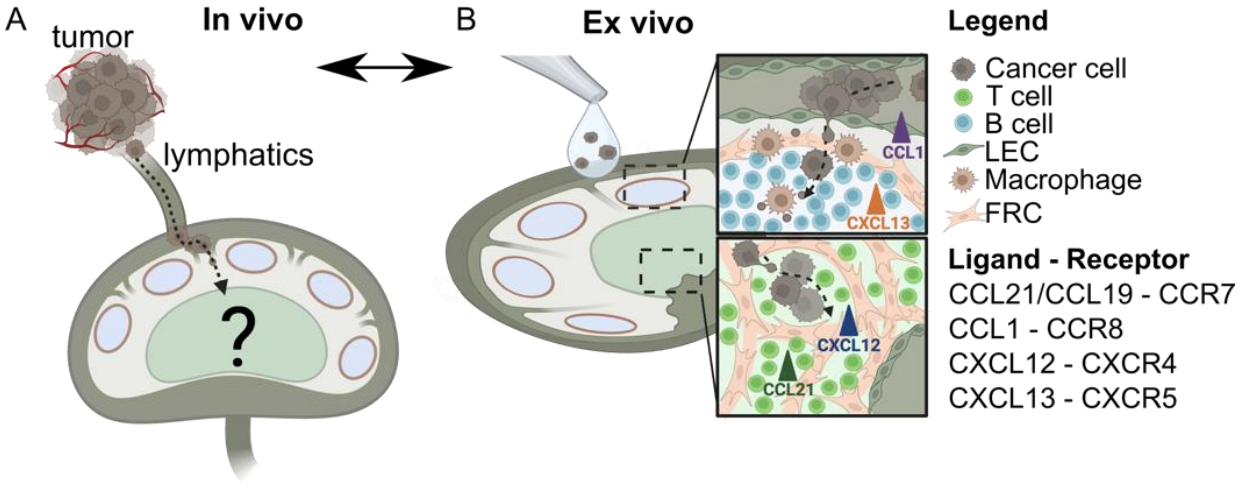

Figure 6.1: Conceptual illustration of an ex vivo model using live LN tissue slices to model cancer cell chemotaxis in TDLNs. (A) In vivo, cancer cells from the primary tumor invade the lymphatic system and eventually the TDLN, where mechanisms of invasion are difficult to parse. (B) An ex vivo model of chemotactic invasion of cancer cells within the organized LN architecture. Insets show spread of cancer cells in distinct anatomical regions of the LN. List of chemokine ligand – receptor signaling axes implemented in promoting cancer cell chemotactic migration. Figure created with BioRender.com.

6.2 Methods

6.2.1 Cell culture

Mouse mammary cancer cell lines BRPKp110-GFP+, 4T1-luc-red and melanoma B16F10 were obtained from Melanie Rutkowski, University of Virginia. Cells were cultured in RMPI (Gibco, 2505339) supplemented with 10% FBS (Corning Heat-inactivated, USDA approved origin, lot: 301210001), 1x L-glutamine (Gibco Life Technologies, lot: 2472354), 50 U/mL Pen/Strep (Gibco, lot: 2441845), 50 µM beta-mercaptoethanol (Gibco, 21985-023), 1 mM sodium pyruvate (Hyclone, 2492879), 1× non-essential amino acids (GIBCO, 2028868), and 20 mM HEPES (Gibco, 15630-060). Cells were seeded in T75 or T175 flasks (Nunc™ EasYFlask™, Fisher Scientific) following manufactures recommendations and cultured sterilely in humidified atmosphere of 5% CO2 and 95% oxygen at 37°C. All cell lines were maintained for less than four passages, with monitoring of morphology and testing for mycoplasma.

6.2.2 Animal work

All animal work was approved by the Institutional Animal Care and Use Committee at the University of Virginia under protocol no. 4042 and was conducted in compliance with guidelines the Office of Laboratory Animal Welfare at the National Institutes of Health (United States). C57BL/6 mice ages 6–12 weeks (Jackson Laboratory, U.S.A.) were housed in a vivarium and given water and food ad libitum. Due to the prevalence of the breast cancer in women, only female mice were used in this study. For generation of tumors in vivo, $5 \cdot 10^5$ BRPKp110 cells were suspended in 100 µL PBS and injected orthotopically into the abdominal mammary fat pad. A control group of female C57Bl/6 mice of matched age received an injection of PBS. Tumor size was measured by calipers every 2–3 days after reaching a palpable size.

6.2.3 Generation of lymph node tissue slices

Lymph nodes were collected and sliced according to a previously established protocol.[33] Briefly, on the day of the experiment, animals were anesthetized with isoflurane followed by cervical dislocation. Inguinal and axillary lymph nodes were collected and placed in ice-cold PBS supplemented with 2% heat inactivated FBS. Subsequently, the lymph nodes were embedded in 6% low melting point agarose at 50°C and allowed to solidify. Agarose blocks containing the lymph nodes were obtained using a 10 mm tissue punch. Slices with a thickness of 300 μm were obtained using a Leica VT1000S vibratome. Following sectioning, the slices were promptly transferred to complete RPMI medium and incubated for a minimum of 1 hour before use.

6.2.4 ELISA for analysis of cytokines and chemokines

Lymph node slices were cultured in complete RPMI media for 20 hr. Culture supernatant was collected and analyzed by sandwich ELISA assay using DuoSet ELISA development kit (R&D Systems, Inc., Minneapolis, MN, USA). ELISAs were for CCL21 (catalog no. DY457), CCL19 (DY440), CCL1 (DY845), CXCL12 (DY460) and CXCL13 (DY470) according to the manufacturer's protocol. For measurement of intranodal IL-21 levels, inguinal and axillary lymph nodes were collected and carefully disrupted in 150 μL of ice-cold phosphate buffer, minimizing cell rupture.[34] The suspension was centrifuged at 1,500 rpm for 5 min, and the supernatant was collected. Samples were analyzed by sandwich ELISA assay using DuoSet ELISA development kit for Il-21 (catalog no. DY594; R&D Systems, Inc., Minneapolis, MN, USA). In all cases, plates were developed using TMB substrate (Fisher Scientific), stopped with 1 M sulfuric acid (Fisher Scientific), and absorbance values were read at 450 nm on a plate reader (CLARIOstar; BMG LabTech, Cary, NC). To determine concentration of sample solutions, calibration curves were fit

in GraphPad Prism 9 with a sigmoidal 4 parameter curve. Limit of detection (LOD) was calculated from the average of the blank + 3× standard deviation of the blank.

6.2.5 In vitro 3D transwell migration assay

$1 \cdot 10^5$ BRPKp110 cells were resuspended in a 100 µL hydrogel containing 2.0 mg/ml collagen type I (rat tail, Ibidi) and 1 mg/ml fibrinogen (BD Biosciences), then seeded into 12 mm diameter culture inserts with 8 µm pores (Millipore, Bellerica, MA). After gelation, 700 µL of chemoattractant or control media was added to the bottom compartment. To level the media outside of the insert with the medium inside and avoid generating fluid flow, 100 µL of media was added on top of the gel. Cells were allowed to migrate during incubation in a humidified atmosphere of 5% CO2 and 95% oxygen at 37°C for 20 hr. After incubation, the gels in the upper chamber were removed with a cotton-tip applicator. After incubation, the gels in the upper chamber were removed with a cotton-tip applicator. The tissue culture inserts were fixed with 4% paraformaldehyde for 20 minutes at room temperature, washed with ice-cold PBS, stained with 300 nM DAPI for 30 minutes at room temperature, washed again with ice-cold PBS, and visualized by fluorescence microscopy. DAPI+ cells at the membrane surface were counted in three non-overlapping fields per well. Three technical replicates were averaged for each experimental run to yield a single biological replicate for statistical analysis. Cancer cell migration fold was calculated as previously described.[35]

6.2.6 Ex vivo overlay of tumor cells onto live lymph node slices

After collection, lymph node slices were left to rest for at least one hour. $1 \cdot 10^6$ BRPKp110 cancer cells were first stained with NHS-Rhodamine (Fisher Scientific) or Cell Trace (Fisher Scientific) for 20 minutes in a humidified sterile incubator at 37 °C with 5% CO2. Following the incubation

period, excess fluorescent dye was removed by centrifugation. The cells were then resuspended in 1mL of complete culture media and incubated at 37 °C with 5% CO2 for 10 minutes to allow fluorescent reagent to undergo acetate hydrolysis. Lymph node slices were placed onto parafilm and covered with an A2 stainless steel flat washer (10 mm outer diameter, 5.3 mm inner; Grainger, USA), creating a 1 mm deep well over each lymph node tissue sample. For an overlay, a 20 µL of cancer cell suspension ($2 \cdot 10^4$ cells) was added into a washer on top of each LN slices and incubated for an hour at 37 °C with 5% CO2. Following the incubation period, excess cancer cells was rinsed with pre-warmed complete media for 30 minutes at 37 °C, changing the media every 10 minutes.

6.2.7 Immunostaining of live lymph node slices

Upon collection, the slices were allowed to rest for one hour before being labelled for live immunofluorescence following a previously established protocol.[36] Briefly, slices were Fc-blocked with an anti-mouse CD16/32 antibody (BioLegend, San Diego, CA) at a concentration of 25 µg/mL in 1x PBS with 2% heat-inactivated FBS (Gibco, Fisher Scientific) and incubated for 30 minutes in a humidified sterile incubator at 37 °C with 5% CO2. To stain, a 10 µL of antibody cocktail, containing antibodies at a concentration of 20 µg/mL, was added and the slices were incubated for an additional hour. Antibodies are listed in Table S1. Following staining, slices were washed with PBS for 30 minutes at 37 °C, refreshing the PBS every 10-15 minutes.

6.2.8 Cas9/RNP nucleofection

6.2.8.1 crRNA selection

Three crRNAs were selected per target using the Benchling (www.benchling.com) online platform. The target area was limited to the first ~40% of the coding sequence, and preference was given to

guides targeting different regions within this area. On-target and off-target scores were evaluated using IDT and Synthego. Guides with the highest on-target and off-target scores were selected. crRNAs were ordered from Integrated DNA Technologies (www.idtdna.com/CRISPR-Cas9) in their proprietary Alt-R format (Table S2).

6.2.8.2 Preparation of crRNA–tracrRNA duplex

To prepare the duplex, each Alt-R crRNA and Alt-R tracrRNA (catalog no. 1072534; IDT) or Alt-tracrRNA-ATTO550 (catalog no. 1075928; IDTd) was reconstituted to 100 µM with Nuclease-Free Duplex Buffer (IDT). Oligos were mixed at equimolar concentrations in a sterile PCR tube (e.g., 10 µl Alt-R crRNA and 10 µl Alt-R tracrRNA). Oligos were annealed by heating at 95°C for 5 minutes in PCR thermocycler and the mix was slowly cooled to room temperature.

6.2.8.3 Precomplexing of Cas9/RNP

In a PCR strip, three crRNA–tracrRNA duplexes (3 µl equal to 150 pmol each, total of 9 µl) and 6 µl (180 pmol) TrueCut Cas9 Protein v2 (catalog no. A36499; Thermo Fisher Scientific) were gently mix by pipetting up and down and incubated at room temperature for at least 10 minutes.

6.2.8.4 Nucleofection

$3 \cdot 10^6$ BRPKp110 cells were resuspended in 20 µl primary cell nucleofection solution (P4 Primary Cell 4D-Nucleofector X kit S (32 RCT, V4XP-4032; Lonza). Cells were mixed and incubated with 15 µl RNP at room temperature for 2 minutes. The cell/RNP mix was transferred to Nucleofection cuvette strips (4D-Nucleofector X kit S; Lonza). Cells were electroporated using a 4D nucleofector (4D-Nucleofector Core Unit: Lonza, AAF-1002B; 4D-Nucleofector X Unit: AAF-1002X; Lonza). Pulses for different T cell populations (DS137). After nucleofection, transected cells were resuspended in prewarmed complete RPMI media and cultured overnight.

Next day, tracrRNA+ cells were sorted on the BD Influx™ cell sorter using BD FACS™ Sortware software. After sorting cells were cultured for 3-5 days.

6.2.9 Flow cytometry

Tumor-draining and control lymph nodes were homogenized using glass slides. Cancer cell dissemination in TDLNs was quantified using flow cytometry acquisition on a Guava Instrument (Guava easyCyte™ 8, Merck Millipore, Billerica, MA, USA). Cell suspensions were first stained with viability dye 7-AAD (AAT Bioquest, Sunnyvale, CA, USA), followed by blocking Fc receptors with anti-CD16/32 (93, purified), and surface staining with anti-mouse CD45 (30-F11, PE). Cells were then permeabilized using buffer set (Invitrogen) and stained intracellularly with anti-GFP (FM264G, APC).

6.2.10 Image acquisition

Transwell membranes were imaged on an Axiovert 200 MOT inverted microscope with an LSM510 scan head (Zeiss, Germany). Images were collected with 5×/1.20 WD objective.

All imaging of LN tissues slices was performed on a Nikon A1Rsi confocal upright microscope, using 400, 487, 561, and 638 lasers with 450/50, 525/50, 600/50, and 685/70 GaAsp detectors. Images were collected with a 4x/ 0.20 and a 40x/ 0.45 NA Plan Apo NIR WD objective.

6.2.11 Image analysis

Images were analyzed in ImageJ (version 2.14.0/1.54g).[37] First, autofluorescent noise from the individual image channels was subtracted, defined as the mean fluorescent intensity ± 1 SD of respective fluorescent minus one (FMO) controls (n = 3 FMO control per experiment). After noise subtraction, regions of interest (ROI) were selected using the wand tracing tool and/or manually

adjusted to reflect anatomical regions. The SCS ROI was defined as the area between podoplanin-positive LECs lining the ceiling and lyve1-positive LECs lining the floor of the SCS. The B-cell ROI was identified as the B220 or CD19 positive area; the B cell follicle ROI was identified as B220 or CD19 positive circular area within the cortex regions. The medullary ROI was defined as a lyve1 positive area in the paracortex of the LN. The T cell ROI was identified as the area of the LN excluding the SCS, cortex, B cell follicles, and medulla ROIs. All regions were non-overlapping, except for B cell follicle ROIs overlapping with the cortex region. Chemokine-rich domains were identified as CCL1, CCL21, CXCL12 or CXCL13 positive ROI. Cancer cell fluorescent signals were converted to binary, and the cancer cell positive area within the total LN and each LN region was measured. Cancer cell invasion was quantified as the cancer cell positive area of the total LN area. Invasion of the individual ROI was normalized to the relative area of each ROI to define an invasion-fold change, where a higher value indicated a greater cancer positive area per unit area of the ROI, and a value of 1 indicated a fractional cancer-positive area equal to the mean in the total LN area. For representative image display, brightness and contrast were adjusted uniformly across all compared images unless otherwise specified.

6.2.12 Statistical analysis

All in vitro assays were performed with a minimum of three biological replicates unless otherwise noted. Murine study numbers are noted in legends and by individual graphed data points. Graphs were generated using Graphpad Prism (version 9.4.0) software and are shown with mean +/- standard deviation, $p < 0.05$ was considered statistically significant.

6.3 Results

6.3.1 BRPKp110 breast cancer cells were chemoattracted to chemokines secreted by live naïve LN tissue slices

Approximately 75% of breast carcinomas fall into the category of hormone receptor-positive (HR+) due to the expression of estrogen receptor and/or progesterone receptor.[38] Therefore, for this study, we selected a HR+ murine mammary cancer cell line, BRPKp110. BRPKp110 was established by culture of primary mammary carcinomas after p53 ablation and the transgenic expression of an oncogenic form of K-ras, which is commonly found in human breast cancers.[31] Similar to human breast cancer carcinomas, in vivo inoculation of BRPKp110 into immune competent mice leads to lymphovascular invasion into TDLNs, making it a good choice to model LN metastasis.[39]

As a first step towards establishing an ex vivo model, we assessed the ability of breast cancer cells to migrate towards conditioned media (CM) from LN slice cultures in vitro. In a 3D transwell assay (Figure 6.2A), CM from overnight culture of naïve murine LN tissue slices promoted a significant increase in BRPKp110 migration in comparison to control media (Figures 6.2B, C). This effect was abolished in tumor cells pretreated with Pertussis toxin (PTx), suggesting migration was mediated via chemokine signaling. To rule out potential off-target effects, we verified that PTx treatment did not alter BRPKp110 actin morphology nor affect proliferation rate (Figure S6.8).

While signaling through the CCL1/CCR8 axis has been shown to control cancer cell entry into the TDLNs,[13] other lymphocyte homing chemokines have been demonstrated to promote lymphatic invasion of cancer cells. For example, signaling through the CCL21/CCR7 axis was

shown to promote migration of metastatic melanoma cells towards lymphatics in vitro and in vivo.[41,42] Furthermore, clinical research reported correlations between CCL21, CCL19/CCR7, CXCL12/CXCR4 and CXCL13/CXCR5 signaling axes and extensive lymphatic spread, an increased risk of LN metastasis in breast cancer[43–49] and pancreatic ductal adenocarcinoma.[50,51] To identify the chemotactic stimuli secreted by live naïve LN slices, we measured the levels of a panel of chemokines in the CM, focusing especially on those that have been implicated in chemotaxis of cancer cells: CCL21, CCL19, CCL1, CXCL12 and CXCL13. In overnight culture, live LN tissue slices secreted detectable levels of each of these except CCL1, which was below the level of detection (Figure 6.2D). Media supplemented with individual recombinant chemokines resulted in an increase in cancer cell migration, but to a lesser extent than towards CM (Figure 6.2E), suggesting that some synergy may occur towards the mixture of chemokines present in the CM. Because chemokine signaling requires receptor expression on the tumor cells, we next tested chemokine receptor expression on BRPKp110 cells. Immunofluorescence labeling indicated that BRPKp110 cells expressed all four of the cognate surface receptors: CCR7, CCR8, CXCR4 and CXCR5 (Figure 6.2F). Interestingly, CXCR4 receptor expression was notably increased in cells cultured in LN CM than in control media or media supplemented with CXCL12 (Figure 6.2G). BRPKp110 cells responded to the CM and to individual chemokines with cytoskeletal rearrangements (F-actin staining) and altered cell morphology from elongated to round (Figure S6.9), further confirming their responsiveness to these ligands.

Collectively, these data demonstrated that BRPKp110 cells were chemoattracted to chemokines secreted by LN tissue and expressed functional receptors for the relevant chemokines, suggesting the potential for chemotactic migration into LN tissue.

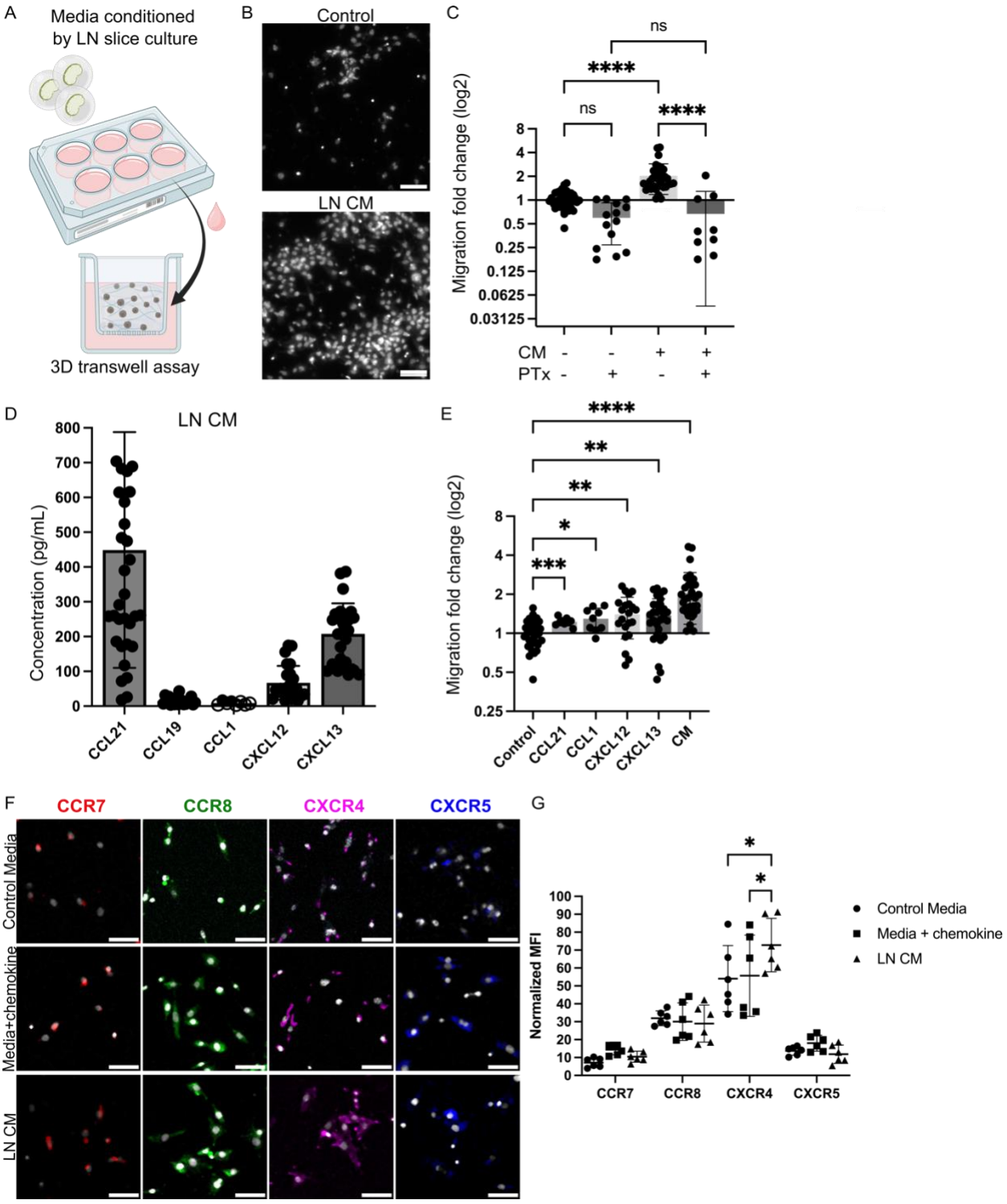

Figure 6.2: Naïve LN CM promotes chemotactic migration of BRPKp110 breast cancer cells. (A) Experimental schematic of 3D transwell migration assay. Cancer cells in hydrogel are added to the the upper compartment of a transwell membrane and migrate overnight towards control or conditioned media in the lower compartment. (B) Representative images of the invasion of

BRPKp110 cells through the transwell membrane towards control media and media conditioned by LN slice culture. Scale bar 100 µm. (C) Migration data from transwell experiments towards conditioned media versus control media. Mean ± standard deviation; each data point represents a migration fold change per membrane (n=3-5/group; normalized data pulled from 3 independent experiments). Migration fold change among tested groups was compared using a two-way ANOVA, followed by Sidak posthoc test. ****$p < 0.0001$. (D) Concentrations of CCL21, CCL19, CCL1, CXCL12 and CXCL13 were measured in live LN slice CM following a 20 hr culture period. Mean ± standard deviation; each dot shows the supernatant from one LN slice. n = 15-35 slices, pooled from 5 female mice. An unfilled circle indicates measurement below the limit of detection. (E) BRPKp110 exhibited a significant increase in migration when exposed to media containing CCL21, CCL1, CXCL12, and CXCL13 chemokines at a concentration of 100 ng/mL. Mean ± standard deviation; each data point represents migration fold change per membrane (n=3-5/group; normalized data pooled from 3 independent in vitro experiments). Migration fold change among tested groups was compared to control group using a one-way ANOVA, followed by Dunnett posthoc test. *$p < 0.05$, **$p < 0.01$, ***$p = 0.001$, ****$p < 0.0001$. (F) Representative images of surface immunofluorescence of chemokine receptors on BRPKp110 breast cancer cells after culture in control media, media supplied with the respective chemokine at 200 ng/mL, or LN CM. Scale bar 100 µm. (G) Quantification of receptor expression under various culture conditions. MFI of chemokine receptors across the image was normalized to cell count. Mean ± standard deviation; each data point represents average MFI of 1experiment (i.e. biological replicate); data pooled from 3 independent in vitro experiments. MFI in different groups was compared using a two-way ANOVA, followed by Tukey posthoc test. *$p < 0.05$.

6.3.2 Cancer cells infiltrated and proliferated in live ex vivo LN slices

To move from culture inserts to invasion into structured tissue, we tested the extent to which ex vivo LN slices could support tumor cell seeding, invasion, and spread. We developed a procedure in which a suspension of fluorescently labelled, syngeneic BRPKp110 cells was seeded on top of 300-µm thick live LN slices from naïve C57BL/6J female mice, incubated for 1 hr, and washed to remove excess cells (Figure 6.3A). We refer to this procedure as an "overlay" of cancer cells onto the tissue slices. After the overlay, the tissues were labelled via live immunofluorescence to identify LN zones.[30] In preliminary work, we determined an optimal seeding density of 20,000 cancer cells per LN slice by seeding various densities onto LN slices (data not shown).

We assessed invasion, spread, and proliferation in the tissue after overlay. BRPKp110 invaded the LN tissue in the first hour such that they were not washed away during the wash step, but were still rounded in morphology. By 20 hr, the cell morphology had changed to elongated, characteristic of cell adhesion and spread (Figure 6.3B), and they had penetrated to an average depth of 140 ± 17 μm into the LN tissue (Figure 6.3C). The tumor cells continued proliferating in the tissue, as staining for Ki-67 revealed a similar proportion of proliferating BRPKp110 cells after 20 hr in the LN tissue as in culture of BRPKp110 cells alone (Figures 6.3D, E). To test the generalizability of this approach, we examined two additional cancer cell lines: HR+ B16F10 murine melanoma and HR- 4T1 murine mammary carcinoma cells. Both cell lines demonstrated the ability to infiltrate LN tissue, showing invasion after 1 hour and further spreading after 20 hours of culture (Figure S6.10). Thus, live LN slices could support an ex vivo model of tumor cell invasion and spread across multiple cancer cell lines.

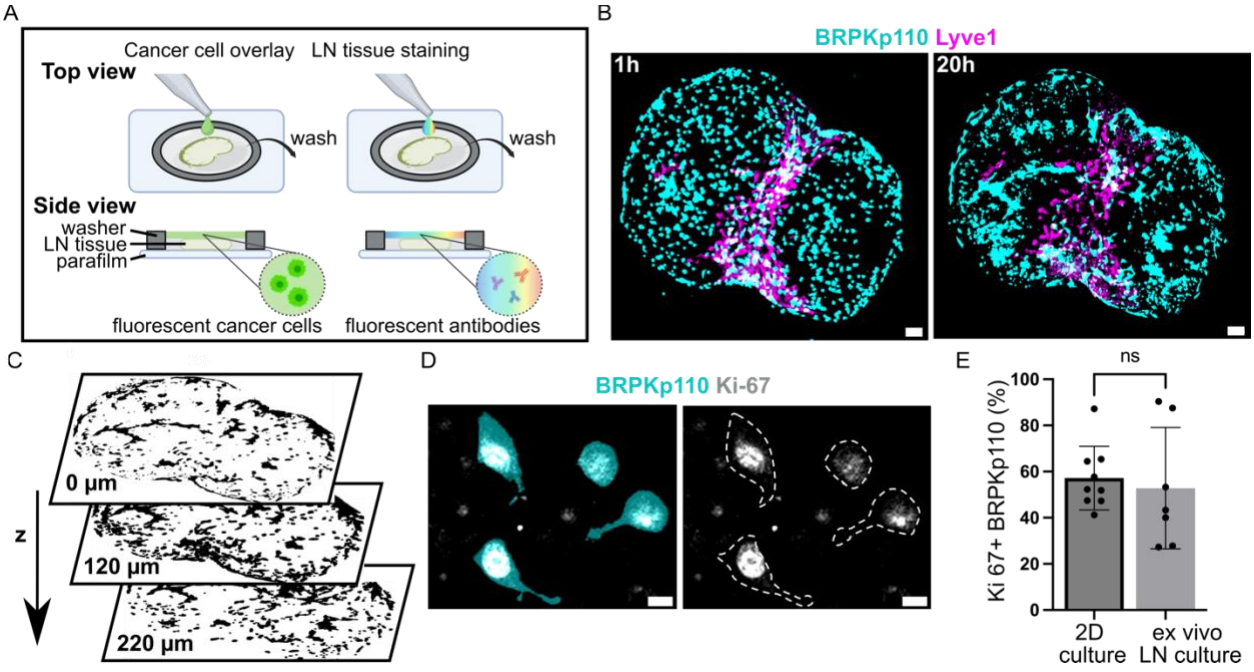

Figure 6.3: Cancer cells introduced to live LN slices ex vivo infiltrate, proliferate and exhibit a dynamic spreading over a 20h culture period. . (A) Schematic representation of cancer cell seeding onto live 300-μm sections of LN tissue, followed by live immunostaining via fluorescently

conjugated antibodies. (B) Fluorescent BRPKp110 cells (NHS-Rhodamine, cyan) were seeded ex vivo onto naïve LN slices stained for lymphatic endothelial cells (lyve1, magenta) and imaged at 1 hr and 20 hr after seeding. Scale bar 200 µm. (C) Binary image of cancer cells at multiple z-depths illustrating infiltration into the LN tissue. (D) Representative image of proliferating BRPKp110 cells (NHS-Rhodamine, cyan) positive for Ki-67 (gray) 20 hr after seeding onto LN tissue. The left image shows merged channels for BRPKp110 and Ki-67; the right image displays Ki-67 with cell contours outlined by a dotted line. Scale bar 20 µm. (E) Percent of Ki-67 positive cells per field of view in BRPKp110 cultured for 20h alone or seeded ex vivo onto live LN. Mean ± standard deviation; each data point represent measurement from an individual sample (n=2-3/group, data pulled from 3 independent experiments). Fraction of Ki-67 positive cells between culture conditions was compared using unpaired t-test. $p > 0.05$.

6.3.3 Enrichment of cancer cells in the SCS preceded spread to the cortex and B cell follicle zones

Similar to direct intra-LN injection performed in vivo,[7,21] adding cancer cells directly to the face of a LN slice allows the cells to bypass the afferent lymphatic vasculature. We took advantage of this feature to determine which regions of the LN were preferentially colonized by cancer cells in the absence of access barriers. To do so, we compared invasion between LN regions, using live tissue immunostaining and image segmentation to define the SCS, cortex, B cell follicles, T cell zone and medulla (Figure 6.4A). Invasion was normalized to the relative area of each zone to define an invasion-fold change, where a higher value indicated a greater cancer positive area per unit area of the region, and a value of 1 indicated a fractional cancer-positive area equal to the mean in the entire tissue slice.

We assessed the distribution of the tumor cells at 1, 20, and 40 hr after seeding, hypothesizing that there would be reorganization over time. At 1 hr after seeding, there was a notably greater distribution of BRPKp110 cells within the SCS and significantly lower in T cell zone in comparison to the average across the tissue (Figure 6.4B). Indeed, individual cancer cells

were clearly visible inside the SCS (Figure 6.4C), as well as elsewhere in the tissue. However, by 20 hr after seeding, the enrichment of BRPKp110 cells within the SCS was no longer statistically significant; instead, cancer cells were preferentially distributed within the cortex and B cell follicles. No difference was detected in the regional distribution of cancer cells between the 20-hr and 40-hr culture periods (Figure S6.11). Thus, cancer cells initially entered the tissue preferentially in the SCS, followed by a re-distribution into the cortex and B cell zones, with relative exclusion from the central T cell zones at both times. This behavior was reminiscent of the in vivo behavior of melanoma tumor cells in TDLN, where metastatic cells first accumulated in the SCS in response to a CCL1 gradient and later formed metastatic lesions in the deeper parenchyma.[13]

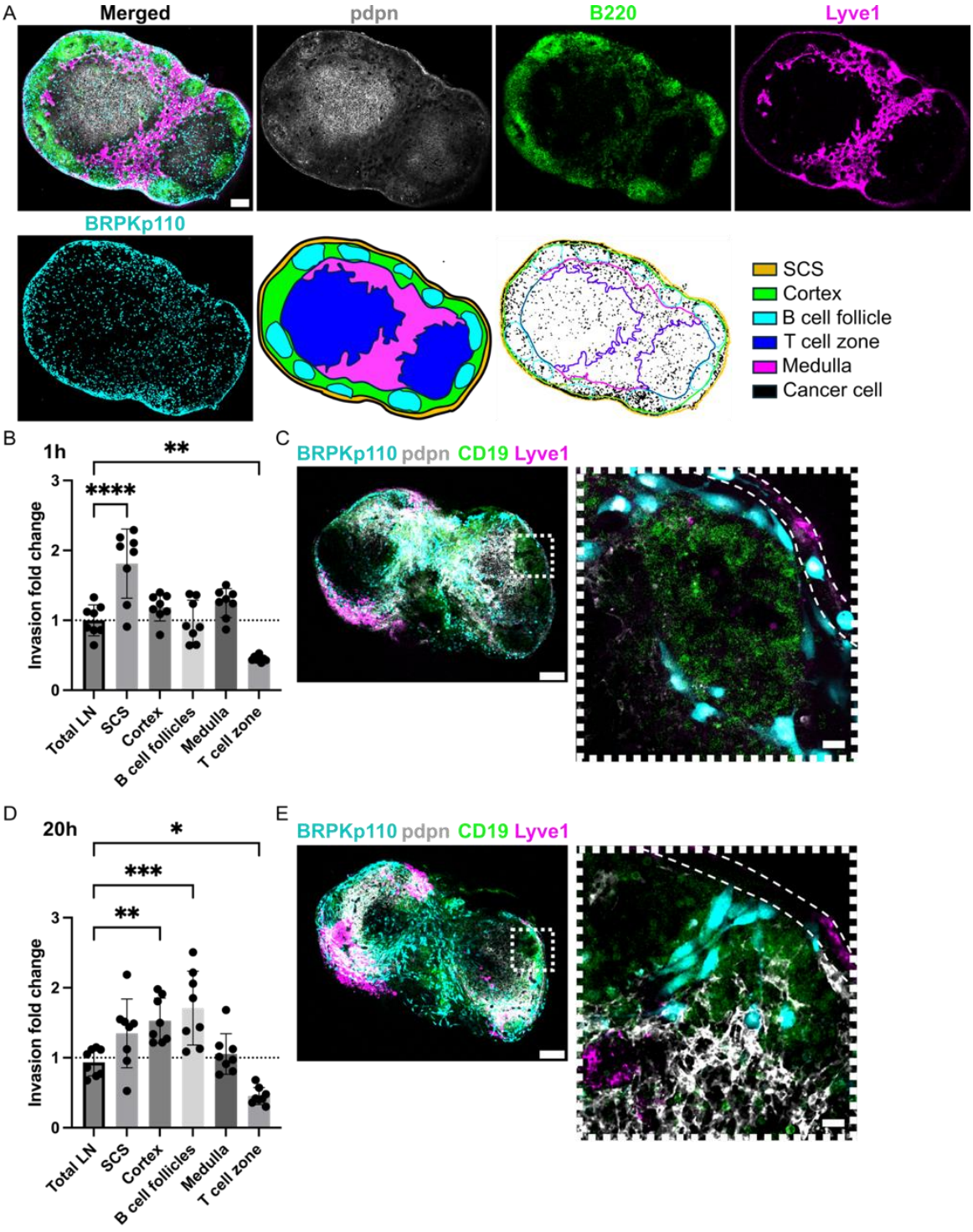

Figure 6.4: Dynamic distribution of cancer cells across LN zones. (A) Quantification of cancer cell invasion in LN zones via live immunostaining and image segmentation. Representative image of LN tissue slice overlaid with cancer cells (NHS-Rhodamine, cyan) and stained for podoplanin (pdpn, gray), a B cell marker (B220, green), and lymphatic endothelial cells (lyve1, magenta). Schematic for assignment of LN regions to the SCS, cortex, B cell follicles, medulla and T cell

zone. Cancer cell invasion is measured as BRPKp110+ area of the LN zone and normalized to the average invasion to the total area. (B) BRPKp110 invasion fold change across LN zones compared to the invasion of the total LN area following 1 hr post-seeding. Mean ± standard deviation; dotted line represents normalized enrichment across the total area of the LN slice; each data point represents invasion fold change normalized to the total LN invasion on a per slice basis (n = 7-8/per group, LN slices obtained from 3 mice). (C) Representative images of BRPKp110 cells (cyan) invasion in the SCS at 1h post-seeding. Scale bars: left image 200 µm; right image 20 µm (D) BRPKp110 invasion fold change across LN zones compared to the invasion of the total LN area following 20 hr post-seeding. Mean ± standard deviation; dotted line represents normalized enrichment across the total area of the LN slice; each data point represents invasion fold change normalized to the total LN invasion on a per slice basis; n = 7-8/per group, LN slices obtained from 3 mice. (E) Representative images of BRPKp110 invading cortex and B cell follicles regions at 20 hr post-seeding. LN tissues were stained with a B cell marker (CD19, green) and lymphatic cell marker (Lyve-1, magenta). Scale bars: left image 200 µm; right image 20 µm. Invasion fold change in LN zones was compared to invasion fold change in total LN using a one-way ANOVA, followed by Dunnett posthoc test. *p <0.05, **p < 0.01, ***p = 0.001, ****p < 0.0001.

6.3.4 Ex vivo invasion correlated with the distribution of CXCL13 and CCL1 in naïve LN slices

Chemokines establish both soluble and immobilized concentration gradients. To define which zones of naïve LNs expressed immobilized CCL21, CCL1, CXCL12 and CXCL13 and how these changed during LN slice culture, we used live immunofluorescence labeling (Figure 6.5A) and image segmentation method as in Figure 2A. The distribution of immobilized CCL21 and CXCL13 in LN culture exhibited dynamic changes over time (Figure 6.5B). Specifically, there was a significant decrease in the total LN area positive for CCL21+ (76% decrease, $p < 0.001$), accompanied by a concurrent increase in the total LN area positive for CXCL13 (83% increase, $p < 0.01$). No changes in the fractions of the total LN area positive for CCL1+ and CXCL12+ were detected in culture from 1 hr to 20 hr (Figure 6.5B). None of the chemokines were confined to a

specific anatomical zone of LN, but rather were distributed across all anatomical zones of the LN to varying degrees (Figure S6.12).

As the chemokines were distributed throughout the LN, we next asked the extent to which BRPKp110 cancer cell invasion in this ex vivo model correlated with distribution of immobilized chemokines. Cancer cell invasion within chemokine-positive and chemokine-negative regions was compared to the average invasion across the LN slice. To avoid neutralizing any chemokine activity, immunofluorescence labeling was performed after cancer cell invasion in these experiments. At 1hr post-seeding, BRPKp110 invasion was 1.6-fold higher in the CXCL13+ region compared to the tissue average (Figure S6.13); no enrichment was detected in other chemokine-positive or negative regions (Figure S6.14). After 20 hr of culture, invasion rate remained high in the CXCL13+ region (1.5-fold increase over the average) and was also increased in the CCL1+ region (1.3-fold increase over the average) (Figures 6.5C, D, E, F). No enrichment was detected in other chemokine-positive or negative regions at this time (Figure S6.15). Thus, we established a correlation between spatiotemporal invasion of cancer cell in naïve LN tissue and distribution of immobilized CXCL13 and CCL1. Considering that the chemokines were detected across multiple zones of the LN, we concluded that cancer cell distribution was better predicted by the distribution of chemokine-rich domains than by anatomical zone.

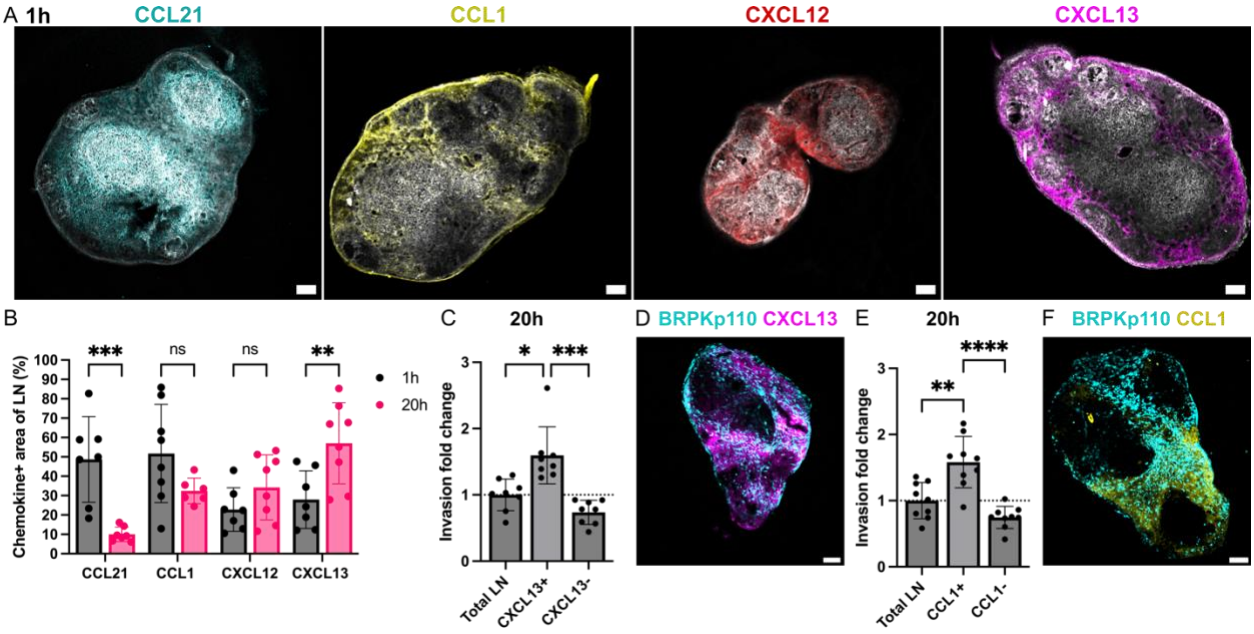

Figure 6.5: Spatiotemporal invasion of cancer cells in regions of immobilized chemokines. (A) Representative images of LN staining of immobilized distribution of CCL21, CCL1, CXCL12 and CXCL13 chemokines after 1 hr of culture. (B) Fraction of LN area positive for immobilized chemokines after 1 hr and 20 hr of culture. Mean ± standard deviation; each data point represents measurement from one LN slice (n = 7-8/per group, LN slices obtained from 3 mice). Chemokine+ area was compared using a two-way ANOVA, followed by Sidak's posthoc test. *p < 0.05, ***p < 0.001. (C) BRPKp110 invasion fold in CXCL13 positive (CXCL13+) and CXCL13 negative (CXCL13-) regions of LN relative to the invasion to the total LN tissue after 20 hr of culture. Mean ± standard deviation; dotted line represents normalized enrichment across the total area of the LN slice; each data point represents invasion fold change normalized to the total LN invasion on a per slice basis (n = 7/per group, LN slices obtained from 3 mice). Invasion fold change was compared using a one-way ANOVA, followed by Tukey posthoc test. *p < 0.05, ***p < 0.001. (D) Representative images of BRPKp110 in CXCL13+ region after 20 hr of culture. (E) BRPKp110 invasion fold in CCL1 positive (CCL1+) and CCL1 negative (CCL1-) domains of LN relative to the invasion to the total LN tissue after 20 hr of culture. Mean ± standard deviation; dotted line represents normalized enrichment across the total area of the LN slice; each data point represents invasion fold change normalized to the total LN invasion on a per slice basis (n = 8/per group, LN slices obtained from 3 mice). Invasion fold change was compared using a one-way ANOVA, followed by Tukey posthoc test *p < 0.05, ***p < 0.001. Scale bars 200 µm.

6.3.5 Knock-out of CXCR5 in BRPKp110 impaired migration into the lymph node and revealed redundancy in chemotactic migration

A feature of the ex vivo model is that it isolates the impact of changes in cancer cell signaling on invasion of the lymph node, without confounding effects from changes to migration out of the primary tumor or entry or migration through the lymphatic vasculature. Having found preferential BRPKp110 invasion towards CXCL13 at both 1 hr and 20 hr after overlay, we sought to demonstrate this capability by testing the requirement for the cognate chemokine receptor, CXCR5, in facilitating localization in the LN. We utilized CRISPR (clustered, regularly interspaced, short palindromic repeats)/Cas9 (CRISPR-associated protein 9) technology to generate BRPKp110 cell lines lacking function of CXCR5. To facilitate interaction with Cas9, we employed chemically modified synthetic CXCR5 gene–specific CRISPR RNAs (crRNA) along with fluorescently labeled tracer RNAs (tracrRNAs), enabling the selection of transfected population through cell sorting (Figure 6.6A). Post-transfection, the viable fraction of tracrRNA-positive BRPKp110 cells, which constituted 85.5% of all cells, was isolated and cultured to establish the BRPKp110 CXCR5 knockout (KO) cell line (Figure 6.6B). We confirmed the loss of chemotactic function in CXCR5 KO cells using a 3D transwell assay with media supplemented with CXCL13 (Figure 6.6C). A similar effort to generate CCR7 KO cells resulted in an 78.6% of viable, tracrRNA-positive cells (Figures S6.16). However, while CCR8 KO cells were also produced, they retained chemotactic function towards CCL1 and were not pursued further.

First, we tested requirement for CXCR5 in cancer cell migration towards factors secreted by naïve LN in vitro. Using conditioned media obtained from overnight culture of naïve LN slices, we compared the migration of CXCR5 KO versus wild type (WT) BRPKp110 controls in a 3D transwell assay. The mean change in migration towards LN CM was 26% reduced in CXCR5 KO

as compared to WT BRPKp110 (Figure 6.6D). On the other hand, there was substantial within-group variation between supernatants from different slices, leaving the migration towards CM not significantly different between WT and KO cells. This result suggested that targeting the CXCR5 receptor reduced the migration of cancer cells toward factors secreted by naïve LN, but perhaps did not completely eliminate it.

Next, we tested the requirement of CXCR5 for cancer cell invasion into naïve LN tissue, and into the CXCL13+ domain in particular. To allow paired comparisons of invasion, we overlayed equal numbers of CXCR5 KO and WT BRPKp110 cells, labeled with different fluorophores, onto each LN slice. In line with the in vitro results, we found that CXCR5 KO cells invaded less into each slice than the WT cells (27% mean reduction in invasion; Figure 6.6E), though some cells did still enter the tissue. Interestingly, although total invasion was reduced, invasion of the CXCL13+ domain was unaffected by KO of CXCR5 alone (Figure 6.6F). Only complete blockade of chemokine signaling by PTx treatment significantly reduced the BRPKp110 invasion in the CXCL13+ regions (Figures 6.6G, H), an effect that remained after 20 hr of culture. Thus, we concluded that the migration of CXCR5 KO cells towards CXCL13+ regions was driven by chemotaxis towards other chemokines.

These findings collectively suggested that CXCR5 was required for a portion of the total BRPKp110 invasion into naïve LNs, but that disrupting CXCR5-mediated signaling alone was insufficient to prevent invasion towards domains rich in CXCL13, due to the multiple chemokines expressed in any given region. These experiments were enabled by the isolation of the LN in the ex vivo model and would be challenging to conduct in vivo, since CXCL13/CXCR5 axis also plays a substantial role within the tumor itself.[52,53]

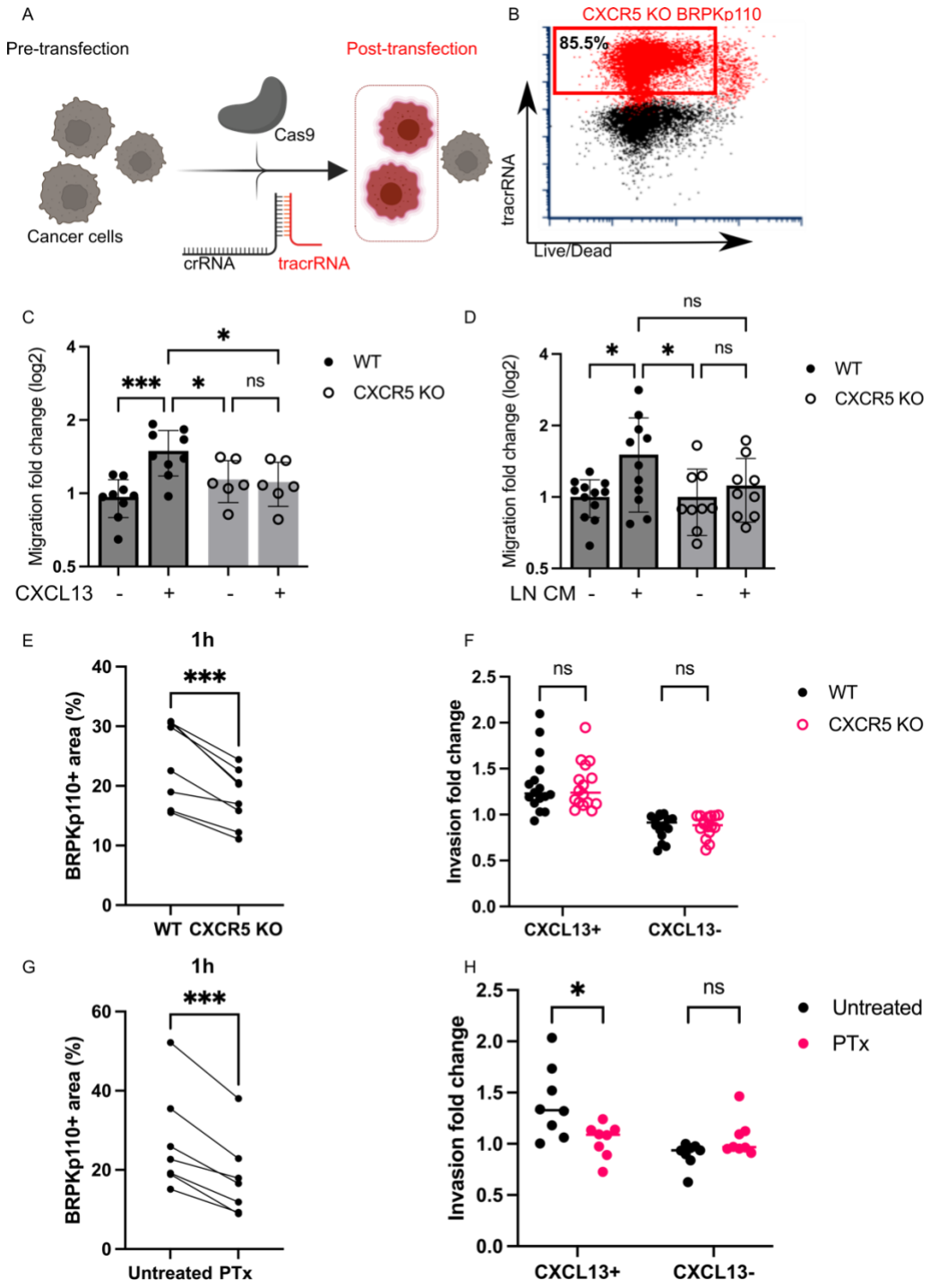

Figure 6.6: Blockade of CXCR5 mediated signaling alone was not sufficient to prevent cancer cell chemotactic migration into LN tissue. (A) Application of CRISPR/Cas9 technology for generation of cancer cell lines lacking CXCR5. crRNA, fluorescently labeled tracrRNA, and recombinant Cas9 protein. (B) Selection of tracrRNA positive cell population post-transfection (red), non-transfected control WT BRPKp110 (black). (C) CXCR5 KO migration toward media containing 200 ng/mL of CXCL13 was impaired, confirming the loss of receptor function. Each data point

represents the mean migration fold change per membrane, calculated from three non-overlapping fields of view (n = 2-3 membranes/condition; normalized data pooled from 3 independent in vitro experiments). Migration fold change was compared using a two-way ANOVA, followed by Tukey posthoc test. ***p < 0.0001, *p < 0.05. (D) Migration fold change of WT and CXCR5 KO BRPKp110 cells towards media conditioned by culture of naïve LN CM from culture. Each data point represents the mean migration fold change per membrane, calculated from three non-overlapping fields of view (n = 3-4 membranes/condition; normalized data pooled from 3 independent in vitro experiments). Migration fold change was compared using a two-way ANOVA, followed by Tukey posthoc test. *p < 0.05. (E) Fraction of total LN area positive for WT BRPKp110 and CXCR5 KO BRPKp110 after 1 hr post overlay. Each data point represents paired measurements from one LN slice (n = 7/per group, LN slices obtained from 3 mice). Cancer cell positive area was compared via paired t-test. ***p < 0.001. (F) Invasion fold change of WT BRPKp110 and CXCR5 KO BRPKp110 in CXCL13+ domain after 1 hr post overlay. Each data point represents invasion fold per LN slice (n = 15 slices, LN slices obtained from 3 mice). Invasion fold change was compared using a two-way ANOVA, followed by Sidak posthoc test. p> 0.5. (G) Fraction of total LN area positive for untreated WT BRPKp110 and PTx pre-treated BRPKp110 after 1 hr post overlay. Each data point represents paired measurements from one LN slice (n = 7/per group, LN slices obtained from 3 mice). Cancer cell positive area was compared via paired t-test. ***p < 0.001. (H) Invasion fold change of untreated WT BRPKp110 and PTx pre-treated BRPKp110 in CXCL13+ domain after 1 hr post overlay. Each data point represents invasion fold per LN slice (n = 15 slices, LN slices obtained from 3 mice). Invasion fold change was compared using a two-way ANOVA, followed by Sidak posthoc test. *p < 0.05.

6.3.6 Primary pre-metastatic TDLNs experienced reduced initial invasion of cancer cells despite increased chemokine secretion

Having established the model of cancer cell invasion in naïve LN slices, we proceeded to apply this model to predict invasion dynamics within the pre-metastatic TDLN in breast cancer. Standard in vivo experiments are complicated by the fact that the tumor and TDLN co-evolve. Therefore, here we applied the ex vivo model of invasion to address whether identical cancer cells invaded differently into pre-metastatic TDLN vs naïve LN.

To generate TDLN, we used a well-established murine model of breast cancer, in which BRPKp100 cells were inoculated into the fourth abdominal mammary fat pad on each side of the animal (Figure 6.7A). In this model, the inguinal TDLN (iTDLN) and axillary TDLN (aTDLN) represent the primary and secondary TDLNs, respectively.[54] TDLNs were harvested at day 5 post tumor inoculation, a timepoint preceding palpable tumor formation (Figure 6.7B), when no BRPKp110 cells (anti-GFP+ CD45-) were detectable in the TDLNs via flow cytometry (Figures S6.17, 6.7C). Therefore, we considered this timepoint to be pre-metastatic, though we cannot exclude the presence of a small, undetectable number of cells or tumor-derived fragments.

To compare the invasion potential of pre-metastatic TDLN versus control LN, we seeded BRPKp110 cells from cell culture onto the day-5 ex vivo slices of TDLN or control LN from PBS-injected animals. As in naïve LN, cancer cells readily entered the TDLN slice ex vivo and converted from a round to spread morphology between 1 and 20 hr (Figure 6.7D). Strikingly, the fraction of LN area occupied by cancer cells was significantly lower in iTDLN slices compared to control LNs (Figures 6.7D, E). This reduction was observed both at the initial entry (25% decrease) and after 20 hr (19% decrease), suggesting less initial accumulation rather than reduced survival or proliferation in overnight culture.

To attempt to determine the origin of the reduced invasion into TDLN, we first tested whether levels of secreted chemokines were similarly reduced. However, overnight cultures of primary draining iTDLN tissue slices actually secreted significantly more CCL21 and CCL19 into the supernatant compared in comparison to aTDLN and control LN (Figure 6.7F), with a correlation between CCL19 and CCL21 secretion only in the iTDLNs (Figure S6.18). The secretion of CXCL12, and CXCL13 by TDLN was not different from that of LNs obtained from control mice, while CCL1 levels were below the limit of detection (Figures 7.7F, S6.19).

Additionally, immunofluorescence labeling revealed no differences in the fractions of area positive for immobilized chemokines between TDLNs and control LNs (Figure S6.20). Thus, the reduced invasion of cancer cells into iTDLN slices was not attributable to reduced secretion of secreted or immobilized chemokines, as secretion was unchanged or even increased. In agreement with these data, BRPKp110 cells showed similar migration in transwell assays towards media conditioned by pre-metastatic TDLNs as by naïve LN (Figure 7.7G). The migration was abolished by PTx treatment (Figure 7.7G) and was reduced in CXCR5 and CCR7 KO cells similarly to in WT cells (Figure S6.21). Together this data confirm that chemotaxis was intact towards TDLN conditioned media.

Next, we considered that reduced invasion might result from anti-tumor immunity in the pre-metastatic TDLNs. Recent studies have highlighted the emerging role of interleukin-21 (IL-21) in the immune response against breast cancer. In breast cancer patients, elevated levels of IL-21 in CD4+ T cells were linked to better prognostic outcomes.[55] Additionally, in a murine model of 4T1 breast cancer, elevated IL-21 was identified as a crucial regulator of CD8+ T-cell-mediated antitumor immunity in the pre-metastatic TDLN.[21] In line with those reports, we observed significantly increased levels of intranodal IL-21 in pre-metastatic (day 5) iTDLNs and aTDLNs from the BRPKp110 animals compared to PBS control animals (Figure 6.7H). Thus, reduced invasion of cancer cell into iTDLN correlated with increased intranodal levels of IL-21, consistent with potential immune activation.

In summary, the ex vivo LN slice model predicted a lower invasion potential of pre-metastatic iTDLNs compared to control LNs, which was not due to diminished chemokine secretion, and which correlated with elevated intranodal IL-21 in concordance with prior reports. Understanding the mechanism behind reduced invasion remains a key focus for future research.

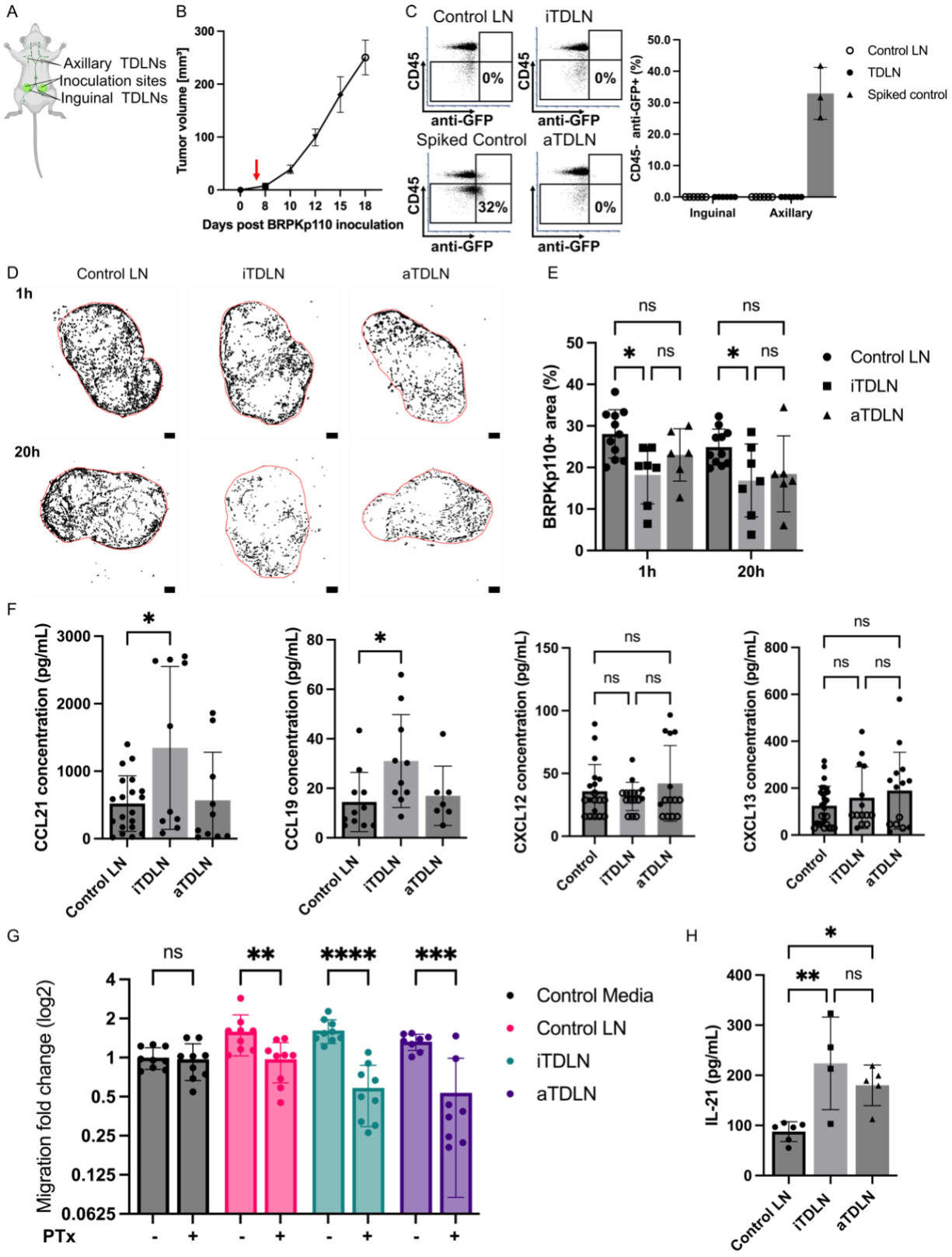

Figure 6.7: Reduced invasion of cancer cells in pre-metastatic iTDLN ex vivo. (A) Schematic illustration of in vivo model of breast cancer from which TDLN were obtained. Bottom-up view

of the animal. (B) Growth kinetics of BRPKp110 mammary tumors (n = 3 mice). (C) Flow cytometry analysis of cancer cell in TDLN. Quantification of CD45- anti-GFP+ cells in TDLNs 5 days post BRPKp110 inoculation. Mean ± standard deviation; each data point represents a fraction of CD45- anti-GFP+ cells per LN (n = 6 LNs/ group (inguinal, axillary) obtained from 3 tumor-bearing mice and 3 control mice injected with PBS). Fraction of CD45- anti-GFP+ cell was compared using a two-way ANOVA, followed by Tukey posthoc test. $p > 0.05$. (D) Representative images of cancer cell invasion (WT BRPKp110, black) into control LN, pre-metastatic iTDLN and aTDLN at 1 hr and 20 hr post overlay. Scale bar 200 μm. (E) BRPKp110+ area positive area in control LNs, a non-tumor mice injected with PBS, pre-metastatic iTDLN and aTDLN after 1h and 20h of culture. Mean ± standard deviation; each data point represents an individual LN slice (n=2-3/group, LN slices obtained from 3 mice). Cancer positive area was compared using a two-way ANOVA, followed by Tukey posthoc test. $*p < 0.05$. (F) Correlation of CCL21 and CCL19 chemokine levels in CM obtained from control LN, CM from culture pre-metastatic iTDLN and aTDLN. Linear regression and correlation between CCL21 and CCL19 levels were done with paired data from supernatants obtained from culture of Control LNs, iTDLNs and aTDLNs. Each data point represent supernatant (n=3/per group, LN slices obtained from 3 mice). Pearson r = 0.7870, R squared = 0.6194, $**p < 0.01$. (H) Intranodal levels of IL-21 in were significantly higher in pre-metastatic iTDLN and aTDLN than in control LN. Mean ± standard deviation; each data point represents the contents of 2 pooled LNs per mice per group (2x inguinal/ 2x axillary). Control n = 12 LNs, 3 mice. iTDLN n = 8 LNs, 4 mice, aTDLN = 10 LNs, 5 mice. Il-21 levels were compared using a two-way ANOVA, followed by Tukey posthoc test. $**p < 0.01$, $*p < 0.05$.

6.4 Discussion

In conclusion, this work utilized live LN tissue slices to model cancer cell spread within the complex LN microenvironment ex vivo. We demonstrated the application of this model to quantify the capacity of cancer cells to invade distinct regions of the LN in the absence of lymphatic barriers. Our novel model predicted a dynamic invasion of cancer cells, with an initial preferential accumulation in the SCS, followed by subsequent spread to the cortex and B-cell follicles. Furthermore, we tested the hypothesis that the chemotactic activity in live LN slices could serve as a model for the spatiotemporal recruitment of cancer cells within the LN. We identified that the preferential invasion of cancer cells correlated with the distribution of immobilized CXCL13 and

CCL1 chemokine-rich domains within the LN. Additionally, we showed that while blocking an individual chemokine led to reduced overall invasion, it was not sufficient to diminish cancer cell enrichment. This suggests that multiple chemokines concurrently regulate cancer cell chemotactic invasion in the spatially organized LN. Furthermore, we applied this system to model invasion into pre-metastatic TDLNs, addressing whether pre-metastatic nodes are more permissive or resistant to cancer cell invasion. In line with other models of breast cancer, our novel model predicted a lower invasion potential of cancer cells into pre-metastatic iTDLNs, which correlated with elevated intranodal IL-21 levels.

Overall, this innovative ex vivo model of cancer cell spread in live LNs enables a quantitative analysis of cancer cell region-specific invasion within the intricate tissue microenvironment. It enhances experimental accessibility, allowing for the simultaneous assessment of factors secreted by the live tissue and its effect on the patterns of invasion of cancer cells. Furthermore, the model set up allows for the manipulation of cancer cells in isolation, providing a controlled setting to test specific interactions. This novel ex vivo model lays a foundation for future research into the interplay between the microenvironmental cues of TDLN and their influence on cancer cell invasion.

Future research will aim to understand the mechanisms behind the reduced invasion into pre-metastatic TDLNs. Specifically, we will focus on the extent to which live TDLNs can induce cancer cell damage or death through immune cell-mediated killing and cytokine secretion. While we demonstrated that live LN slices effectively support the invasion of cancer cells for up to 20 hours of culture, the short duration remains a limitation. A 20-hr interaction may not fully capture the long-term interactions and progressive stages of cancer cell invasion and metastasis that occur in vivo. Future studies will aim to extend the culture duration and further explore these interactions

to enhance our understanding and therapeutic approaches. Lastly, although to our knowledge this model is the first to enable the spread of cancer cells within the cellular and anatomical complexity of the LN microenvironment, it lacks the functionality of the migratory cellular compartment. Further studies are needed to address this limitation.

6.5 References

(1) Siegel, R. L.; Miller, K. D.; Jemal, A. Cancer Statistics, 2020. *CA. Cancer J. Clin.* **2020**, *70* (1), 7–30. https://doi.org/10.3322/caac.21590.

(2) Redig, A. J.; McAllister, S. S. Breast Cancer as a Systemic Disease: A View of Metastasis. *J. Intern. Med.* **2013**, *274* (2), 113–126. https://doi.org/10.1111/joim.12084.

(3) Ran, S.; Volk, L.; Hall, K.; Flister, M. J. Lymphangiogenesis and Lymphatic Metastasis in Breast Cancer. *Pathophysiology* **2010**, *17* (4), 229–251. https://doi.org/10.1016/j.pathophys.2009.11.003.

(4) du Bois, H.; Heim, T. A.; Lund, A. W. Tumor-Draining Lymph Nodes: At the Crossroads of Metastasis and Immunity. *Sci. Immunol.* **2021**, *6* (63), eabg3551. https://doi.org/10.1126/sciimmunol.abg3551.

(5) Steeg, P. S. Tumor Metastasis: Mechanistic Insights and Clinical Challenges. *Nat. Med.* **2006**, *12* (8), 895–904. https://doi.org/10.1038/nm1469.

(6) Ji, H.; Hu, C.; Yang, X.; Liu, Y.; Ji, G.; Ge, S.; Wang, X.; Wang, M. Lymph Node Metastasis in Cancer Progression: Molecular Mechanisms, Clinical Significance and Therapeutic Interventions. *Signal Transduct. Target. Ther.* **2023**, *8* (1), 367. https://doi.org/10.1038/s41392-023-01576-4.

(7) Reticker-Flynn, N. E.; Zhang, W.; Belk, J. A.; Basto, P. A.; Escalante, N. K.; Pilarowski, G. O. W.; Bejnood, A.; Martins, M. M.; Kenkel, J. A.; Linde, I. L.; Bagchi, S.; Yuan, R.; Chang,

S.; Spitzer, M. H.; Carmi, Y.; Cheng, J.; Tolentino, L. L.; Choi, O.; Wu, N.; Kong, C. S.; Gentles, A. J.; Sunwoo, J. B.; Satpathy, A. T.; Plevritis, S. K.; Engleman, E. G. Lymph Node Colonization Induces Tumor-Immune Tolerance to Promote Distant Metastasis. *Cell* **2022**, *185* (11), 1924-1942.e23. https://doi.org/10.1016/j.cell.2022.04.019.

(8) Nathanson, S. D.; Kwon, D.; Kapke, A.; Alford, S. H.; Chitale, D. The Role of Lymph Node Metastasis in the Systemic Dissemination of Breast Cancer. *Ann. Surg. Oncol.* **2009**, *16* (12), 3396–3405. https://doi.org/10.1245/s10434-009-0659-2.

(9) Brown, M.; Assen, F. P.; Leithner, A.; Abe, J.; Schachner, H.; Asfour, G.; Bago-Horvath, Z.; Stein, J. V.; Uhrin, P.; Sixt, M.; Kerjaschki, D. Lymph Node Blood Vessels Provide Exit Routes for Metastatic Tumor Cell Dissemination in Mice. *Science* **2018**, *359* (6382), 1408–1411. https://doi.org/10.1126/science.aal3662.

(10) Pereira, E. R.; Kedrin, D.; Seano, G.; Gautier, O.; Meijer, E. F. J.; Jones, D.; Chin, S.-M.; Kitahara, S.; Bouta, E. M.; Chang, J.; Beech, E.; Jeong, H.-S.; Carroll, M. C.; Taghian, A. G.; Padera, T. P. Lymph Node Metastases Can Invade Local Blood Vessels, Exit the Node, and Colonize Distant Organs in Mice. *Science* **2018**, *359* (6382), 1403–1407. https://doi.org/10.1126/science.aal3622.

(11) Riedel, A.; Shorthouse, D.; Haas, L.; Hall, B. A.; Shields, J. Tumor-Induced Stromal Reprogramming Drives Lymph Node Transformation. *Nat. Immunol.* **2016**, *17* (9), 1118–1127. https://doi.org/10.1038/ni.3492.

(12) Qian, C.-N.; Berghuis, B.; Tsarfaty, G.; Bruch, M.; Kort, E. J.; Ditlev, J.; Tsarfaty, I.; Hudson, E.; Jackson, D. G.; Petillo, D.; Chen, J.; Resau, J. H.; Teh, B. T. Preparing the "Soil": The Primary Tumor Induces Vasculature Reorganization in the Sentinel Lymph Node before the Arrival

of Metastatic Cancer Cells. *Cancer Res.* **2006**, *66* (21), 10365–10376. https://doi.org/10.1158/0008-5472.CAN-06-2977.

(13) Das, S.; Sarrou, E.; Podgrabinska, S.; Cassella, M.; Mungamuri, S. K.; Feirt, N.; Gordon, R.; Nagi, C. S.; Wang, Y.; Entenberg, D.; Condeelis, J.; Skobe, M. Tumor Cell Entry into the Lymph Node Is Controlled by CCL1 Chemokine Expressed by Lymph Node Lymphatic Sinuses. *J. Exp. Med.* **2013**, *210* (8), 1509–1528. https://doi.org/10.1084/jem.20111627.

(14) Martinez, V. G.; Pankova, V.; Krasny, L.; Singh, T.; Makris, S.; White, I. J.; Benjamin, A. C.; Dertschnig, S.; Horsnell, H. L.; Kriston-Vizi, J.; Burden, J. J.; Huang, P. H.; Tape, C. J.; Acton, S. E. Fibroblastic Reticular Cells Control Conduit Matrix Deposition during Lymph Node Expansion. *Cell Rep.* **2019**, *29* (9), 2810-2822.e5. https://doi.org/10.1016/j.celrep.2019.10.103.

(15) Pereira, E. R.; Jones, D.; Jung, K.; Padera, T. P. The Lymph Node Microenvironment and Its Role in the Progression of Metastatic Cancer. *Semin. Cell Dev. Biol.* **2015**, *38*, 98–105. https://doi.org/10.1016/j.semcdb.2015.01.008.

(16) Cochran, A. J.; Huang, R.-R.; Lee, J.; Itakura, E.; Leong, S. P. L.; Essner, R. Tumour–Induced Immune Modulation of Sentinel Lymph Nodes. *Nat. Rev. Immunol.* **2006**, *6* (9), 659–670. https://doi.org/10.1038/nri1919.

(17) Preynat-Seauve, O.; Contassot, E.; Schuler, P.; Piguet, V.; French, L. E.; Huard, B. Extralymphatic Tumors Prepare Draining Lymph Nodes to Invasion via a T-Cell Cross-Tolerance Process. *Cancer Res.* **2007**, *67* (10), 5009–5016. https://doi.org/10.1158/0008-5472.CAN-06-4494.

(18) Lee, E.; Pandey, N. B.; Popel, A. S. Pre-Treatment of Mice with Tumor-Conditioned Media Accelerates Metastasis to Lymph Nodes and Lungs: A New Spontaneous Breast Cancer Metastasis Model. *Clin. Exp. Metastasis* **2014**, *31* (1), 67–79. https://doi.org/10.1007/s10585-013-9610-9.

(19) Vinay, D. S.; Ryan, E. P.; Pawelec, G.; Talib, W. H.; Stagg, J.; Elkord, E.; Lichtor, T.; Decker, W. K.; Whelan, R. L.; Kumara, H. M. C. S.; Signori, E.; Honoki, K.; Georgakilas, A. G.; Amin, A.; Helferich, W. G.; Boosani, C. S.; Guha, G.; Ciriolo, M. R.; Chen, S.; Mohammed, S. I.; Azmi, A. S.; Keith, W. N.; Bilsland, A.; Bhakta, D.; Halicka, D.; Fujii, H.; Aquilano, K.; Ashraf, S. S.; Nowsheen, S.; Yang, X.; Choi, B. K.; Kwon, B. S. Immune Evasion in Cancer: Mechanistic Basis and Therapeutic Strategies. *Semin. Cancer Biol.* **2015**, *35*, S185–S198. https://doi.org/10.1016/j.semcancer.2015.03.004.

(20) Louie, D. A. P.; Oo, D.; Leung, G.; Lin, Y.; Stephens, M.; Alrashed, O.; Tso, M.; Liao, S. Tumor-Draining Lymph Node Reconstruction Promotes B Cell Activation During E0771 Mouse Breast Cancer Growth. *Front. Pharmacol.* **2022**, *13*, 825287. https://doi.org/10.3389/fphar.2022.825287.

(21) Mao, X.; Tang, X.; Pan, H.; Yu, M.; Ji, S.; Qiu, W.; Che, N.; Zhang, K.; Huang, Z.; Jiang, Y.; Wang, J.; Zhong, Z.; Wang, J.; Liu, M.; Chen, M.; Zhou, W.; Wang, S. B Cells and IL-21-Producing Follicular Helper T Cells Cooperate to Determine the Dynamic Alterations of Premetastatic Tumor Draining Lymph Nodes of Breast Cancer. *Research* **2024**, *7*, 0346. https://doi.org/10.34133/research.0346.

(22) Greenlee, J. D.; King, M. R. Engineered Fluidic Systems to Understand Lymphatic Cancer Metastasis. *Biomicrofluidics* **2020**, *14* (1), 011502. https://doi.org/10.1063/1.5133970.

(23) Birmingham, K. G.; O'Melia, M. J.; Bordy, S.; Reyes Aguilar, D.; El-Reyas, B.; Lesinski, G.; Thomas, S. N. Lymph Node Subcapsular Sinus Microenvironment-On-A-Chip Modeling Shear Flow Relevant to Lymphatic Metastasis and Immune Cell Homing. *iScience* **2020**, *23* (11), 101751. https://doi.org/10.1016/j.isci.2020.101751.

(24) Shim, S.; Belanger, M. C.; Harris, A. R.; Munson, J. M.; Pompano, R. R. Two-Way Communication between *Ex Vivo* Tissues on a Microfluidic Chip: Application to Tumor–Lymph Node Interaction. *Lab. Chip* **2019**, *19* (6), 1013–1026. https://doi.org/10.1039/C8LC00957K.

(25) Tian, Y. F.; Ahn, H.; Schneider, R. S.; Yang, S. N.; Roman-Gonzalez, L.; Melnick, A. M.; Cerchietti, L.; Singh, A. Integrin-Specific Hydrogels as Adaptable Tumor Organoids for Malignant B and T Cells. *Biomaterials* **2015**, *73*, 110–119. https://doi.org/10.1016/j.biomaterials.2015.09.007.

(26) Faria, C.; Gava, F.; Gravelle, P.; Valero, J. G.; Dobaño-López, C.; Van Acker, N.; Quelen, C.; Jalowicki, G.; Morin, R.; Rossi, C.; Lagarde, J.-M.; Fournié, J.-J.; Ysebaert, L.; Laurent, C.; Pérez-Galán, P.; Bezombes, C. Patient-Derived Lymphoma Spheroids Integrating Immune Tumor Microenvironment as Preclinical Follicular Lymphoma Models for Personalized Medicine. *J. Immunother. Cancer* **2023**, *11* (10), e007156. https://doi.org/10.1136/jitc-2023-007156.

(27) Kastenschmidt, J. M.; Schroers-Martin, J. G.; Sworder, B. J.; Sureshchandra, S.; Khodadoust, M. S.; Liu, C. L.; Olsen, M.; Kurtz, D. M.; Diehn, M.; Wagar, L. E.; Alizadeh, A. A. A Human Lymphoma Organoid Model for Evaluating and Targeting the Follicular Lymphoma Tumor Immune Microenvironment. *Cell Stem Cell* **2024**, *31* (3), 410-420.e4. https://doi.org/10.1016/j.stem.2024.01.012.

(28) Brodt, P. Tumor Cell Adhesion to Frozen Lymph Node Sections—Anin Vitro Correlate of Lymphatic Metastasis. *Clin. Exp. Metastasis* **1989**, *7* (3), 343–352. https://doi.org/10.1007/BF01753685.

(29) Salmon, H.; Rivas-Caicedo, A.; Asperti-Boursin, F.; Lebugle, C.; Bourdoncle, P.; Donnadieu, E. Ex Vivo Imaging of T Cells in Murine Lymph Node Slices with Widefield and Confocal Microscopes. *J. Vis. Exp.* **2011**, No. 53, 3054. https://doi.org/10.3791/3054.

(30) Groff, B. D.; Kinman, A. W. L.; Woodroof, J. F.; Pompano, R. R. Immunofluorescence Staining of Live Lymph Node Tissue Slices. *J. Immunol. Methods* **2019**, *464*, 119–125. https://doi.org/10.1016/j.jim.2018.10.010.

(31) Belanger, M. C.; Ball, A. G.; Catterton, M. A.; Kinman, A. W. L.; Anbaei, P.; Groff, B. D.; Melchor, S. J.; Lukens, J. R.; Ross, A. E.; Pompano, R. R. Acute Lymph Node Slices Are a Functional Model System to Study Immunity Ex Vivo. *ACS Pharmacol. Transl. Sci.* **2021**, *4* (1), 128–142. https://doi.org/10.1021/acsptsci.0c00143.

(32) Katakai, T.; Habiro, K.; Kinashi, T. Dendritic Cells Regulate High-Speed Interstitial T Cell Migration in the Lymph Node via LFA-1/ICAM-1. *J. Immunol.* **2013**, *191* (3), 1188–1199. https://doi.org/10.4049/jimmunol.1300739.

(33) Belanger, M. C.; Ball, A. G.; Catterton, M. A.; Kinman, A. W. L.; Anbaei, P.; Groff, B. D.; Melchor, S. J.; Lukens, J. R.; Ross, A. E.; Pompano, R. R. Acute Lymph Node Slices Are a Functional Model System to Study Immunity Ex Vivo. *ACS Pharmacol. Transl. Sci.* **2021**, *4* (1), 128–142. https://doi.org/10.1021/acsptsci.0c00143.

(34) Chatziandreou, N.; Farsakoglu, Y.; Palomino-Segura, M.; D'Antuono, R.; Pizzagalli, D. U.; Sallusto, F.; Lukacs-Kornek, V.; Uguccioni, M.; Corti, D.; Turley, S. J.; Lanzavecchia, A.; Carroll, M. C.; Gonzalez, S. F. Macrophage Death Following Influenza Vaccination Initiates the Inflammatory Response That Promotes Dendritic Cell Function in the Draining Lymph Node. *Cell Rep.* **2017**, *18* (10), 2427–2440. https://doi.org/10.1016/j.celrep.2017.02.026.

(35) Harris, A. R.; Yuan, J. X.; Munson, J. M. Assessing Multiparametric Drug Response in Tissue Engineered Tumor Microenvironment Models. *Methods* **2018**, *134–135*, 20–31. https://doi.org/10.1016/j.ymeth.2017.12.010.

(36) Groff, B. D.; Kinman, A. W. L.; Woodroof, J. F.; Pompano, R. R. Immunofluorescence Staining of Live Lymph Node Tissue Slices. *J. Immunol. Methods* **2019**, *464*, 119–125. https://doi.org/10.1016/j.jim.2018.10.010.

(37) Schindelin, J.; Arganda-Carreras, I.; Frise, E.; Kaynig, V.; Longair, M.; Pietzsch, T.; Preibisch, S.; Rueden, C.; Saalfeld, S.; Schmid, B.; Tinevez, J.-Y.; White, D. J.; Hartenstein, V.; Eliceiri, K.; Tomancak, P.; Cardona, A. Fiji: An Open-Source Platform for Biological-Image Analysis. *Nat. Methods* **2012**, *9* (7), 676–682. https://doi.org/10.1038/nmeth.2019.

(38) Niemeier, L. A.; Dabbs, D. J.; Beriwal, S.; Striebel, J. M.; Bhargava, R. Androgen Receptor in Breast Cancer: Expression in Estrogen Receptor-Positive Tumors and in Estrogen Receptor-Negative Tumors with Apocrine Differentiation. *Mod. Pathol.* **2010**, *23* (2), 205–212. https://doi.org/10.1038/modpathol.2009.159.

(39) Rutkowski, M. R.; Allegrezza, M. J.; Svoronos, N.; Tesone, A. J.; Stephen, T. L.; Perales-Puchalt, A.; Nguyen, J.; Zhang, P. J.; Fiering, S. N.; Tchou, J.; Conejo-Garcia, J. R. Initiation of Metastatic Breast Carcinoma by Targeting of the Ductal Epithelium with Adenovirus-Cre: A Novel Transgenic Mouse Model of Breast Cancer. *J. Vis. Exp.* **2014**, No. 85, 51171. https://doi.org/10.3791/51171.

(40) The Cancer Genome Atlas Network. Comprehensive Molecular Portraits of Human Breast Tumours. *Nature* **2012**, *490* (7418), 61–70. https://doi.org/10.1038/nature11412.

(41) Wiley, H. E.; Gonzalez, E. B.; Maki, W.; Wu, M. -t.; Hwang, S. T. Expression of CC Chemokine Receptor-7 and Regional Lymph Node Metastasis of B16 Murine Melanoma. *JNCI J. Natl. Cancer Inst.* **2001**, *93* (21), 1638–1643. https://doi.org/10.1093/jnci/93.21.1638.

(42) Shields, J. D.; Emmett, M. S.; Dunn, D. B. A.; Joory, K. D.; Sage, L. M.; Rigby, H.; Mortimer, P. S.; Orlando, A.; Levick, J. R.; Bates, D. O. Chemokine-Mediated Migration of

Melanoma Cells towards Lymphatics – a Mechanism Contributing to Metastasis. *Oncogene* **2007**, *26* (21), 2997–3005. https://doi.org/10.1038/sj.onc.1210114.

(43) Kang, H.; Watkins, G.; Parr, C.; Douglas-Jones, A.; Mansel, R. E.; Jiang, W. G. Stromal Cell Derived Factor-1: Its Influence on Invasiveness and Migration of Breast Cancer Cells in Vitro, and Its Association with Prognosis and Survival in Human Breast Cancer. *Breast Cancer Res.* **2005**, *7* (4), R402. https://doi.org/10.1186/bcr1022.

(44) Hiller, D.; Chu, Q. D. CXCR4 and Axillary Lymph Nodes: Review of a Potential Biomarker for Breast Cancer Metastasis. *Int. J. Breast Cancer* **2011**, *2011*, 1–6. https://doi.org/10.4061/2011/420981.

(45) Sun, Y.; Mao, X.; Fan, C.; Liu, C.; Guo, A.; Guan, S.; Jin, Q.; Li, B.; Yao, F.; Jin, F. CXCL12-CXCR4 Axis Promotes the Natural Selection of Breast Cancer Cell Metastasis. *Tumor Biol.* **2014**, *35* (8), 7765–7773. https://doi.org/10.1007/s13277-014-1816-1.

(46) Li, X.; Sun, S.; Li, N.; Gao, J.; Yu, J.; Zhao, J.; Li, M.; Zhao, Z. High Expression of CCR7 Predicts Lymph Node Metastasis and Good Prognosis in Triple Negative Breast Cancer. *Cell. Physiol. Biochem.* **2017**, *43* (2), 531–539. https://doi.org/10.1159/000480526.

(47) Biswas, S.; Sengupta, S.; Roy Chowdhury, S.; Jana, S.; Mandal, G.; Mandal, P. K.; Saha, N.; Malhotra, V.; Gupta, A.; Kuprash, D. V.; Bhattacharyya, A. CXCL13–CXCR5 Co-Expression Regulates Epithelial to Mesenchymal Transition of Breast Cancer Cells during Lymph Node Metastasis. *Breast Cancer Res. Treat.* **2014**, *143* (2), 265–276. https://doi.org/10.1007/s10549-013-2811-8.

(48) Müller, A.; Homey, B.; Soto, H.; Ge, N.; Catron, D.; Buchanan, M. E.; McClanahan, T.; Murphy, E.; Yuan, W.; Wagner, S. N.; Barrera, J. L.; Mohar, A.; Verástegui, E.; Zlotnik, A.

Involvement of Chemokine Receptors in Breast Cancer Metastasis. *Nature* **2001**, *410* (6824), 50–56. https://doi.org/10.1038/35065016.

(49) Longo-Imedio, M. I.; Longo, N.; Treviño, I.; Lázaro, P.; Sánchez-Mateos, P. Clinical Significance of CXCR3 and CXCR4 Expression in Primary Melanoma. *Int. J. Cancer* **2005**, *117* (5), 861–865. https://doi.org/10.1002/ijc.21269.

(50) Kato, M.; Kitayama, J.; Kazama, S.; Nagawa, H. Expression Pattern of CXC Chemokine Receptor-4 Is Correlated with Lymph Node Metastasis in Human Invasive Ductal Carcinoma. *Breast Cancer Res.* **2003**, *5* (5), R144. https://doi.org/10.1186/bcr627.

(51) Sperveslage, J.; Frank, S.; Heneweer, C.; Egberts, J.; Schniewind, B.; Buchholz, M.; Bergmann, F.; Giese, N.; Munding, J.; Hahn, S. A.; Kalthoff, H.; Klöppel, G.; Sipos, B. Lack of CCR7 Expression Is Rate Limiting for Lymphatic Spread of Pancreatic Ductal Adenocarcinoma. *Int. J. Cancer* **2012**, *131* (4). https://doi.org/10.1002/ijc.26502.

(52) Panse, J.; Friedrichs, K.; Marx, A.; Hildebrandt, Y.; Luetkens, T.; Bartels, K.; Horn, C.; Stahl, T.; Cao, Y.; Milde-Langosch, K.; Niendorf, A.; Kröger, N.; Wenzel, S.; Leuwer, R.; Bokemeyer, C.; Hegewisch-Becker, S.; Atanackovic, D. Chemokine CXCL13 Is Overexpressed in the Tumour Tissue and in the Peripheral Blood of Breast Cancer Patients. *Br. J. Cancer* **2008**, *99* (6), 930–938. https://doi.org/10.1038/sj.bjc.6604621.

(53) Regulative Role of the CXCL13-CXCR5 Axis in the Tumor Microenvironment. *Precis. Clin. Med.* **2018**. https://doi.org/10.1093/pcmedi/pby006.

(54) Buchta Rosean, C.; Bostic, R. R.; Ferey, J. C. M.; Feng, T.-Y.; Azar, F. N.; Tung, K. S.; Dozmorov, M. G.; Smirnova, E.; Bos, P. D.; Rutkowski, M. R. Preexisting Commensal Dysbiosis Is a Host-Intrinsic Regulator of Tissue Inflammation and Tumor Cell Dissemination in Hormone

Receptor–Positive Breast Cancer. *Cancer Res.* **2019**, *79* (14), 3662–3675. https://doi.org/10.1158/0008-5472.CAN-18-3464.

(55) Balouchi-Anaraki, S.; Mohammadsadeghi, S.; Norouzian, M.; Rasolmali, R.; Talei, A.-R.; Mehdipour, F.; Ghaderi, A. Expression of Interleukin-21 and Interleukin-21 Receptor in Lymphocytes Derived from Tumor-Draining Lymph Nodes of Breast Cancer. *Breast Dis.* **2022**, *41* (1), 373–382. https://doi.org/10.3233/BD-220013.

6.6 Supplementary figures

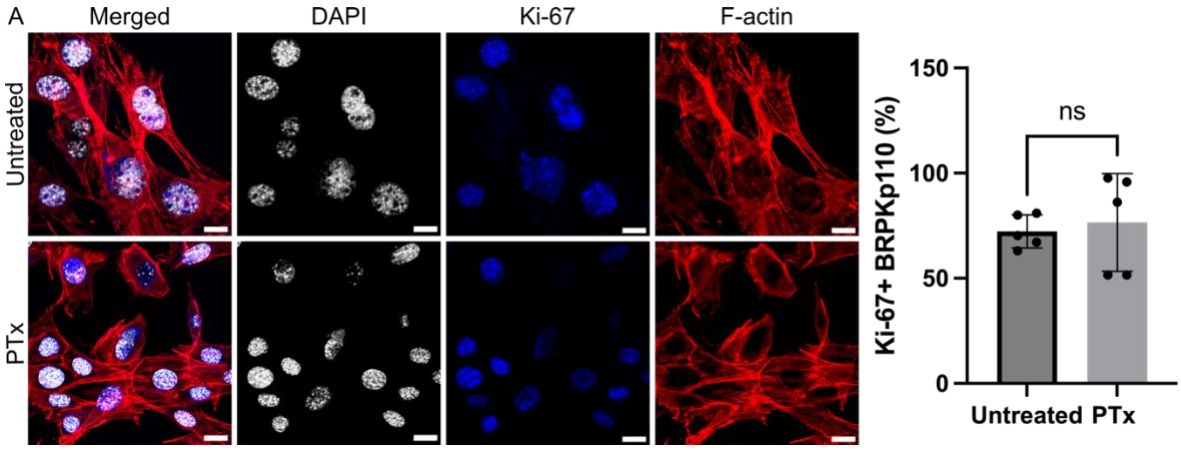

Figure 6.8: Impact of PTx treatment on BRPKp110 morphology and proliferation. Morphology and proliferation of BRPKp110 cells cultured with 100 ng/ml PTx for 20 hr. Cells are stained with rhodamine-labeled phalloidin (red), Dapi (nuclei; white) and Ki-67 (blue). Data are representative of three experiments. Scale bar 20 µm. No difference in percent of proliferating fraction Ki-67+ BRPKp110 cells was observed in cells treated with PTx. Each data point represents one biological replicate. Percent of Ki-67 positive cells per field of view in BRPKp110 cultured for 20h in media supplied with PTx or in a plain media (untreated). Mean ± standard deviation; each data point represent measurement from an individual sample (n=2-3/group, data pulled from 3 independent experiments). Fraction of Ki-67 positive cells between culture conditions was compared using unpaired t-test. $p > 0.05$

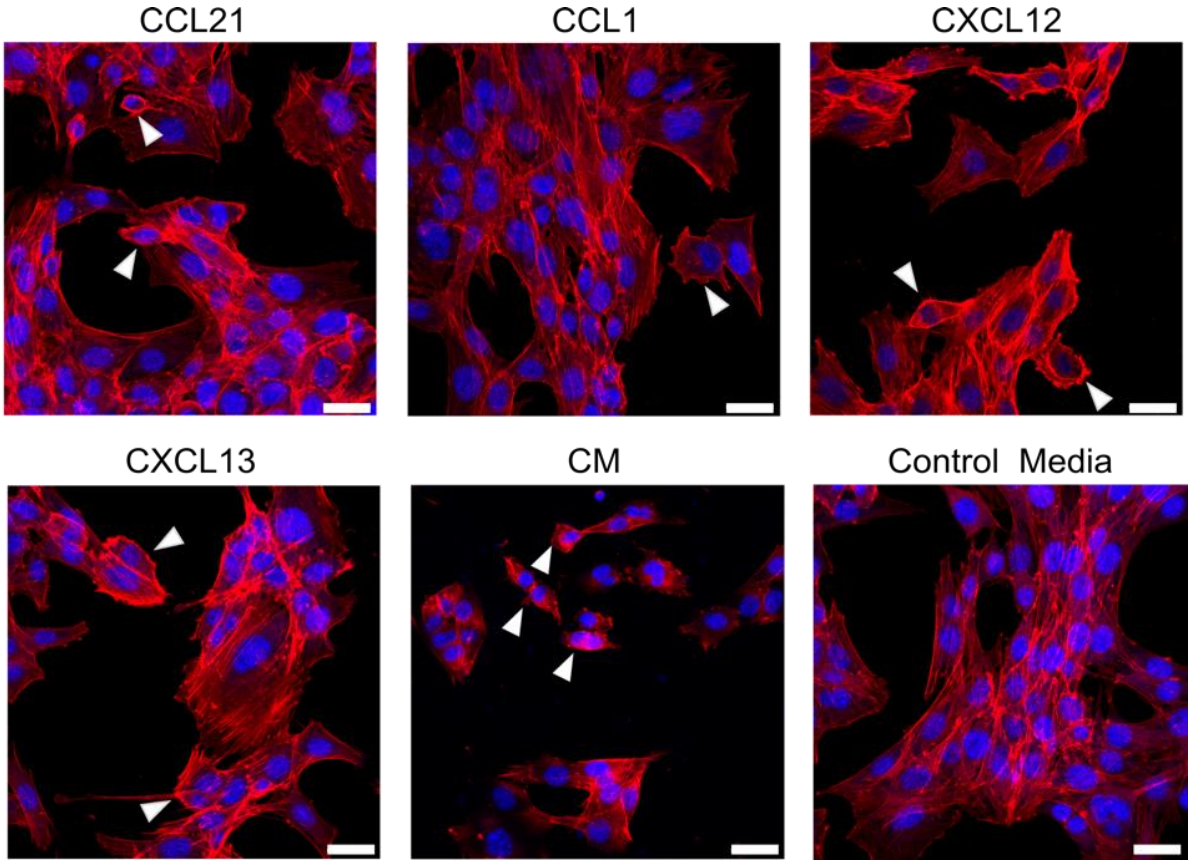

Figure 6.9: Effects of chemokines on BRPKp110 cancer cell morphology. Cells were stained with rhodamine-labeled phalloidin (red) and Dapi (nuclei; blue). Scale bar 20 µm. Data are representative of three experiments.

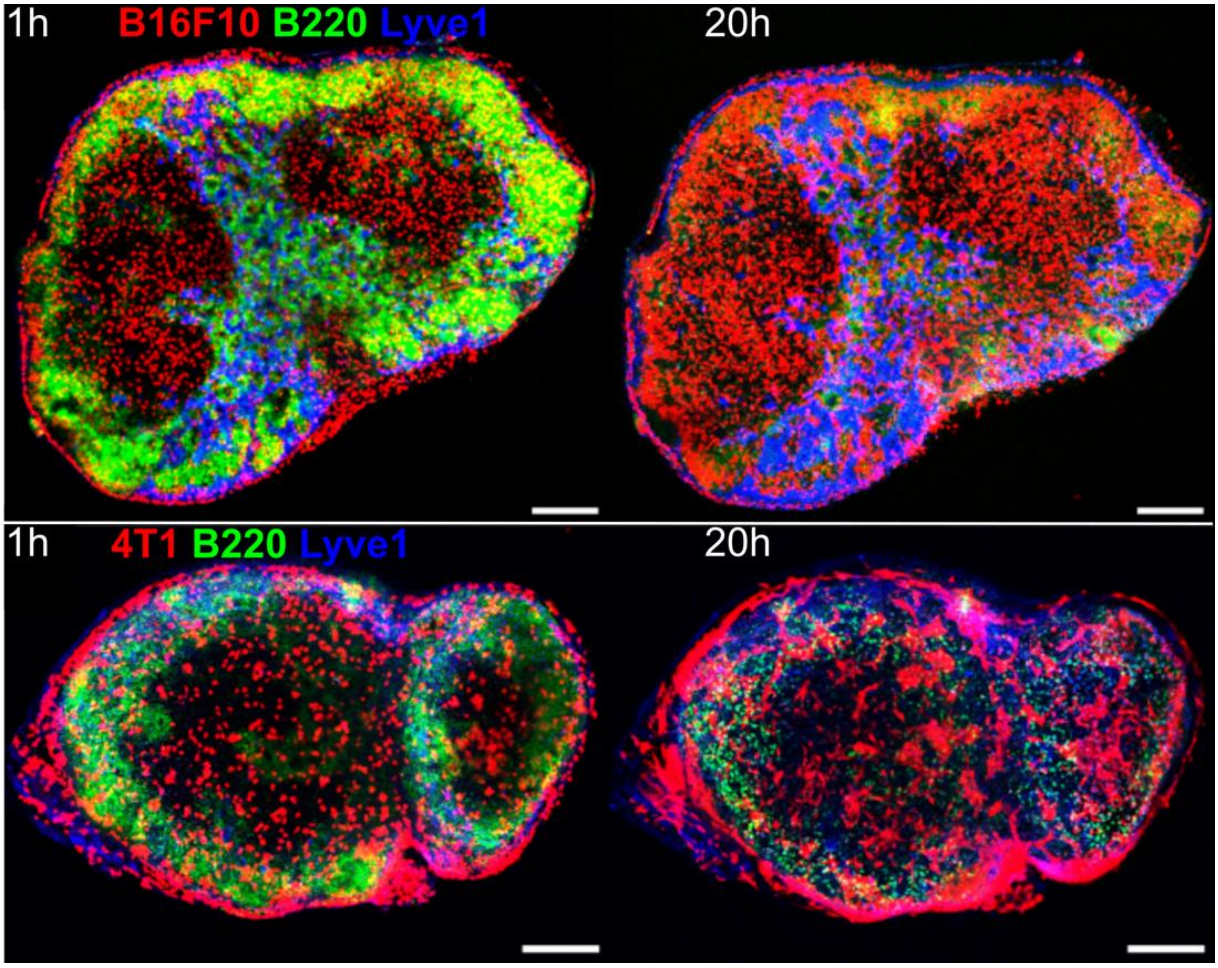

Figure 6.10: Cancer cells overlaid onto ex vivo LN slices infiltrate the tissue. Fluorescently labeled cancer cells (red) spread in naïve LN slice from 1-hr post seeding (left) to 20-hr of culture post seeding (right). B16F10 melanoma cells (red). 4T1 breast cancer cells (red). B220 (green) marks B cells. Lyve1 (blue) marks LECs. Scale bar 200 μm.

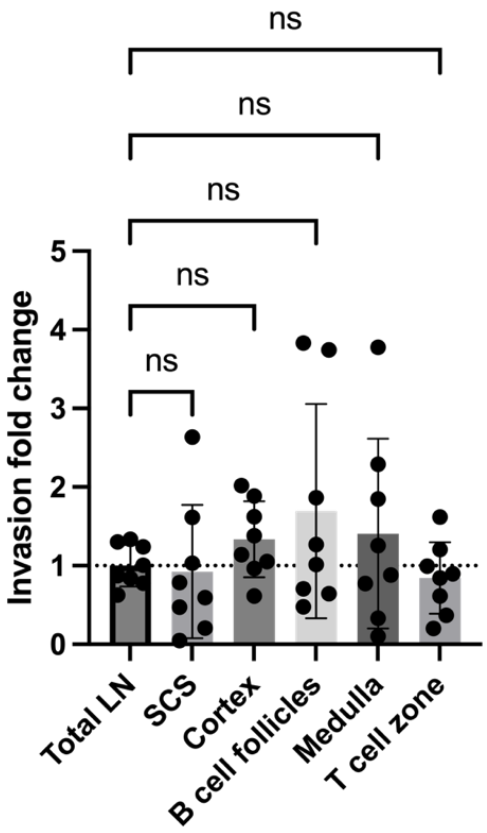

Figure 6.11: BRPKp110 invasion fold change after 40 hr of culture. Invasion fold change of BRPKp110 cells in LN regions in comparison to the average across the LN tissue. Mean ± standard deviation; dotted line represents normalized enrichment across the total area of the LN slice; each data point represents invasion fold change normalized to the total LN invasion on a per slice basis (n = 7-8/per group, LN slices obtained from 3 mice).

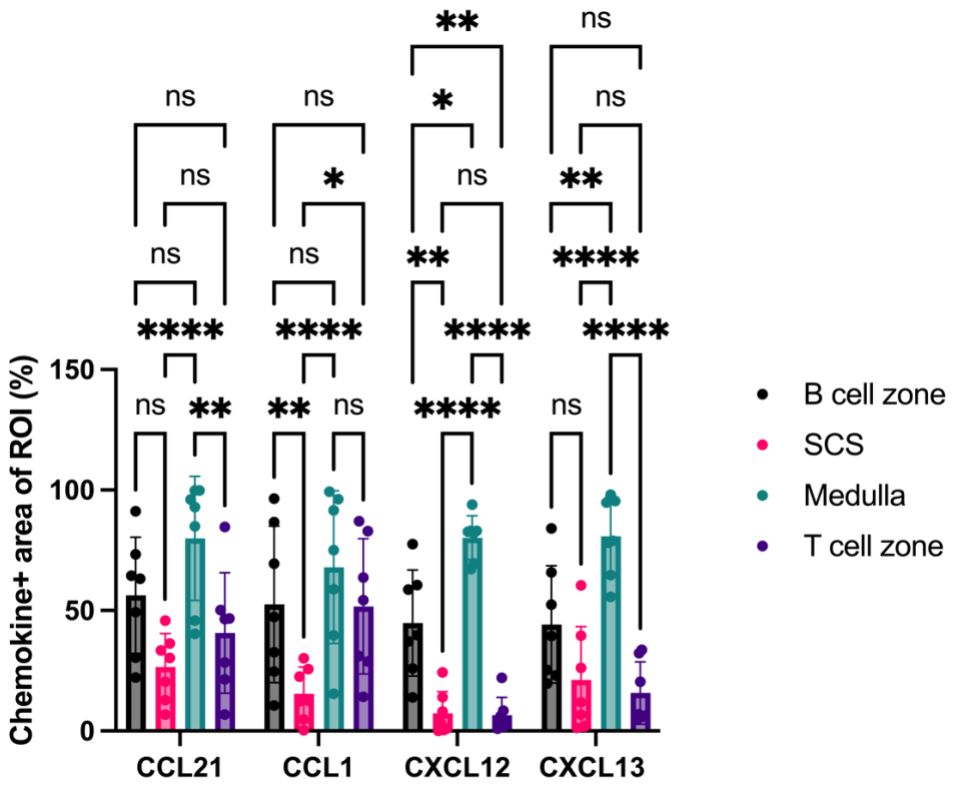

Figure 6.12: Distribution of immobilized chemokines within regions of LN tissue after 1 hr of culture. Fraction of total LN ROI positive for immobilized CCL21, CCL1, CXCL12 and CXCL13 measured in naive LN after 1 hr of culture. Mean ± standard deviation; each data point represents a LN slice (n=4-8/per group, LN slices obtained from 3 mice). Chemokine positive areas were compared using a two-way ANOVA, followed by Tukey posthoc test. *$p < 0.05$, **$p < 0.01$, ****$p < 0.0001$.

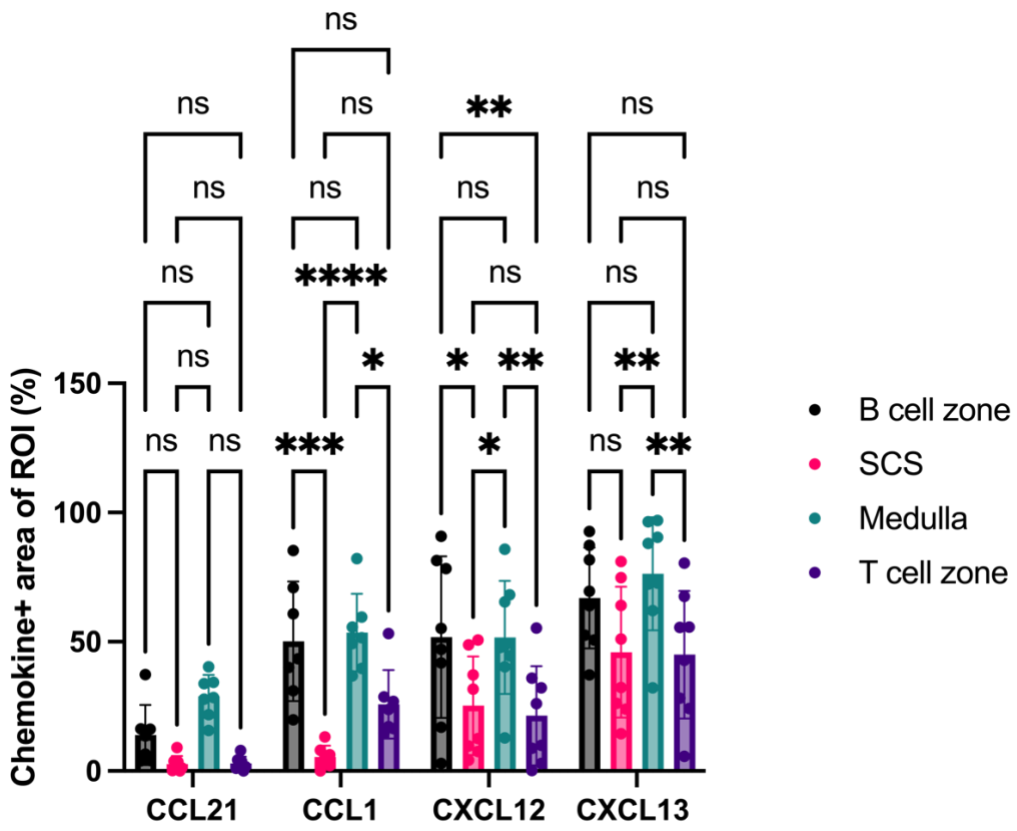

Figure 6.13: Distribution of immobilized chemokines within regions of LN tissue after 20 hr of culture. Fraction of total LN ROI positive for immobilized CCL21, CCL1, CXCL12 and CXCL13 measured in naive LN after 20 hr of culture. Mean ± standard deviation; each data point represents a LN slice (n=4-8/per group, LN slices obtained from 3 mice). Chemokine positive areas were compared using a two-way ANOVA, followed by Tukey posthoc test. *p < 0.05, **p < 0.01, ***p < 0.001 ,****p < 0.0001.

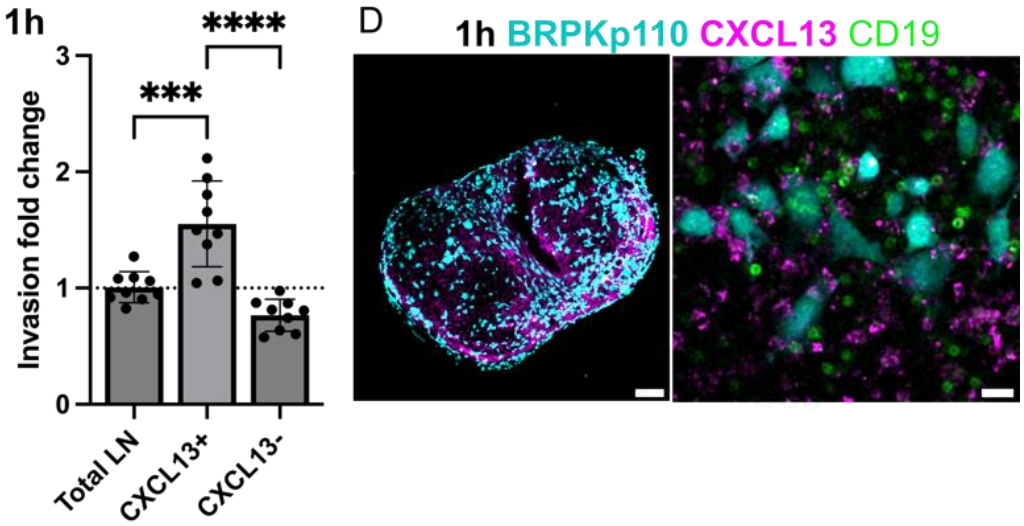

Figure 6.14: BRPKp110 invasion in CXCL13-rich domain after 1 hr of culture. Right: BRPKp110 invasion fold in CXCL13 positive (CXCL13+) and CXCL13 negative (CXCL13-) regions of LN tissue relative to the invasion to the total LN tissue after 1 hr of culture. Mean ± standard deviation; dotted line represents normalized enrichment across the total area of the LN slice; each data point represents invasion fold change normalized to the total LN invasion on a per slice basis. Invasion fold change was compared using a one-way ANOVA, followed by Tukey posthoc test *$p < 0.05$, ***$p < 0.001$. Left: Representative images of cancer cells (cyan) in CX CL13+ chemokine domain (magenta) after 1 hr of culture. Scale bar 200 µm.

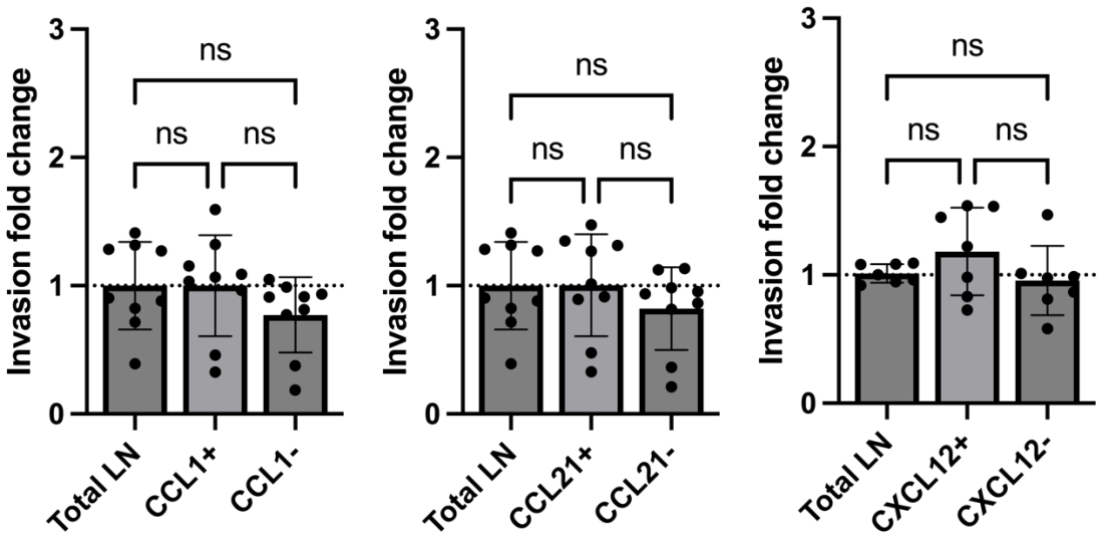

Figure 6.15: BRPKp110 invasion in chemokine-rich domians after 1 hr of culture. BRPKp110 invasion fold in CXCL13 positive (CXCL13+) and CXCL13 negative (CXCL13-) regions of LN tissue relative to the invasion to the total LN tissue after 1 hr of culture. Mean ± standard deviation; dotted line represents normalized enrichment across the total area of the LN slice; each data point represents invasion fold change normalized to the total LN invasion on a per slice basis. Invasion fold change was compared using a one-way ANOVA, followed by Tukey posthoc test *$p < 0.05$, ***$p < 0.001$. (D) Representative images of cancer cells (cyan) in CX CL13+ chemokine domain (magenta) after 1 hr of culture. Scale bar 200 μm.

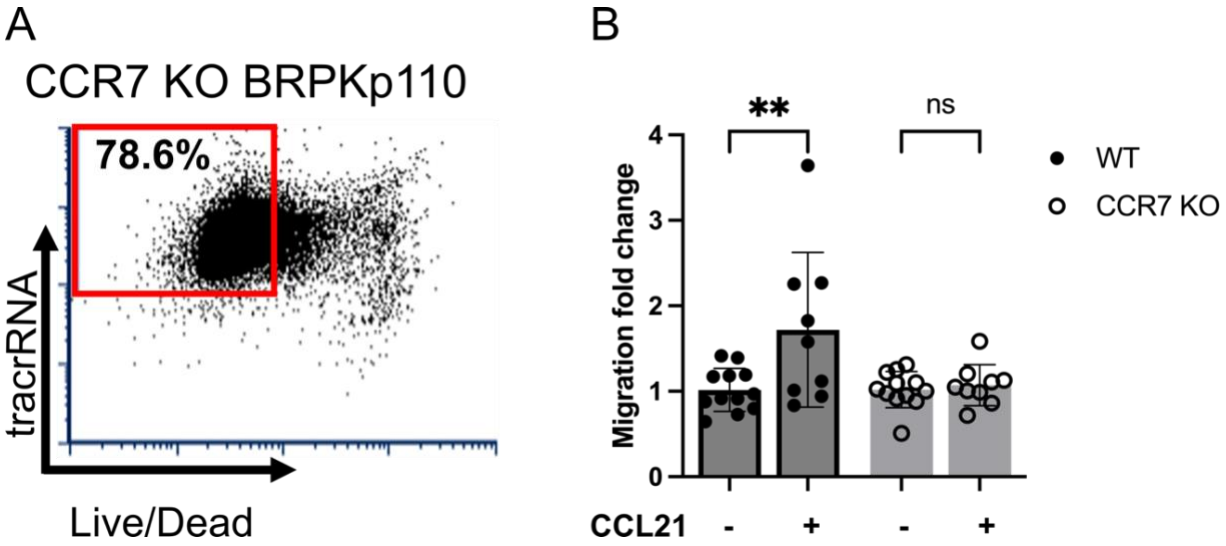

Figure 6.16: Loss of chemotactic function in BRPKp110 CCR7 KO. (A) Selection of tracrRNA positive cell population post-transfection (red), non-transfected control WT BRPKp110 (black). (B) CCR7 KO migration toward media containing 200 ng/mL of CCL21 was impaired, confirming the loss of receptor function. Each data point represents the mean migration fold change per membrane, calculated from three non-overlapping fields of view (n = 2-3 membranes/condition; normalized data pooled from 3 independent in vitro experiments). Migration fold change was compared using a two-way ANOVA, followed by Tukey posthoc test. ***$p < 0.0001$, *$p < 0.05$.

6.18 Correlation of CCL21 and CCL19 chemokine levels in CM obtained from control LN, CM from culture pre-metastatic iTDLN and aTDLN. Linear regression and correlation between CCL21 and CCL19 levels were done with paired data from supernatants obtained from culture of Control LNs, iTDLNs and aTDLNs. Each data point represent supernatant (n=3/per group, LN slices obtained from 3 mice). Pearson r = 0.7870, R squared = 0.6194, **$p < 0.01$.

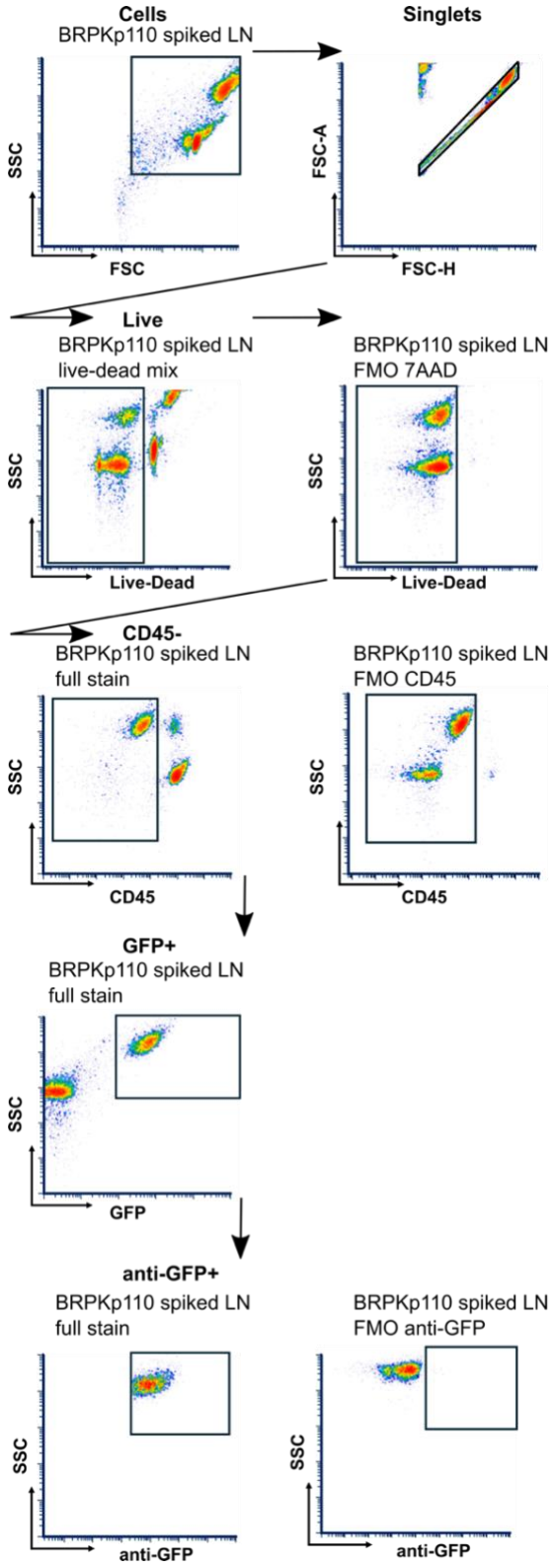

Figure 6.17: Gating strategy for quantification of cancer cells in TDLNs.

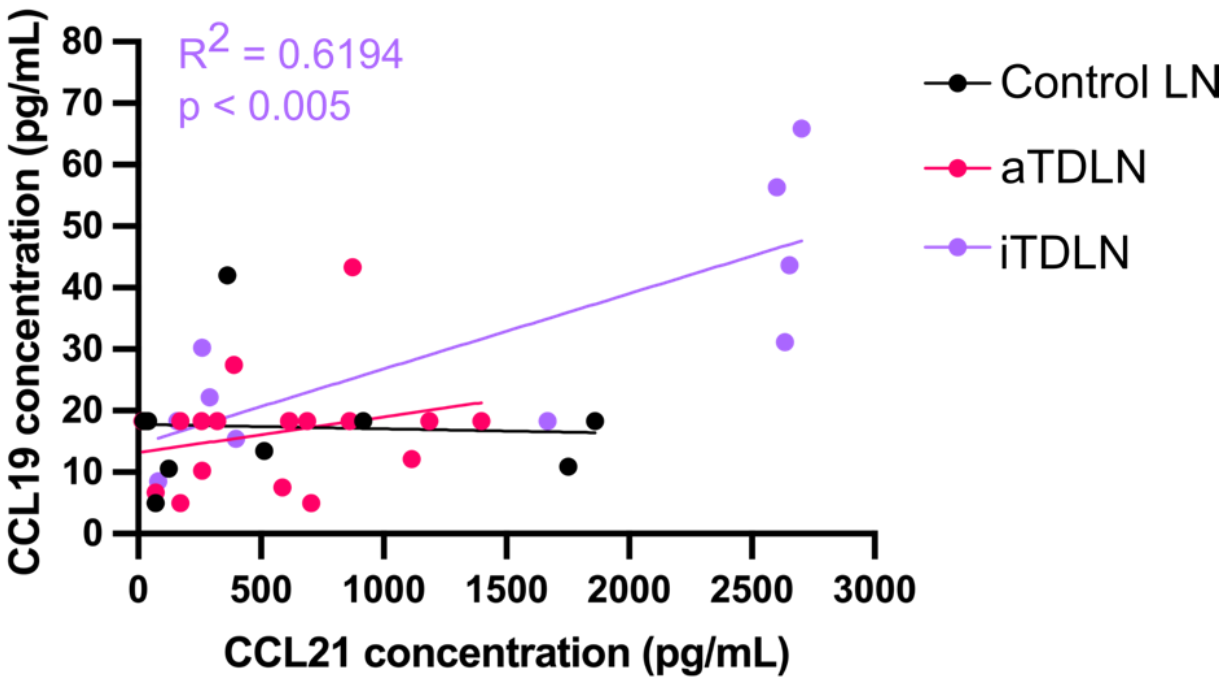

Figure 6.18: Correlation of CCL21 and CCL19 chemokine levels in CM. CM obtained from control LN, CM from culture pre-metastatic iTDLN and aTDLN. Linear regression and correlation between CCL21 and CCL19 levels were done with paired data from supernatants obtained from culture of Control LNs, iTDLNs and aTDLNs. Each data point represent supernatant (n=3/per group, LN slices obtained from 3 mice). Pearson r = 0.7870, R squared = 0.6194, **p < 0.01.

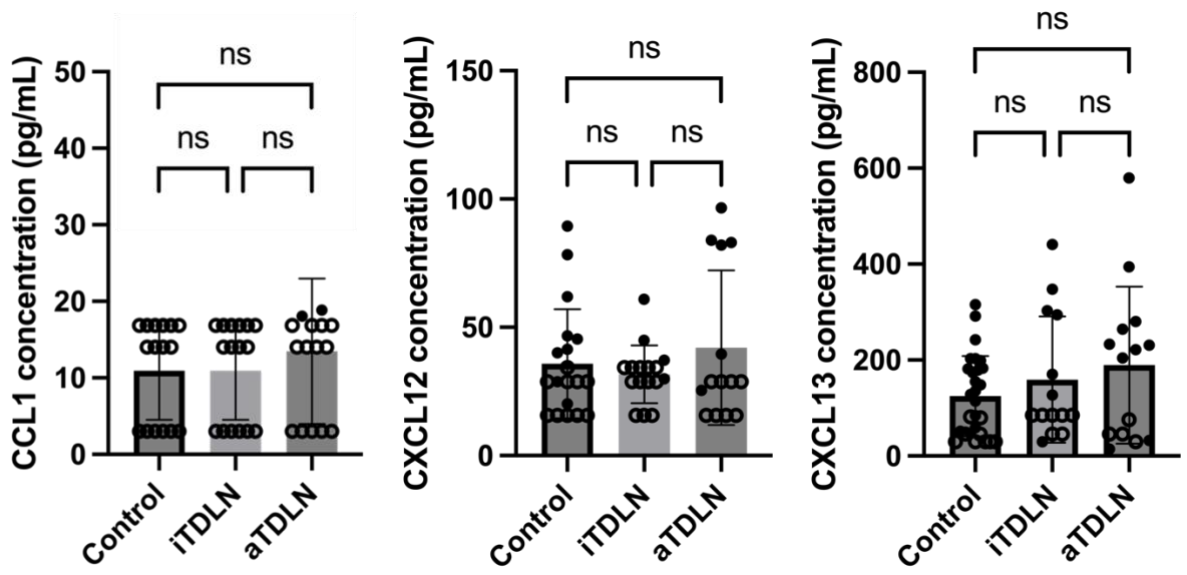

Figure 6.19: CCL1, CXCL12 and CXCL13 levels in CM. Concentrations of CCL1, CXCL12 and CXCL13 in live pre-metastatic TDLN slice CM following a 20 hr culture period. Mean ± standard deviation; each data point represent supernatant (n=3/per group, LN slices obtained from 3 mice). Chemokine concentrations were compared using a one-way ANOVA, followed by Tukey posthoc test. $p > 0.05$.

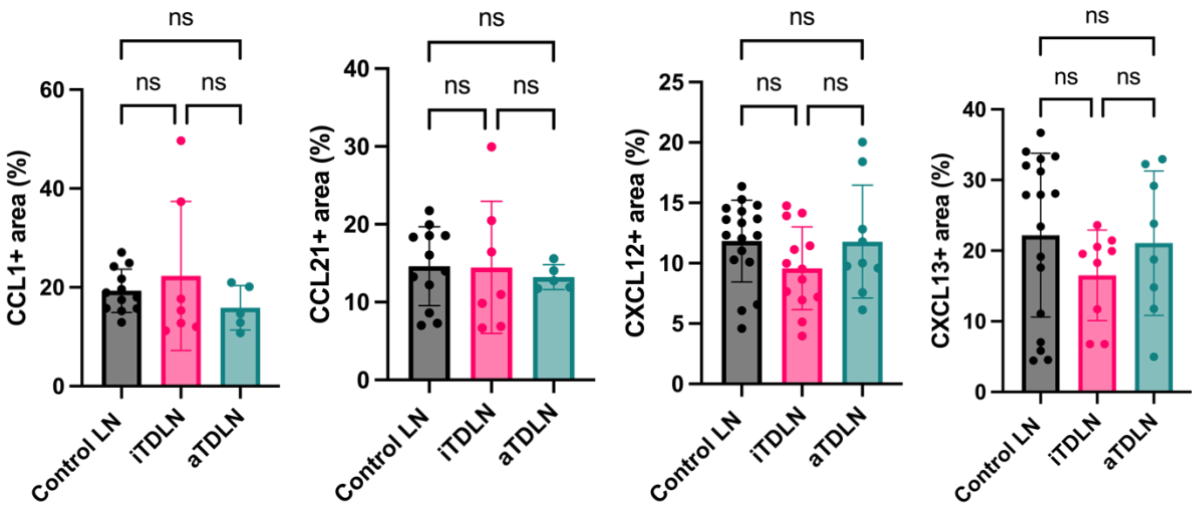

Figure 6.20: Comparison of immobilized chemokine positive areas in control LN and TDLNs. Fraction of total LN area positive for immobilized CCL1, CCL21, CXCL12 and CXCL13 measured in control LN and pre-metastatic iTDLN and aTDLN. Mean ± standard deviation; each data point represents a LN slice (n=4-8/per group, LN slices obtained from 3 mice). Chemokine positive areas were compared using a one-way ANOVA, followed by Tukey posthoc test. $p > 0.05$.

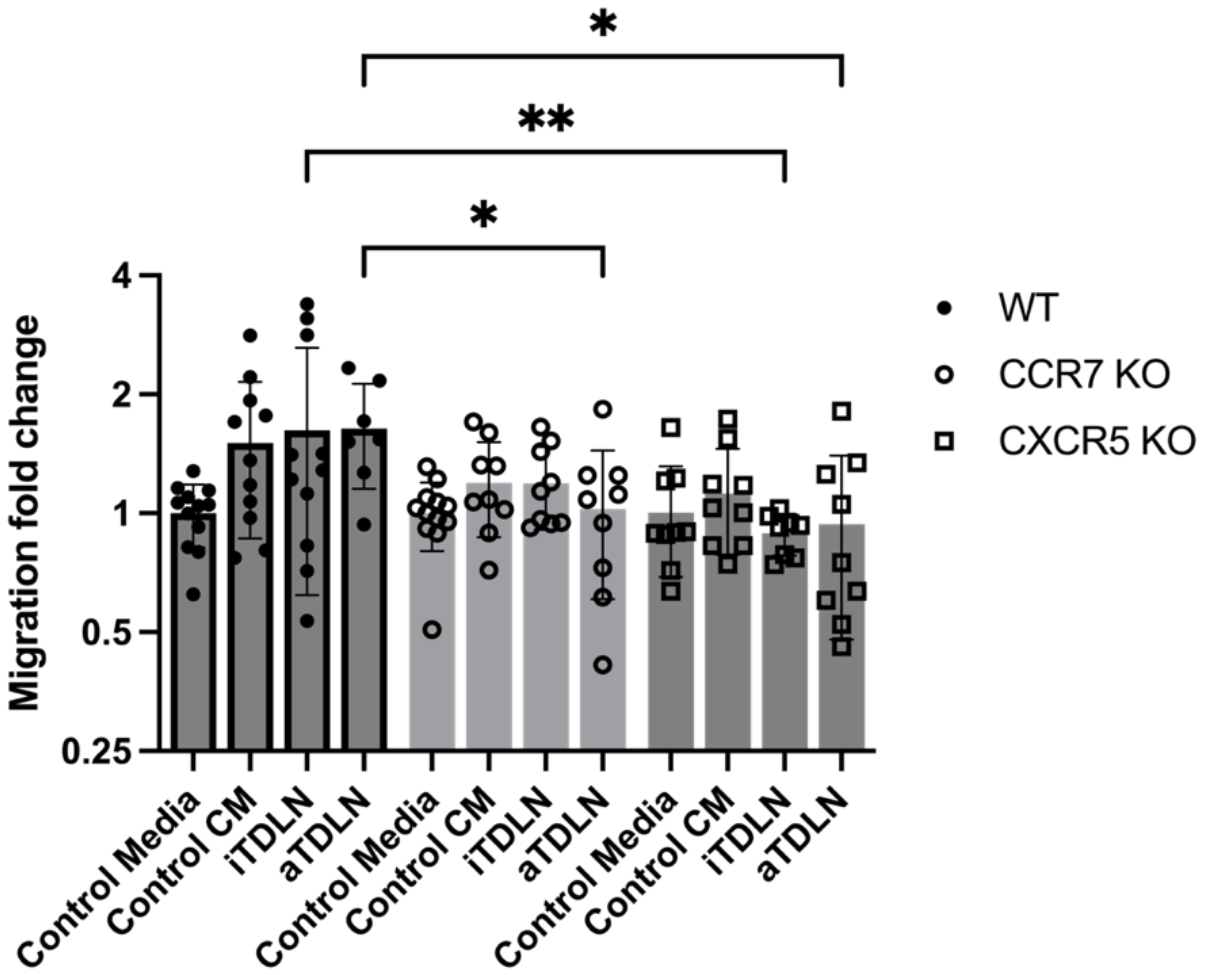

Figure 6.21: Migration of WT and KO BRPKp110 towards TDLN CM. Migration in KO cell lines towards TDLN was impaired yet remained comparable to migration towards Control CM. Mean ± standard deviation; each data point represents the mean migration fold change per membrane, calculated from three non-overlapping fields of view (n = 3-4 membranes/condition; normalized data pooled from 3 independent in vitro experiments). Migration fold change was compared using a two-way ANOVA, followed by Tukey posthoc test. **$p < 0.001$, *$p < 0.05$.

6.7 Supplementary tables

Resource	Vendor	Identifier
anti-mouse CD16/32, clone 93, Rat IgG2a, κ	BioLegend	101302
anti-mouse Ki-67 antibody, clone 16A8, Isotype Rat IgG2a, κ	BioLegend	652407
anti-mouse APC CD197 (CCR7) clone 4B12, Rat IgG2a, κ	BioLegend	120107
anti-mouse APC CD198 (CCR8) clone SA214G2, Rat IgG2b, κ	BioLegend	150309
anti-mouse APC CD184 (CXCR4) clone L276F12, Rat IgG2b, κ	BioLegend	146507
anti-mouse APC CD185 (CXCR5) clone L138D7, Rat IgG2b, κ	BioLegend	145505
Isotype Control APC RatIgG2a, clone RTK2758, Rat IgG2a, κ	BioLegend	400511
Isotype Control APC Rat IgG2b, κ, clone RTK4530	BioLegend	400611
Briliant Violet 421 anti-mouse podoplanin, clone 8.1.1, Syrian Hamster IgG	BioLegend	127423
Alexa Fluor 647 anti-mouse lyve1, clone ALY7, Rat IgG1,κ	Invitrogen	53-0443-82
Alexa Fluor 488 anti-mouse B220, clone RA3-6B2, Rat IgG2a, κ	BioLegend	103229
Starbright Violet 670 anti-mouse CD19, clone 6D5 , Rat IgG2a, κ	Bio-Rad	MCA1439SBV67
PE anti-mouse CD45, clone 30-F11, Isotype Rat IgG2b, κ	BioLegend	103105
APC anti-GFP Antibody, clone FM264, Rat IgG2a, κ	BioLegend	338010

Table 6.1: List of used antibodies.

crRNA	Sequence (5′-3′)	PAM
CCR7-1	CATCGGCGAGAATACCACGG	TGG
CCR7-2	GTACAGGGTGTAGTCCACCG	TGG
CCR7-3	CCTGGACGATGGCTACGTAG	CGG
CCR8-1	TCGTGGGCTGCAAGAAACTG	AGG
CCR8-2	CCTTGATGGCATAGACAGCG	TGG
CCR8-3	TCTTGGATGGATGTGCCACG	AGG
CXCR4-1	TGGAGACTATGACTCCAACA	AGG
CXCR4-2	TCTTTGCCGACGTCAGCCAG	GGG
CXCR4-3	CTTTGCCGACGTCAGCCAGG	GGG
CXCR5-1	TTGGTGCGTAGAATCCACGA	GGG
CXCR5-2	GTGGATTCTACGCACCAATG	GGG
CXCR5-3	TACCCACTAACCCTGGACAT	GGG

Table 6.2: List of used crRNA sequences.

7 Characterization of TDLN remodeling in in vivo model of BRPKp110 breast cancer

7.1 Introduction

Although the clinical paradigm that tumors often engage the lymphatic system is widely recognized, there is a significant knowledge gap regarding the specific events required for metastatic seeding in the TDLN.[1] Preceding tumor invasion, the TDLN undergoes profound structural and functional changes including organ enlargement,[2] increase in fluid permissiveness[3] and shift in cytokine expression,[4] all of which may create a more favorable environment for tumor seeding and metastatic outgrowth.

We hypothesize that these physical and biochemical changes, such as stromal expansion and altered cytokine signaling, collectively create a microenvironment that supports cancer cell invasion within TDLNs. To characterize these changes, we quantified stromal remodeling and chemokine secretion in TDLNs at early and advanced stages of disease progression (day 5, day 18, and day 26 post-inoculation) using in vivo model of murine breast cancer (syngeneic GFP+ BRPKp110 breast tumor cell line in C57Bl/6 female mice).

7.2 Methods

7.2.1 Cell culture

Mouse mammary cancer cell lines BRPKp110-GFP+ were obtained from Melanie Rutkowski, University of Virginia. Cells were cultured in RMPI (Gibco, 2505339) supplemented with 10% FBS (Corning Heat-inactivated, USDA approved origin, lot: 301210001), 1x L-glutamine (Gibco

Life Technologies, lot: 2472354), 50 U/mL Pen/Strep (Gibco, lot: 2441845), 50 µM beta-mercaptoethanol (Gibco, 21985-023), 1 mM sodium pyruvate (Hyclone, 2492879), 1× non-essential amino acids (GIBCO, 2028868), and 20 mM HEPES (Gibco, 15630-060). Cells were seeded in T75 or T175 flasks (Nunc™ EasYFlask™, Fisher Scientific) following manufactures recommendations and cultured sterilely in humidified atmosphere of 5% CO2 and 95% oxygen at 37°C. Cell were maintained for less than four passages, with monitoring of morphology and testing for mycoplasma.

7.2.2 Animal work

All animal work was approved by the Institutional Animal Care and Use Committee at the University of Virginia under protocol no. 4042 and was conducted in compliance with guidelines the Office of Laboratory Animal Welfare at the National Institutes of Health (United States). C57BL/6 mice ages 6–12 weeks (Jackson Laboratory, U.S.A.) were housed in a vivarium and given water and food ad libitum. Due to the prevalence of the breast cancer in women, only female mice were used in this study. For generation of tumors in vivo, $5 \cdot 10^5$ BRPKp110 cells were suspended in 100 µL PBS and injected orthotopically into the abdominal mammary fat pad. A control group of female C57Bl/6 mice of matched age received an injection of PBS. Tumor size was measured by calipers every 2–3 days after reaching a palpable size.

7.2.3 Generation of lymph node tissue slices

Lymph nodes were collected and sliced according to a previously established protocol.[5] Briefly, on the day of the experiment, animals were anesthetized with isoflurane followed by cervical dislocation. Inguinal and axillary lymph nodes were collected and placed in ice-cold PBS supplemented with 2% heat inactivated FBS. Subsequently, the lymph nodes were embedded in 6% low melting point agarose at 50°C and allowed to solidify. Agarose blocks containing the

lymph nodes were obtained using a 10 mm tissue punch. Slices with a thickness of 300 µm were obtained using a Leica VT1000S vibratome. Following sectioning, the slices were promptly transferred to complete RPMI medium and incubated for a minimum of 1 hour before use.

7.2.4 ELISA for analysis of cytokines and chemokines

Lymph node slices were cultured in complete RPMI media for 20 hr. Culture supernatant was collected and analyzed by sandwich ELISA assay using DuoSet ELISA development kit (R&D Systems, Inc., Minneapolis, MN, USA). ELISAs were for CCL21 (catalog no. DY457), CCL19 (DY440), CCL1 (DY845), CXCL12 (DY460) and CXCL13 (DY470) according to the manufacturer's protocol. In all cases, plates were developed using TMB substrate (Fisher Scientific), stopped with 1 M sulfuric acid (Fisher Scientific), and absorbance values were read at 450 nm on a plate reader (CLARIOstar; BMG LabTech, Cary, NC). To determine concentration of sample solutions, calibration curves were fit in GraphPad Prism 9 with a sigmoidal 4 parameter curve. Limit of detection (LOD) was calculated from the average of the blank + 3× standard deviation of the blank.

7.2.5 Immunostaining of live lymph node slices

Upon collection, the slices were allowed to rest for one hour before being labelled for live immunofluorescence following a previously established protocol.[6] Briefly, slices were Fc-blocked with an anti-mouse CD16/32 antibody (BioLegend, San Diego, CA) at a concentration of 25 µg/mL in 1x PBS with 2% heat-inactivated FBS (Gibco, Fisher Scientific) and incubated for 30 minutes in a humidified sterile incubator at 37 °C with 5% CO2. To stain, a 10 µL of antibody cocktail, containing antibodies at a concentration of 20 µg/mL, was added and the slices were

incubated for an additional hour. Following staining, slices were washed with PBS for 30 minutes at 37 °C, refreshing the PBS every 10-15 minutes.

7.2.6 Image acquisition

All imaging of LN tissues slices was performed on a Nikon A1Rsi confocal upright microscope, using 400, 487, 561, and 638 lasers with 450/50, 525/50, 600/50, and 685/70 GaAsp detectors. Images were collected with a 4x/ 0.20 and a 40x/ 0.45 NA Plan Apo NIR WD objective.

7.2.7 Image analysis

Images were analyzed in ImageJ (version 2.14.0/1.54g).[7] First, autofluorescent noise from the individual image channels was subtracted, defined as the mean fluorescent intensity ± 1 SD of respective fluorescent minus one (FMO) controls (n = 3 FMO control per experiment). The podoplanin signal was isolated, converted to grayscale, thresholded, and background subtracted. Small objects were removed, and the images were then converted to binary. A circle-fitting algorithm, Max Inscribed Circles,[8] was applied to identify the largest circle that could fit in the gaps without overlapping other circles. The distribution of circle radii was binned by 2 microns. Raw data were to determine differences in circles with a radius greater than 12 μm. Analyses were performed on images of the FRC network n= 9 mice per group. For representative image display, brightness and contrast were adjusted uniformly across all compared images unless otherwise specified.

7.3 Results

7.3.1 Stromal remodeling of primary TDLN at early stages of breast cancer occurs before LN organ expansion

Similar to human breast cancer carcinomas, in vivo inoculation of BRPKp110 cells into immunocompetent mice results in lymphovascular invasion into TDLNs, making it a suitable model for studying LN metastasis.[9] In this model, BRPKp110 cells were inoculated into the fourth abdominal mammary fat pad on each side of the animal, with the inguinal TDLN (iTDLN) and axillary TDLN (aTDLN) serving as the primary and secondary TDLNs, respectively.[10]

To understand physical remodeling of TDLN, we first assessed how the size of TDLN and FRC stromal network change with the progression of breast cancer. Fibroblastic reticular cells (FRCs) in LN construct a stromal network that serves as a scaffold for lymphocyte migration.[11] During inflammation, FRC stromal network expands to accommodate the influx of immune cells, which is associated with changes in fluid flow through the conduits and an upregulation of chemokines.[12–14] Stromal remodeling within TDLN is a key process that facilitates the dynamic adaptation of the local microenvironment and cellular functions to upstream tumor stimuli, thereby influencing the immune response and overall disease progression.[4]

While at day 5 post BRPKp110 inoculation no difference in LN size was detected between inguinal and auxiliary LNs of control and tumor-bearing mice (Figure 7C), there was a substantial increase in stromal gap size in iTDLN in comparison to aTDLN (Figures 7A, B, D).

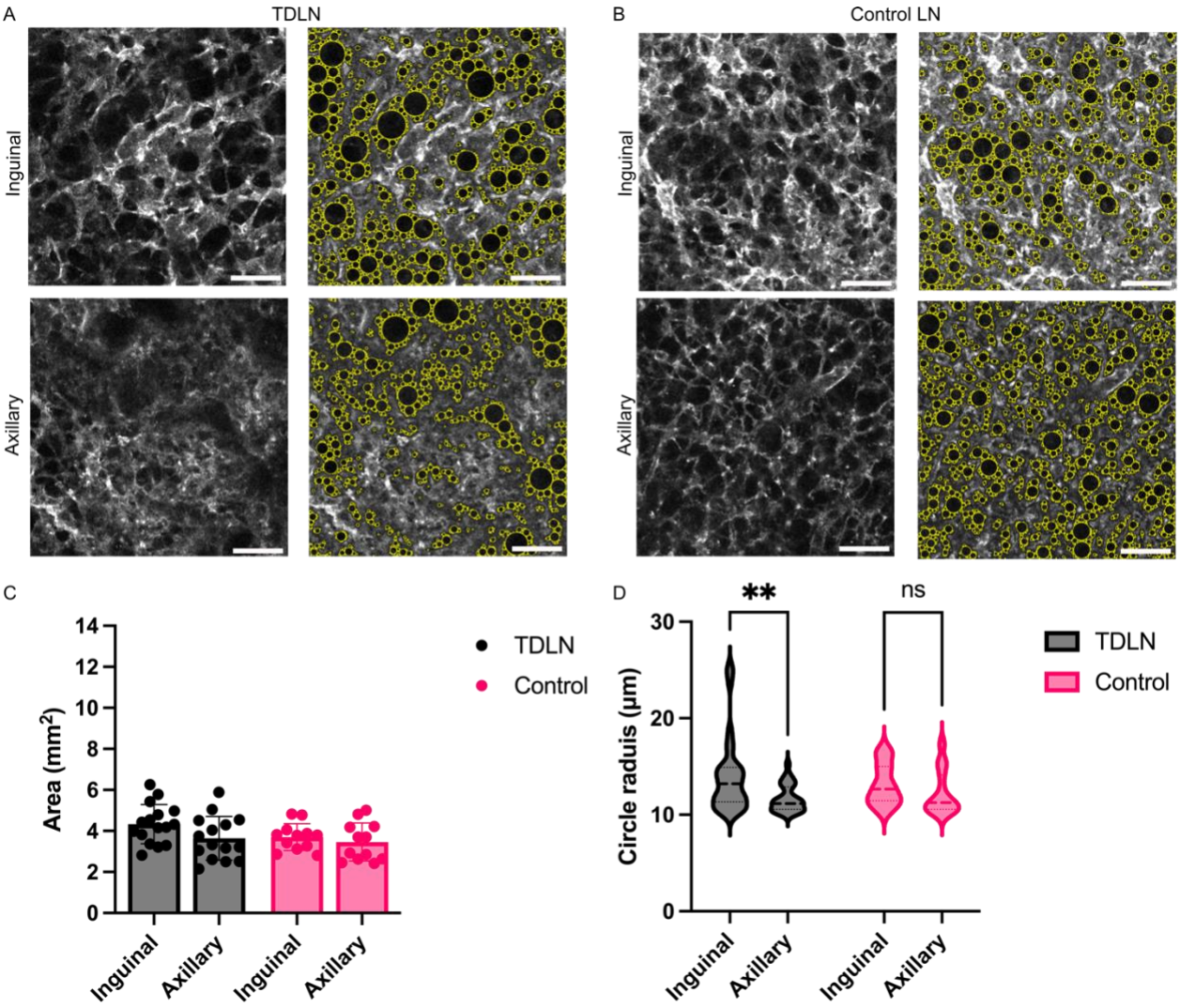

Figure 7.1: Stromal network size in TDLN at the early stage of BRPKp110 breast cancer. Enlarged FRC stromal gaps in primary TDLNs at early stage of breast cancer. Representative images of FRC stromal network in (A) inguinal and axillary TDLNs and (B) control LNs. LN slices stained with marker for fibroblast reticular cells (podoplanin; gray). Yellow circles indicate gaps the stromal network. Scale bar 20 μm. (C) Comparisons of LN whole organ area in control and tumor LNs. Mean ± standard deviation; each data point represents measurement from one LN (n = 11/per group, LN slices obtained from 6 mice). Area was compared using a two-way ANOVA, followed by Tukey posthoc test. ***p < 0.0001, **p < 0.01. (D) Comparisons of fitted circle radii in TDLN and Control LNs. (n = 3/per group, LN slices obtained from 9 mice). Circle radius was compared using a two-way ANOVA, followed by Tukey posthoc test. **p < 0.01.

These findings suggest that primary iTDLNs respond to the upstream breast tumor by remodeling the FRC network, although this remodeling does not impact the overall size of the TDLN at early stages of the disease.

7.3.2 FRC network remodeling of TDLN is persistent during advanced breast cancer stages

At the advanced stage of primary tumor development (day 18), there was a substantial increase in size in iTDLN in comparison to aTDLN, and control inguinal and axillary LNs, 5.1±3 ·106 μm2 vs 2.5±1 ·106 μm2, and 2.5±1 · 106 μm2, 2.1±1· 106 μm2, respectively (Figures 7.2A, D). Concurrently, stromal gaps in both iTDLN and aTDLN were significantly enlarged compared to those in control LNs (Figures 7.2 B, C, E). Together, these result indicate that the enlarged FRC stromal gaps observed at the early stage persist into advanced stages of disease, suggesting a sustained alteration in the TDLN immune environment.

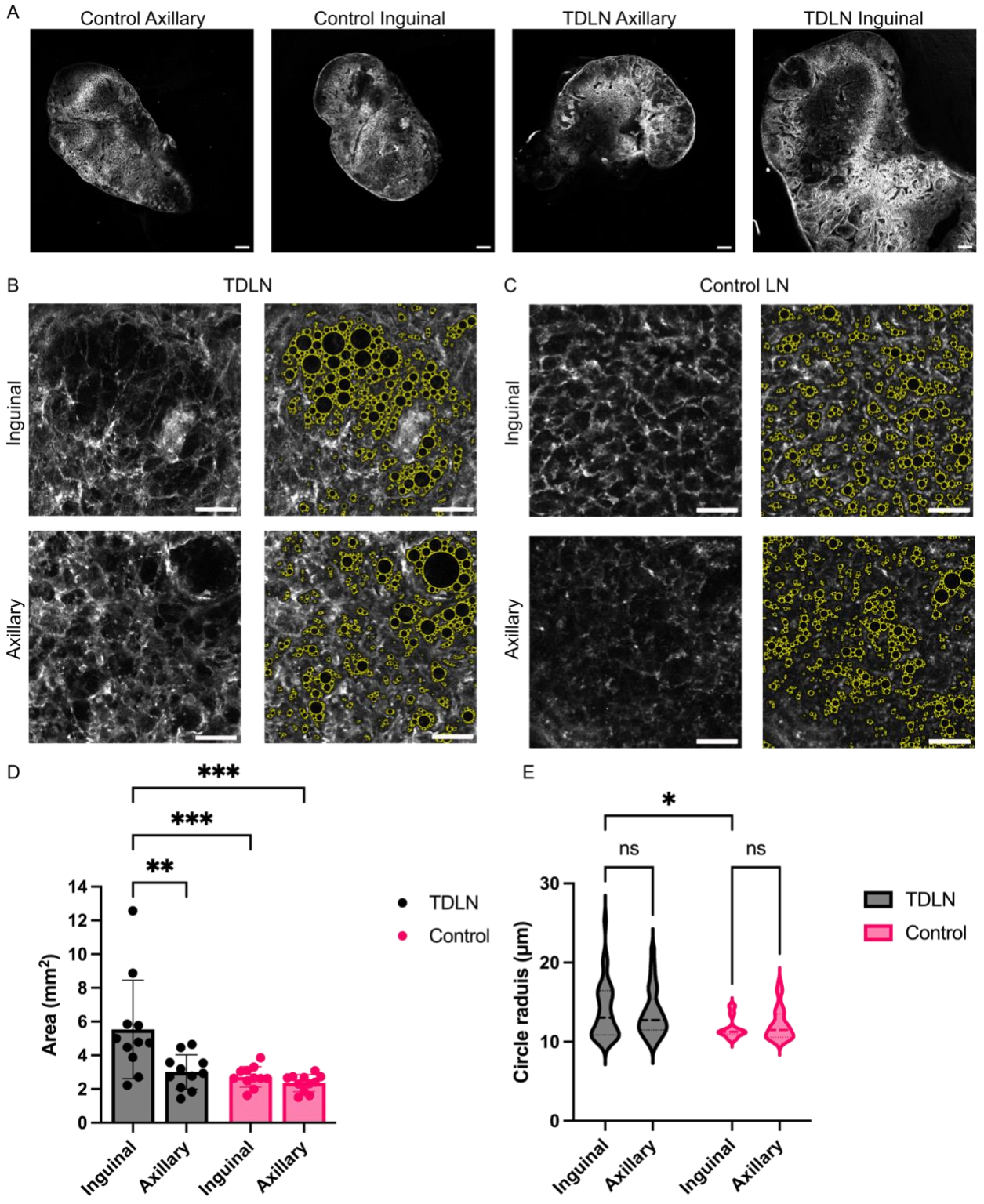

Figure 7.2: TDLNs undergo enlargement and expansion of FRC stromal gaps at advanced stage of breast cancer. (A) Representative images of axillary and inguinal LNs obtained from tumor-bearing and control mice after 18 days post inoculation. LN slices stained with marker for fibroblast reticular cells (podoplanin; gray). Scale bar 200 μm. Representative images of FRC

stromal network in (B) inguinal and axillary TDLNs and (C) control LNs. LN slices stained with marker for fibroblast reticular cells (podoplanin; gray). Yellow circles indicate gaps the stromal network. Scale bar 20 μm. (D) Comparisons of LN whole organ area in control and tumor LNs. Mean ± standard deviation; each data point represents measurement from one LN (n = 11/per group, LN slices obtained from 6 mice). Area was compared using a two-way ANOVA, followed by Tukey posthoc test. ***p < 0.0001, **p < 0.01. (E) Comparisons of fitted circle radii in TDLN and Control LNs. (n = 3/per group, LN slices obtained from 9 mice). Circle radius was compared using a two-way ANOVA, followed by Tukey posthoc test. *p < 0.05.

7.3.3 Temporal changes in chemokine secretion by TDLNs during advanced breast cancer progression

Having demonstrated in Chapter 6 that iTDLNs upregulate the secretion of CCL21 and CCL19 at early pre-metastatic stages of BRPKp110 breast cancer (day 5), we aimed to identify which chemokines are upregulated by TDLNs during advanced stages of breast cancer (days 18 and 26 post-tumor inoculation).

On day 18, iTDLNs secreted higher levels of CCL21 compared to aTDLNs and control LNs, and exhibited increased CXCL13 levels compared to control LNs (Figure 7.3). By day 26, when metastasis to aTDLNs and lungs is well established in this model of breast cancer,[10] levels of CCL21, CCL19 and CXCL13 were no longer upregulated and compare to those in aTDLNs and control LNs (Figure 7.3). Meanwhile, secretion of CCL1 remained below the level of detection at both tested time points, while CXCL12 levels were consistently comparable across all tested groups at both time points.

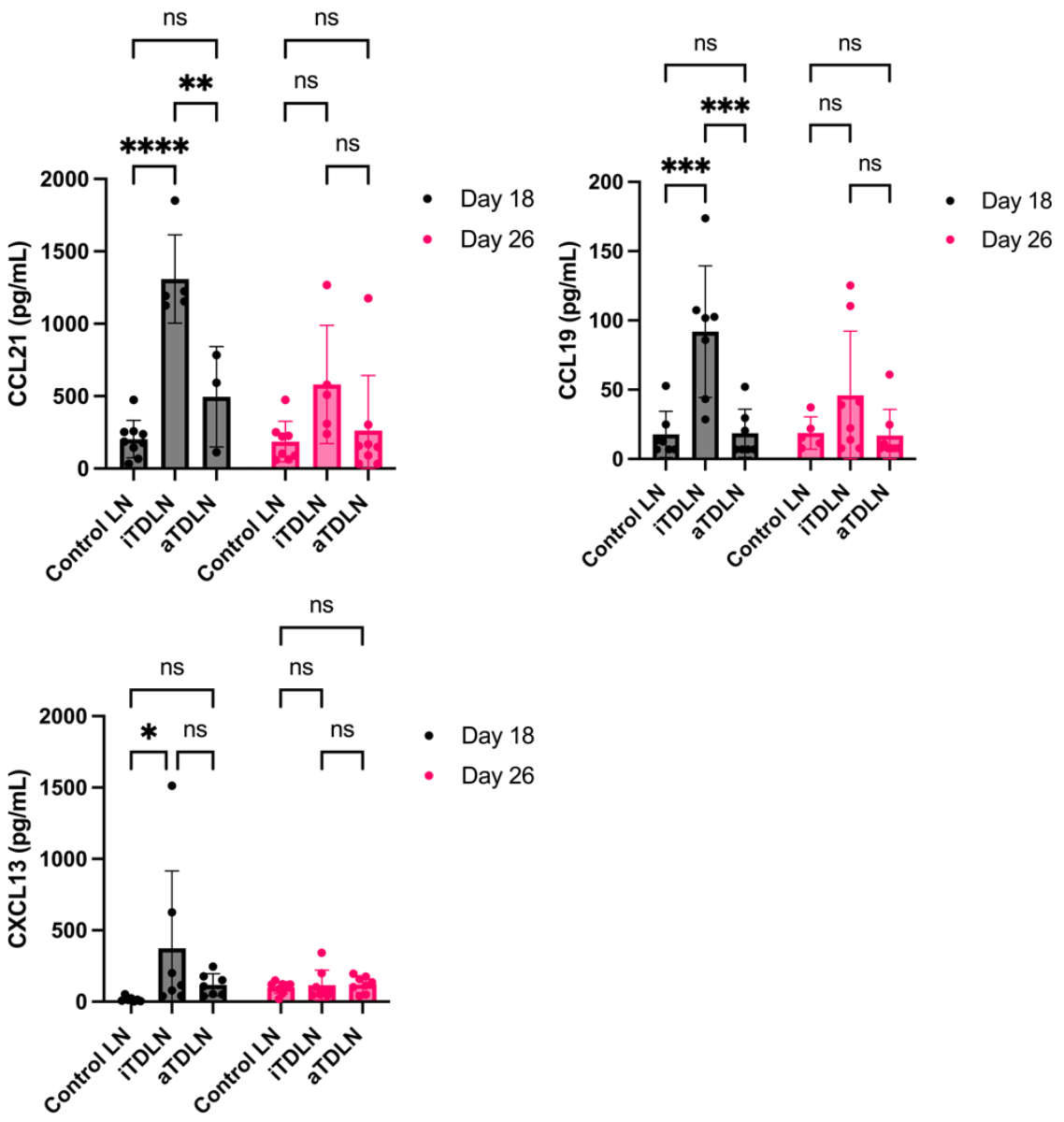

Figure 7.3: Concentrations of chemokine levels in control LN and TDLNs at tumor day 18 and day 26. Concentrations of CCL21, CCL19 and CXCL13 chemokines were measured in conditioned media obtained from control LN, iTDLN and aTDLN following a 20 hr culture period. Mean ± standard deviation; each data point corresponds to the supernatant collected from an individual LN slice (n = 2-3/per group, LN slices obtained from 3 mice). Concentration was compared using a two-way ANOVA, followed by Tukey posthoc test. ****$p < 0.0001$, ***$p < 0.001$, **$p < 0.01$, *$p < 0.05$.

In conclusion, these data demonstrate that the levels of secreted lymphocyte-homing CCL21, CCL19, and CXCL13 chemokines were significantly upregulated in the iTDLN during the stage when primary tumors were well established. This suggests an active role of these chemokines in the immune response to the primary tumor. However, as the disease progressed to the metastatic stage, the secretion levels of these chemokines decreased to baseline levels. This downregulation at the metastatic stage indicates a potential shift in the immune environment, which may contribute to the establishment and progression of metastases.

7.4 Discussion

The progression of breast cancer is intricately linked to the dynamic changes within TDLNs. Using the BRPKp110 breast cancer model we demonstrated dynamic nature of TDLN physical and biochemical remodeling. The remodeling of FRC stromal network may resulted in disruption of size exclusion properties of stromal conduits that facilitate invasion of tumor cell into TDLNs. Furthermore, the upregulation of multiple chemotactic stimuli at both early and advanced stages of primary tumor growth may affect the expression of cognate receptors on primary tumor cells, recruiting them to the TDLNs.

7.5 Conclusions and future work

While it is established that upon vaccination, activated dendritic cells enter the LN and the interaction between the protein CLEC2 on dendritic cells and podoplanin on FRCs induces stromal relaxation and LN enlargement,[15,16] the mechanism behind the enlargement of FRC stromal gaps in TDLNs remains unknown. Future research will test the role of CLEC2-expressing migratory dendritic cells in podoplanin-induced FRC relaxation.

Furthermore, future research will investigate how changes in the FRC network and chemokine gradients within TDLNs influence the trafficking and function of immune cells. This research could reveal potential therapeutic targets to modulate the immune microenvironment and inhibit metastatic spread.

7.6 References

(1) Du Bois, H.; Heim, T. A.; Lund, A. W. Tumor-Draining Lymph Nodes: At the Crossroads of Metastasis and Immunity. *Sci. Immunol.* **2021**, *6* (63), eabg3551. https://doi.org/10.1126/sciimmunol.abg3551.

(2) Qian, C.-N.; Berghuis, B.; Tsarfaty, G.; Bruch, M.; Kort, E. J.; Ditlev, J.; Tsarfaty, I.; Hudson, E.; Jackson, D. G.; Petillo, D.; Chen, J.; Resau, J. H.; Teh, B. T. Preparing the "Soil": The Primary Tumor Induces Vasculature Reorganization in the Sentinel Lymph Node before the Arrival of Metastatic Cancer Cells. *Cancer Res.* **2006**, *66* (21), 10365–10376. https://doi.org/10.1158/0008-5472.CAN-06-2977.

(3) Pereira, E. R.; Jones, D.; Jung, K.; Padera, T. P. The Lymph Node Microenvironment and Its Role in the Progression of Metastatic Cancer. *Semin. Cell Dev. Biol.* **2015**, *38*, 98–105. https://doi.org/10.1016/j.semcdb.2015.01.008.

(4) Riedel, A.; Shorthouse, D.; Haas, L.; Hall, B. A.; Shields, J. Tumor-Induced Stromal Reprogramming Drives Lymph Node Transformation. *Nat. Immunol.* **2016**, *17* (9), 1118–1127. https://doi.org/10.1038/ni.3492.

(5) Belanger, M. C.; Ball, A. G.; Catterton, M. A.; Kinman, A. W. L.; Anbaei, P.; Groff, B. D.; Melchor, S. J.; Lukens, J. R.; Ross, A. E.; Pompano, R. R. Acute Lymph Node Slices Are

a Functional Model System to Study Immunity Ex Vivo. *ACS Pharmacol. Transl. Sci.* **2021**, *4* (1), 128–142. https://doi.org/10.1021/acsptsci.0c00143.

(6) Groff, B. D.; Kinman, A. W. L.; Woodroof, J. F.; Pompano, R. R. Immunofluorescence Staining of Live Lymph Node Tissue Slices. *J. Immunol. Methods* **2019**, *464*, 119–125. https://doi.org/10.1016/j.jim.2018.10.010.

(7) Schindelin, J.; Arganda-Carreras, I.; Frise, E.; Kaynig, V.; Longair, M.; Pietzsch, T.; Preibisch, S.; Rueden, C.; Saalfeld, S.; Schmid, B.; Tinevez, J.-Y.; White, D. J.; Hartenstein, V.; Eliceiri, K.; Tomancak, P.; Cardona, A. Fiji: An Open-Source Platform for Biological-Image Analysis. *Nat. Methods* **2012**, *9* (7), 676–682. https://doi.org/10.1038/nmeth.2019.

(8) Wershof, E.; Park, D.; Barry, D. J.; Jenkins, R. P.; Rullan, A.; Wilkins, A.; Schlegelmilch, K.; Roxanis, I.; Anderson, K. I.; Bates, P. A.; Sahai, E. A FIJI Macro for Quantifying Pattern in Extracellular Matrix. *Life Sci. Alliance* **2021**, *4* (3), e202000880. https://doi.org/10.26508/lsa.202000880.

(9) Rutkowski, M. R.; Allegrezza, M. J.; Svoronos, N.; Tesone, A. J.; Stephen, T. L.; Perales-Puchalt, A.; Nguyen, J.; Zhang, P. J.; Fiering, S. N.; Tchou, J.; Conejo-Garcia, J. R. Initiation of Metastatic Breast Carcinoma by Targeting of the Ductal Epithelium with Adenovirus-Cre: A Novel Transgenic Mouse Model of Breast Cancer. *J. Vis. Exp.* **2014**, No. 85, 51171. https://doi.org/10.3791/51171.

(10) Buchta Rosean, C.; Bostic, R. R.; Ferey, J. C. M.; Feng, T.-Y.; Azar, F. N.; Tung, K. S.; Dozmorov, M. G.; Smirnova, E.; Bos, P. D.; Rutkowski, M. R. Preexisting Commensal Dysbiosis Is a Host-Intrinsic Regulator of Tissue Inflammation and Tumor Cell

Dissemination in Hormone Receptor–Positive Breast Cancer. *Cancer Res.* **2019**, *79* (14), 3662–3675. https://doi.org/10.1158/0008-5472.CAN-18-3464.

(11) Katakai, T.; Hara, T.; Sugai, M.; Gonda, H.; Shimizu, A. Lymph Node Fibroblastic Reticular Cells Construct the Stromal Reticulum via Contact with Lymphocytes. *J. Exp. Med.* **2004**, *200* (6), 783–795. https://doi.org/10.1084/jem.20040254.

(12) Martinez, V. G.; Pankova, V.; Krasny, L.; Singh, T.; Makris, S.; White, I. J.; Benjamin, A. C.; Dertschnig, S.; Horsnell, H. L.; Kriston-Vizi, J.; Burden, J. J.; Huang, P. H.; Tape, C. J.; Acton, S. E. Fibroblastic Reticular Cells Control Conduit Matrix Deposition during Lymph Node Expansion. *Cell Rep.* **2019**, *29* (9), 2810-2822.e5. https://doi.org/10.1016/j.celrep.2019.10.103.

(13) Lütge, M.; Pikor, N. B.; Ludewig, B. Differentiation and Activation of Fibroblastic Reticular Cells. *Immunol. Rev.* **2021**, *302* (1), 32–46. https://doi.org/10.1111/imr.12981.

(14) Pikor, N. B.; Cheng, H.-W.; Onder, L.; Ludewig, B. Development and Immunological Function of Lymph Node Stromal Cells. *J. Immunol.* **2021**, *206* (2), 257–263. https://doi.org/10.4049/jimmunol.2000914.

(15) Acton, S. E.; Astarita, J. L.; Malhotra, D.; Lukacs-Kornek, V.; Franz, B.; Hess, P. R.; Jakus, Z.; Kuligowski, M.; Fletcher, A. L.; Elpek, K. G.; Bellemare-Pelletier, A.; Sceats, L.; Reynoso, E. D.; Gonzalez, S. F.; Graham, D. B.; Chang, J.; Peters, A.; Woodruff, M.; Kim, Y.-A.; Swat, W.; Morita, T.; Kuchroo, V.; Carroll, M. C.; Kahn, M. L.; Wucherpfennig, K. W.; Turley, S. J. Podoplanin-Rich Stromal Networks Induce Dendritic Cell Motility via

Activation of the C-Type Lectin Receptor CLEC-2. *Immunity* **2012**, *37* (2), 276–289. https://doi.org/10.1016/j.immuni.2012.05.022.

(16) Acton, S. E.; Farrugia, A. J.; Astarita, J. L.; Mourão-Sá, D.; Jenkins, R. P.; Nye, E.; Hooper, S.; Van Blijswijk, J.; Rogers, N. C.; Snelgrove, K. J.; Rosewell, I.; Moita, L. F.; Stamp, G.; Turley, S. J.; Sahai, E.; Reis E Sousa, C. Dendritic Cells Control Fibroblastic Reticular Network Tension and Lymph Node Expansion. *Nature* **2014**, *514* (7523), 498–502. https://doi.org/10.1038/nature13814.

8 Conclusions and future directions

In conclusion, this work utilized live LN tissue slices to model cancer cell spread within the complex LN microenvironment ex vivo. We demonstrated the application of this model to quantify the capacity of cancer cells to invade distinct regions of the LN in the absence of lymphatic barriers. Moreover, we developed an image analysis methodology to quantify the spatial invasion of cancer cells within live LN slices, utilizing live immunofluorescence staining coupled with confocal imaging. This methodology enabled us to examine the dynamics of cancer cell invasion relative to both the anatomical zones of the LN and domains rich in immobilized chemokines. Our novel model predicted a dynamic invasion of cancer cells, with an initial preferential accumulation in the SCS, followed by subsequent spread to the cortex and B-cell follicles. Furthermore, we tested the hypothesis that the chemotactic activity in live LN slices could serve as a model for the chemotactic migration of cancer cells. We identified that the preferential invasion of cancer cells correlated with the distribution of immobilized CXCL13 and CCL1 chemokine-rich domains within the LN. Additionally, through CRISPR/Cas9 technology, we elucidated the importance of CXCR5 receptor in guiding cancer cell invasion suing both 3D transwell assay and ex vivo overlay onto live LN tissue. Our results indicate that while the CXCR5 receptor facilitates the migration of cancer cells toward molecules produced by naïve LN, blocking CXCR5-mediated signaling is not sufficient to halt cancer cell invasion in regions positive for matrix-bound CXCL13. Rather, a combination of chemokine signaling pathways simultaneously influences cancer cell invasion in specific areas. Finally, we applied this system to model invasion into pre-metastatic TDLNs, addressing whether pre-metastatic nodes are more permissive or resistant to cancer cell invasion. In line with other models of breast cancer, our novel model predicted a lower invasion potential of cancer cells into pre-metastatic iTDLNs, which correlated with elevated intranodal IL-21.

While we demonstrated that live LN slices effectively support the invasion of cancer cells for up to 20 hours of culture, the short duration remains a limitation. A 20-hr interaction may not fully capture the long-term interactions between cancer cells and LN microenvironment at progressive stages of cancer invasion. Future studies will aim to extend the culture duration. Additionally, while to our knowledge this model is the first to enable the spread of cancer cells within the cellular and anatomical complexity of the LN microenvironment ex vivo, in its current state it lacks the functionality of the migratory cellular compartment. Further studies are needed to enable incorporation of migratory cells populations to address this limitation.

Overall, this innovative ex vivo model of cancer cell spread in live LNs enables a time-course analysis of cancer-immune interactions within the intricate tissue microenvironment. It enhances experimental accessibility and supports parallel read-outs, allowing for the simultaneous assessment of cancer cells and live tissue. Furthermore, the model set up allows for the manipulation of cancer cells in isolation, providing a controlled setting to test specific interactions. This novel model lays a foundation for future research into the interplay between the microenvironmental cues of TDLN and their influence on cancer cell invasion.

8.1 Evaluating immune cell killing potency of TDLN

Future research will aim to understand the mechanisms behind the reduced invasion into pre-metastatic TDLNs. Specifically, we will focus on the extent to which live TDLNs can induce cancer cell damage or death through immune cell-mediated killing and cytokine secretion.

If successful, live TDLNs slices that effectively mimic the microenvironmental cues and effector cell activity can serve as a valuable tool for evaluating TDLN priming and the cytotoxic

effects of anti-cancer treatments. Existing cytotoxicity assays are limited by their narrow focus on single-effector, single-target, or single-antigen scenarios, which do not adequately mimic the complex in vivo microenvironments. While advanced assays like antigen stress tests provide more detailed analysis through repeated antigen stimulation, they still require further development to accurately replicate in vivo conditions and account for factors such as T-cell exhaustion.[1] Additionally, the state of effector cell function does not always directly correlate with target cell death.[2] Thus, a combined analysis of both, effector cells function and direct analysis of target cell lysis, can offer valuable insights into mechanisms of anti-tumor cytotoxicity. In contrast, the setup of this novel ex vivo model allows for a combined analysis of both, effector cells function and direct analysis of cancer cell lysis, while preserving the innate microenvironment of the TDLN.

8.2 Testing immunotherapy effects on cancer cell invasiveness

TDLNs are key sites where the immune system first encounters tumor antigens, and the presence of anti-tumor immunity in these nodes can indicate active immune response to the tumor.[3] The remodeling of TDLN tissue microenvironments suggests a crosstalk between the primary tumor and TDLN that is dependent on the disease stage.[4] Consequently, the microenvironment of TDLN can either facilitate metastasis or hinder immune surveillance and the elimination of cancer cells.[5–8] Understanding the factors in TDLNs that contribute to the switch to a tumor-tolerant immune state during disease progression can provide insights into mechanisms of LN metastasis. Our novel approach for modeling cancer cell spread in live LN tissues can be applied to the TDLNs collected at various stages of tumor progression, enabling an analysis of cancer cell invasiveness as a function of the TDLN state (Figure X). Future work will expand the application of this model

to TDLNs obtained at advanced disease stages, quantifying the invasive potential of cancer cells while simultaneously assessing changes in immune status.

8.3 Investigating selective infiltration of cancer cells

Lastly, when seeding cancer cells onto live LN slices, only a fraction of the cells infiltrates the tissue. A detailed comparison of differentially expressed and coregulated genes between non-infiltrated and infiltrated cancer cells can further refine the biological characterization of invasive cancer cells. Although primary tumors changes in response to the environment, state of cancer cells in culture may not resemble the state of metastatic cells that reach TDLNs in vivo. However, due to the approachability of the LN slice ex vivo system, this limitation can be addressed by overlaying cells sourced from the primary tumor to its respective TDLNs. Exploring the molecular mechanisms driving this selective infiltration may uncover new targets for therapeutic intervention.

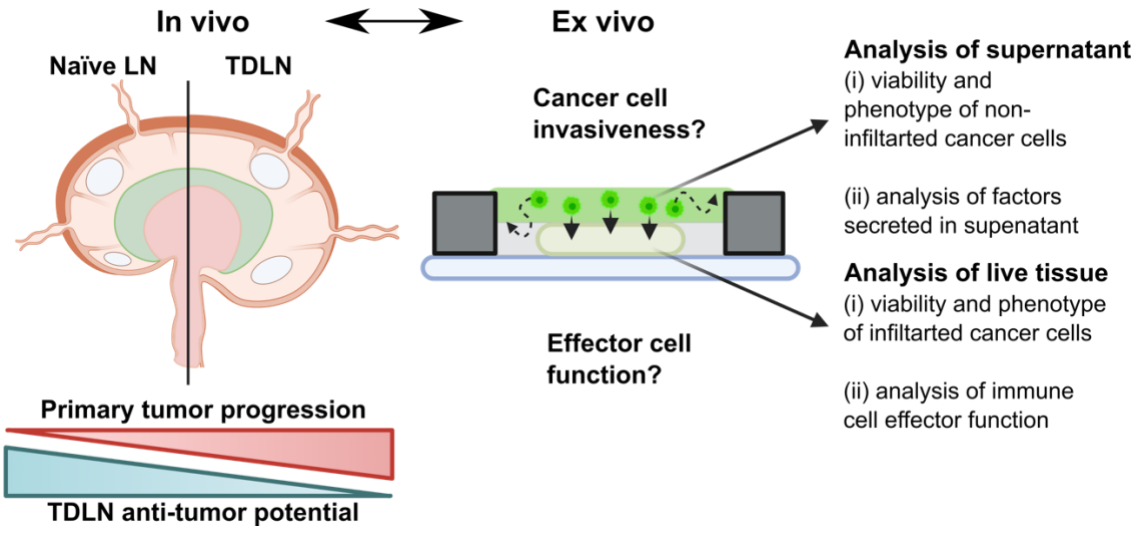

Figure 8.1: Future application of ex vivo model of cancer cell spread in live LN tissue. Ex vivo model of cancer cell spread in live LN slices provides a platform to investigate mechanisms of cancer invasion within the intricate tissue microenvironment, supporting time-course analysis and

parallel read-outs. We anticipate that this system will enable further research into cancer-immune interactions and allow to isolate specific factors that make TDLNs resistant to cancer cell invasion, which are challenging to dissect in vivo.

8.4 References

(1) Kiesgen, S.; Messinger, J. C.; Chintala, N. K.; Tano, Z.; Adusumilli, P. S. Comparative Analysis of Assays to Measure CAR T-Cell-Mediated Cytotoxicity. *Nat. Protoc.* **2021**, *16* (3), 1331–1342. https://doi.org/10.1038/s41596-020-00467-0.

(2) Waldman, A. D.; Fritz, J. M.; Lenardo, M. J. A Guide to Cancer Immunotherapy: From T Cell Basic Science to Clinical Practice. *Nat. Rev. Immunol.* **2020**, *20* (11), 651–668. https://doi.org/10.1038/s41577-020-0306-5.

(3) Louie, D. A. P.; Oo, D.; Leung, G.; Lin, Y.; Stephens, M.; Alrashed, O.; Tso, M.; Liao, S. Tumor-Draining Lymph Node Reconstruction Promotes B Cell Activation During E0771 Mouse Breast Cancer Growth. *Front. Pharmacol.* **2022**, *13*, 825287. https://doi.org/10.3389/fphar.2022.825287.

(4) O'Melia, M. J.; Manspeaker, M. P.; Thomas, S. N. Tumor-Draining Lymph Nodes Are Survival Niches That Support T Cell Priming against Lymphatic Transported Tumor Antigen and Effects of Immune Checkpoint Blockade in TNBC. *Cancer Immunol. Immunother.* **2021**, *70* (8), 2179–2195. https://doi.org/10.1007/s00262-020-02792-5.

(5) Lee, E.; Pandey, N. B.; Popel, A. S. Pre-Treatment of Mice with Tumor-Conditioned Media Accelerates Metastasis to Lymph Nodes and Lungs: A New Spontaneous Breast Cancer Metastasis Model. *Clin. Exp. Metastasis* **2014**, *31* (1), 67–79. https://doi.org/10.1007/s10585-013-9610-9.

(6) Mao, X.; Tang, X.; Pan, H.; Yu, M.; Ji, S.; Qiu, W.; Che, N.; Zhang, K.; Huang, Z.; Jiang, Y.; Wang, J.; Zhong, Z.; Wang, J.; Liu, M.; Chen, M.; Zhou, W.; Wang, S. B Cells and IL-21-Producing Follicular Helper T Cells Cooperate to Determine the Dynamic Alterations of Premetastatic Tumor Draining Lymph Nodes of Breast Cancer. *Research* **2024**, *7*, 0346. https://doi.org/10.34133/research.0346.

(7) Wang, Y.; Zhu, T.; Shi, Q.; Zhu, G.; Zhu, S.; Hou, F. Tumor-Draining Lymph Nodes: Opportunities, Challenges, and Future Directions in Colorectal Cancer Immunotherapy. *J. Immunother. Cancer* **2024**, *12* (1), e008026. https://doi.org/10.1136/jitc-2023-008026.

(8) Fransen, M. F.; Van Hall, T.; Ossendorp, F. Immune Checkpoint Therapy: Tumor Draining Lymph Nodes in the Spotlights. *Int. J. Mol. Sci.* **2021**, *22* (17), 9401. https://doi.org/10.3390/ijms22179401.

Contributed Protocols

1. Cancer cell labeling with fluorescent dyes.

Materials:

- Cell tracing reagents (Tab.1)
- DMSO
- PBS
- Culture medium (containing at least 1% serum)
- 15 mL tube

Fluorescent cell tracing reagents listed in Table 1 were tested for labeling of BRPKp110 cancer cells. The protocol outlined below yielded viable cells capable of migration and spread in Live for a duration of 20h.

1. Prepare stock solution immediately prior to use to obtain 5 mM stock solution. by adding the appropriate volume of DMSO (see vendor instructions) and mixing well.
2. Obtain $1 \cdot 10^6 /\mathrm{mL}$ cancer cell suspension in PBS.
3. For 1mL of cell suspension add 1µL of staining solution (1:1000 dilution).
4. Incubate the cells at 37°C for 20 min, protected from light.
5. To remove excess of dye, add 5mL of culture medium (containing at least 1% serum) to the cells and incubate at 37°C for 5 min.
6. Pellet the cells by centrifugation at 400X for 5 min and resuspend them in 5 mL of pre-warmed complete culture medium.
7. Incubate the cells at 37° C for least 10 min before use to allow the CellTrace™ reagent to undergo acetate hydrolysis.

Product information	Cell Trace Violet	Cell Trace CSFE	NHS-Rhodamine
Vendor, catalog number	Thermo Scientific™ C34557	Thermo Scientific™ C34554	Thermo Scientific™ 46406
Excitation/Emission (nm)	405/450	492/517nm	552/575
Working concentration	5 µM	5 µM	5 µM

Table 0.1: Product information, spectral detail and working concentration.

2. Cancer cell overlay onto live LN slices.

Materials:

- Non-treated 6 well plate
- Low melting point agarose
- Parafilm
- Washers
- Complete culture media
- PBS with 2% serum

1. Preparation of live LN slices (detailed protocol for obtaining live LN slices is available elsewhere).

   Briefly, harvest inguinal, brachial and axillary LNs from the mouse and immediately place them ice-cold PBS supplemented with 2% heat inactivated FBS to maintain tissue integrity until embedding into agarose gel. Subsequently, embed LNs in a petri dish filled with 6% low melting point agarose at 50°C and place the dish on ice until agarose is solidified (5 min). Use a cylindrical 10 mm tissue punch to obtain agarose blocks with LNs. Slice obtained agarose blocks to a thickness of 300 µm using a Leica VT1000S vibratome. Note, that top and bottom LN slices do not contain a 300 µm of LN tissue and therefore are not

suitable for the overlays. Collect LN slices into a 6-well plate filled with pre-warmed complete media. Following sectioning, incubate at 37°C for at least 1 h before use to allow tissue recovery.

2. Label cancer cells with fluorescent cell tracing reagents (detailed protocol is available above)
3. After LN slices have been incubated at 37°C for least 1 h and cancer cell have been stained with fluorescent cell tracer, overlay cancer cell on top of live LN slices:
    i. Prepare necessary number of washers: place washers into a petri dish containing 70% ethanol for at least 5 min, then replace washers into a petri dish filled with PBS.
    ii. Reconstitute $1 \cdot 10^6$ fluorescently labeled cancer cells in 1mL pre-warmed complete culture media. Mix well by pipetting up and down.
    iii. Cover the lid of a 6-well plate with a parafilm.
    iv. Using a brush, carefully place the LN slices on the parafilm.
    v. Using a non-sharp tweezers place a washer on top of each LN slice.
    vi. Pipette 20 µL of cancer cell suspension inside the washer encircling each LN slice.
    vii. Cover the plate and incubate at 37°C for 1 h.
    viii. Following a 1h of incubation, carefully remove washers using non-sharp tweezers, then carefully place the LN slices into the well-plate filled with 500 µL pre-warmed complete culture media per well. Ensure that orientation of the LN slice remain unchanged (same side up as for cancer cell overlay).
    ix. Incubate for 10 min at 37°C.

x. Aspirate media. Add 500 µL of pre-warmed complete culture media per well. Incubate for 10 min at 37°C. Repeat wash step with pre-warmed complete media twice (a total duration of 30 min).

4. Stain slices using life immunofluorescent protocol (detailed protocol is available elsewhere). Consider whether antibodies used for immunostaining may have neutralizing or stimulating effect (e.g. anti-CCL21 and other chemokine antibodies; anti-CD3, etc.) Note that if antibodies used for immunostaining do not have a neutralizing/stimulating effect, step 4: Immunofluorescent staining can be performed before step 3: Cancer cell overlay.

   Briefly, prepare Fc block (anti-CD16/32) in PBS with 2% serum at working concentration of 25 µg/mL. Avoiding changing the orientation of the LN slices, use brush to carefully place onto parafilm. Clean washers in 70% ethanol and PBS. Using non-sharp tweezers place a washer on top of each LN slice. Add 20 µL of a blocking solution into the washer encircling each slice. Cover the plate and incubate the LN slices for 20-30 min at 37°C.

   Prepare an antibody cocktail at a concentration of 20 µg/mL for each antibody in PBS with 2% serum. Add 10 µL of the antibody cocktail directly into the washer containing the blocking solution on each slice. Mix gently by pipetting up and down, taking care not to disrupt the slice. Keep the plate covered to protect from light and prevent photobleaching. Incubate the LN slices for 60 min at 37°C. Remove the washers and rinse the slices by adding 1mL of PBS with 2% serum to each well. Incubate for 10 min at 37°C, aspirate, repeat washing step three times (a total of 30 min, replacing the solution every 10 min). Transfer LN slices to a well plate containing a 500 µL of pre-warmed complete culture media for immediate imaging, or culture.

3. Ki-67 staining of LN slices.

Materials:

- Ice-cold 70% ethanol
- Fc block purified anti-mouse CD16/32, clone 93, Rat IgG2a, κ, BioLegend, cat# 101302
- Alexa Fluor 647 anti-mouse Ki-67 antibody, clone 16A8, Isotype Rat IgG2a, κ, BioLegend, cat# 652407
- DAPI Invitrogen cat# D1306 concentration 5 mg/mL
- Wash buffer (PBS with 2% FBS)

1. Add 3 mL of ice-cold 70% ethanol dropwise into the well with LN slice.
2. Incubate at -20°C for at least 2 hours. These fixed samples can be stored at -20°C for up to a week prior to staining.
3. Wash twice with 5 ml of wash buffer.
4. Place slices onto the parafilm.
5. Prepare washers:
    i. Incubate washers in -70 ethanol at room temperature for at least 20 min prior to use.
    ii. Rinse washers in PBS.
    iii. Using a non-sharp tweezers place a washer on top of each LN slice.
6. Prepare Fc block (anti-CD16/32) in PBS with 2% serum at working concentration of 25 µg/mL. Add 20 µL of Fc blocking solution into the washer encircling each slice. Incubate at RT for 20-30 min.

7. Prepare Ki-67 antibody in PBS with 2% serum at working concentration of 25 µg/mL. Add 10 µl of antibody solution into the washer encircling each slice. Incubate at RT for 90-120 min protected from light.
8. Remove the washers and carefully place LN slices into the wells without changing the orientation of the slices.
9. Rinse the slices by adding 1mL of ice-cold PBS.
10. Incubate for 10 min at RT, aspirate, repeat washing step three times (a total of 30 min, replacing the solution every 10 min).
11. Transfer LN slices to a well plate containing a 500 µL of PBS for imaging.

4. Cancer cell monolayer surface staining for chemokine receptors

Materials:

- Confluent monolayer of cancer cells (6-well plate)
- Formalin 1:10 dilution (buffered) FisherBrand cat# 23-245684
- PBS with 2% FBS
- Fc block purified anti-mouse CD16/32, clone 93, Rat IgG2a, κ, BioLegend, cat# 101302
- Antibodies for chemokine receptors:
    i. anti-mouse APC CD197 (CCR7) clone 4B12, Rat IgG2a, κ, BioLegend, cat# 120107
    ii. anti-mouse APC CD198 (CCR8) clone SA214G2, Rat IgG2b, κ, BioLegend, cat# 150309
    iii. anti-mouse APC CD184 (CXCR4) clone L276F12, Rat IgG2b, κ, BioLegend, cat# 146507

iv. anti-mouse APC CD185 (CXCR5) clone L138D7, Rat IgG2b, κ, BioLegend, cat#145505

v. Isotype Control APC RatIgG2a, clone RTK2758, Rat IgG2a, κ, BioLegend, cat# 400511

vi. Isotype Control APC Rat IgG2b, κ, clone RTK4530, BioLegend, cat# 400611

1. Aspirate media from cancer cells and rinse wells with PBS.
2. Add 1mL of formalin solution per well. Fix cells at RT for 30 min with gentle agitation.
3. Aspirate formalin solution and rinse with PBS with 2% FBS.
4. Prepare Fc block (anti-CD16/32) in PBS with 2% serum at working concentration of 25 µg/mL. Add 100 µL of Fc blocking solution per well. Incubate at RT for 20-30 min with gentle agitation.
5. Prepare antibody staining solution (or antibody isotope control) in PBS with 2% serum at working concentration of 25 µg/mL. Add 100 µl of antibody solution per well. Incubate at RT for 60 min with gentle agitation. Keep protected from light.
6. Rinse by adding 1mL of PBS. Incubate for 10 min at RT, aspirate, repeat twice.

5. Cancer cell pre-treatment with Pertussis toxin.

Materials:

- 30% bleach solution
- Pertussis toxin, 50 µg, TOCRIS cat# 3097
- Cancer cell culture at low confluence (30-50%)

1. Reconstitute Pertussis toxin to 0.1 µg/µl in 500 µl of sterile distilled water.
2. Add Pertussis toxin to complete media to final concentration of 100 ng/mL.
3. Replace media in cancer cell culture with media supplied with Pertussis toxin.
4. Incubate cancer cell at 37C for 16h.
5. After 16h, aspirate media containing Pertussis toxin from cancer cell culture to a tube containing 30% bleach solution.
6. Rinse cell in PBS with 2% serum. Aspirate to a tube containing 30% bleach solution.
7. Repeat twice.

6. 3D Transwell migration protocol.

Materials:

- Transwell membranes Milicell Standing Cell Culture Inserts cat# PI8P01250, pore size 8 µm, diameter 12 mm
- Non-treated 12 well plates
- Collagen Ibidi cat#50201 concentration 5 mg/mL
- Fibrinogen 6 mg/mL (BD Biosciences)
- 10X PBS: 20 µL
- 1M NaOH: 6 µL
- ddH2O: 49 µL
- NaHCO3
- 10% Formalin Solution
- DAPI Invitrogen cat# D1306 concentration 5 mg/mL
- Ice-cold PBS
- Inverted microscope for image acquisition

Preparation of cells:

1. Place cell culture inserts into non-treated 12 well plate.
2. Determine volume needed for 100,000 cancer cells / 100µL gel per transwell. Account for pipetting errors, make extra.
3. Obtain cell suspension by removing cells from the flask using trypsin solution.
4. Spin down to obtain a cell pellet with the required number of cells.
5. Preparation of Collagen I gel at 2 mg/mL. Place gel reagents on ice for 20 min.

   For 300 ul of collagen gel pipet all ingredients in the order listed

   i. 10X PBS: 20 µL
   ii. 1M NaOH: 6 µL
   iii. ddH2O: 49 µL
   iv. NaHCO3 7.5%: 5 µL
   v. Media: 50 µL
   vi. Collagen I 5 mg/mL: 120 µL
   vii. Fibrinogen: 50 µL (Suspend the cell pellet in the fibrinogen)
   viii. Mix well by pipetting, keeping the tube on ice.
6. Add 100 µL of gel-cell suspension to each transwell. Gently tap plate to ensure coverage.
7. Place the plate with the inserts in the incubator at 37C for 30 min for gelation.
8. Once the gel has set, slowly pipette 700 µL of media (or chemoattractant) into the well around the insert.
9. Add 100 µL of media on top of the gel.
10. Lift and set down the inserts to ensure there are no air bubbles.
11. Return the plate to the incubator and culture for 18-20 hours.

12. Once culture time has passed, carefully remove the gel with a Q tip.
13. Aspirate the media from the wells.
14. To fix the membranes, add 700 µL of 10% formalin into the well. Keep at RT for 15 min.
15. Aspirate formalin and add 700 µL ice-cold PBS. Repeat 2-3 times.
16. Staging the membrane with 700uL of 300 nM DAPI stain solution:
    i. Add 2.1 µm of 5 mg/mL DAPI stock to 100 uL of PBS to make a 300 µM DAPI intermediate dilution.
    ii. Dilute the 300 µM DAPI intermediate dilution 1:1,000 in PBS as needed to make a 300 nM DAPI stain solution.
    iii. Stain for 30 min at RT protected from light.
    iv. Wash with 700 µL ice-cold PBS. Repeat 2-3 times.
17. Image on the inverted microscope in brightfield and DAPI channels with 5x magnification. Take 3 non-overlapping FOV per well.
18. Export images in 16-bit images in TIFF format (make sure to check the box next to Original Data).
19. Image Analysis in FIJI ImageJ:
    i. Combine all DAPI.ORG images into a stack.
    ii. Set scale ratio: 0.785 px/1µm when using 5X objective.
    iii. Set up a threshold to convert all images in the stack to binary.
    iv. Remove small objects by binary filter Open.
    v. Perform watershed segmentation.
    vi. Count cells via analyze particles. Set a100 µm-infinity threshold. Select exclude on the edges.

20. Statistical Analysis: Calculate % invasion (of total tumor cells seeded) using the following equation:

$$\%\ \text{Invasion} = \frac{\text{Average cell count} \cdot \text{Membrane surface Aaea}}{\text{Image field of view Aaea} \cdot \text{Number of cells seeded}} \cdot 100$$

21. Repeat experiment at least three times to yield biological replicates. Present data as mean ± standard error of the mean (SEM). Perform unpaired *t* tests or two-way ANOVA for statistical analysis of unmatched groups.

7. Image segmentation of LN anatomical regions.

1. Perform immunostaining of LN slices for markers of: (i) fibroblast reticular cells (FRCs) using anti-mouse podoplanin antibody, BioLegend cat# 127423; (ii) lymphatic endothelial cells (LECs) via anti-mouse lyve1, Invitrogen cat# # 53-0443-82; (iii) a B cell marker B220 anti-mouse, BioLegend cat# 103229 or anti-mouse CD19, Bio-Rad cat# MCA1439SBV67; and, optionally, for a T cell marker (iv) anti-mouse CD3, BioLegend cat# 100235. (Detailed protocol for LN slice immunostaining is available elsewhere).
2. Open images from the individual channels in Fiji ImageJ. Open regions of interest (ROI) manager: Analyze > Tools > ROI Manager. Use Wand (tracing) tool to select individual regions.
    i. Subcapsular sinus (SCS) region as the area between podoplanin positive LECs lining the ceiling of the SCS and lyve1 positive LECs lining the floor of the SCS. Add selected region to the ROI Manager.
    ii. B-cell region as B220 or CD19 positive area, define a B cell follicle region was defined as $B220^{high}$ region within the cortex.
    iii. Medullary region as a lyve1 positive area in the paracortex of LN.

iv. T cell zone as the CD3 positive area of the LN in the paracortex excluding SCS, cortex, B cell follicles and medulla regions.

8. Gap analysis of FRC stromal network.

1. Install Fiji ImageJ Max Inscribed Circles Plugin from BioImaging And Optics Platform (BIOP) .
2. Acquire images of LN FRC stroma immunostained for podoplanin. (Detailed protocol for immunostaining is available elsewhere). Briefly, block LN slices in Fc block (anti-CD16/32) at working concentration of 0.025 mg/mL. Reserve slices for unstained controls (n=3). Stain LN slices with anti-mouse podoplanin antibody solution at working concentration of 0.02 mg/mL block. Fix LN slices at RT for 30 min with gentle agitation. Rinse in PBS. Obtain images via confocal microscope (×40 magnification objective) in z-stack.
3. Measure MFI of the unstained controls. Calculate background signal as average MFI+1 SD. Subtract background from all images stained for podoplanin. Process > Math > Subtract.
4. Set px to µm ratio (3.22 pixels/µm for 40x objective). Analyze > Set Scale
5. Create a stack from individual z-plane images. Image > Stacks > Images to stack > Max projection.
6. Create a z-stack projection. Image > Stacks > Z Project > Max projection.
7. Filter z-stack projection image. Process > Filters > Gaussian Blur (Sigma =1).
8. Convert to binary image. Image > Adjust > Treshold.
9. Remove small objects. Process > Binary > Close; Process > Binary > Fill Holes.

10. Use circle-fitting algorithm to fit the largest circle possible within the gaps. Plugins > Max Inscribed Circles > Minimum diameter
11. Measure the areas of individual inscribed circles. Analyze > Tools > ROI Manager > Measure.
12. Calculate radius. Analyze circles with radius >12 µm.

9. RNP transfection for CRISPR/Cas9-mediated gene knock out.

1. Use Benchling to design guide RNA (crRNA) to target coding region of the gene of interest.

Considerations when designing a crRNA:

i. The crRNA should be designed to bind close to the beginning of the coding region to increase the likelihood of disrupting the receptor's function (gRNA sequence should start at the beginning of at least within the first 40% of the gene coding sequence).
ii. Aim for a high on-target score. On-target score is a measure Cas cleavage efficiency of how likely a given gRNA sequence is to accurately target and bind to its intended genomic site.
iii. Aim for a high off-target score. The off-target score tells the inverse probability of Cas off-target binding. A higher score means the sequence has less chance to bind to sequences in the rest of the genome.
iv. Design 4-5 RNA guides. A total of three different guide crRNAs per coding region of the gene of interest are required.
v. Confirm the score of designed RNAs using IDT and Synthego.

2. Cas9/RNP nucleofection:

i. Precomplexing of Cas9/RNP. In a PCR strip, combine three crRNA–tracrRNA duplexes (3 µl equal to 150 pmol each, total of 9 µl) and 6 µl (180 pmol) TrueCut Cas9 Protein v2 (catalog no.

A36499; Thermo Fisher Scientific). Gently mix by pipetting up and down and incubate at RT for at least 10 min.

ii. Nucleofection. Resuspend $3 \cdot 10^6$ million BRPKp110 cells were in 20 µl primary cell nucleofection solution (P4 Primary Cell 4D-Nucleofector X kit S [32 RCT, V4XP-4032; Lonza). Mix and incubate with 15 µl Cas9/RNP at RT for 2 min. Transfer cell/RNP mix to a Nucleofection cuvette strips (4D-Nucleofector X kit S; Lonza). Electroporate using a 4D nucleofector (4D-Nucleofector Core Unit: Lonza, AAF-1002B; 4D-Nucleofector X Unit: AAF-1002X; Lonza) using pulse program EN-138. After nucleofection, resuspend transected cells were in pre-warmed complete media and cultured overnight. Continue with isolation of tracrRNA+ cells using cell sorter. Culture obtained cells until confluence.

3. Once a cell line has been established, adequate validation of the specific gene edits required. Common methods to validate engineered cell lines include sanger sequencing, next-generation sequencing, and qPCR to verify the edit at a genomic level. Western blot and mass spectrometry can provide confirmation at the proteomic level. For functional studies immunohistochemistry and FACS are often used.

10. Flow cytometric analysis of cancer cell infiltration in TDLNs.

Materials:

- Glass slides Premium plain microscope slides, FisherBrand, cat# 125441
- 96 round bottom well plate
- FACS buffer (PBS + 2-3% FCS and 1-2mM EDTA).
- 7AAD
- Antibodies:

i. Fc block purified anti-mouse CD16/32, clone 93, Rat IgG2a, κ, BioLegend, cat# 101302
ii. PE anti-mouse CD45, clone 30-F11, Isotype Rat IgG2b, κ, BioLegend, cat# 103105
iii. APC anti-GFP Antibody, clone FM264, Rat IgG2a, κ, BioLegend, cat# 338010
iv. Isotype Control APC RatIgG2a, clone RTK2758, Rat IgG2a, κ, BioLegend, cat# 400511
v. Isotype Control APC Rat IgG2b, κ, clone RTK4530, BioLegend, cat# 400611

- Permeabilization Buffer 10X, Invitrogen, ref# 00833356
- IC Fixation Buffer, Invitrogen, ref# 00822249
- Compensation beads UltraComp eBeads, Incitrogen, ref# 01222242
- Cancer cell culture (set 2-4 days prior for positive anti-GFP spiked controls)

1. Add 100 µL of media onto glass slide.

2. Place the sample (TDLN or control LN) into a droplet of media, then homogenize the tissue by gently pressing another glass slide on top.

3. Collect cells into FACS buffer.

4. Spin down by centrifugation at 400X for 5 min.

5. Resuspend in 200 µL of FACS buffer. Transfer to a round bottom 96 well plate.

6. Allocate cancer cells and cells from naïve LN for: live/dead control (1), unstained controls (2), and compensation controls and necessary FMOs controls.

7. Spin plate down by centrifugation at 400X for 3 min. Decant liquid by flicking plate into sink.

8.Live/Dead staining via 7AAD. Stain every well except for unstained and FMO 7AAD with 0.25 µL 7AAD in 300 µL of FACS buffer per sample. Incubate 20 min at RT, protected from light. Adding more than 0.5 µL of 7AAD to samples containing BRPKp110 cancer cell will result into bleedover to Red-Red channel.

9. Prepare Dead control by adding 300 µL of 70% ethanol to unstained cells. Incubate 20 min at room temperature, protected from light.

10. After 20 min incubation spin down by centrifugation at 400X for 3 min.

11. Resuspend Dead control in FACS buffer. Stain for 7AAD as above.

12. Add 300 µL of FACS buffer (to wash) and spin down/decant as above.

13. Surface staining:

i. Prepare Fc block (anti-CD16/32) in FACS buffer at working concentration of 0.025 mg/mL.

ii. Add 25 µL of Fc block to all wells except unstained and any FMOs. Incubate for 5 min on ice, protected from light.

iii. Prepare surface staining antibodies (anti-CD45) in FACS buffer at working concentration of 0.025 mg/mL. Add 50 µL per sample (except FMO control). Incubate for 15 min on ice, protected from light.

iv. Add 200 µL of FACS buffer and spin/decant as above.

14. Intracellular staining:

i. Prepare 1x Perm Wash (mix 1 part of 10x PermWash with 9 parts of DI water).

ii. Add 1x Perm Wash at 150 µL per well. Spin down and decant.

iii. Resuspend appropriate wells in necessary intracellular antibodies (typically used at 1:100) diluted in 1x PermWash. Incubate at room temperature for 60 min, protected from light.

iv. Add 150ul 1x PermWash, spin down and decant.

v. Add 200ul 1x PermWash, spin down and decant.

vi. Resuspend in 300 µL FACS buffer.

15. Wrap plate in foil if not analyzing immediately.

16. On the day of the flow cytometry, prepare your compensation beads:

i. Vortex bottle of eBioscience UltraComp eBeads for 20 seconds.

ii. Add one drop of beads to a labeled Eppendorf tube. Make one tube for each antibody you used in your panel.

iii. Add 1 µL of each antibody to the appropriate tube. You should have one comp tube per fluorochrome.

iv. Vortex well and incubate at room temperature for 15 min, protected from the light.

v. Add 300 µL of FACS buffer, mix well and transport to the 96 well plate.